SANDIA REPORT
SAND2005-1389
Unlimited Release
Printed March 2005

Bioaerosol Collection and Concentration for Microseparations-Based Detectors

Karl Wally, Eric B. Cummings, C.R. Bowe Ellis, Michael P. Kanouff

Prepared by
Sandia National Laboratories
Albuquerque, New Mexico 87185 and Livermore, California 94550

Sandia is a multiprogram laboratory operated by Sandia Corporation,
a Lockheed Martin Company, for the United States Department of Energy's
National Nuclear Security Administration under Contract DE-AC04-94-AL85000.

Approved for public release; further dissemination unlimited.

Sandia National Laboratories

Issued by Sandia National Laboratories, operated for the United States Department of Energy by Sandia Corporation.

NOTICE: This report was prepared as an account of work sponsored by an agency of the United States Government. Neither the United States Government, nor any agency thereof, nor any of their employees, nor any of their contractors, subcontractors, or their employees, make any warranty, express or implied, or assume any legal liability or responsibility for the accuracy, completeness, or usefulness of any information, apparatus, product, or process disclosed, or represent that its use would not infringe privately owned rights. Reference herein to any specific commercial product, process, or service by trade name, trademark, manufacturer, or otherwise, does not necessarily constitute or imply its endorsement, recommendation, or favoring by the United States Government, any agency thereof, or any of their contractors or subcontractors. The views and opinions expressed herein do not necessarily state or reflect those of the United States Government, any agency thereof, or any of their contractors.

Printed in the United States of America. This report has been reproduced directly from the best available copy.

Available to DOE and DOE contractors from
U.S. Department of Energy
Office of Scientific and Technical Information
P.O. Box 62
Oak Ridge, TN 37831

Telephone: (865) 576-8401
Facsimile: (865) 576-5728
E-Mail: reports@adonis.osti.gov
Online ordering: http://www.doe.gov/bridge

Available to the public from
U.S. Department of Commerce
National Technical Information Service
5285 Port Royal Rd
Springfield, VA 22161

Telephone: (800) 553-6847
Facsimile: (703) 605-6900
E-Mail: orders@ntis.fedworld.gov
Online order: http://www.ntis.gov/help/ordermethods.asp?loc=7-4-0#online

SAND2005-1389
Printed March 2005

Bioaerosol Collection and Concentration for Microseparations-Based Detectors

Karl Wally, Eric B. Cummings, C.R. Bowe Ellis, Michael P. Kanouff
Sandia National Laboratories/California
P.O. Box 969
Livermore, CA 94551-0969

Daniel J. Rader
Sandia National Laboratories/New Mexico
P.O. Box 5800
Albuquerque, NM 87185

Abstract

The ability to detect Weapons of Mass Destruction biological agents rapidly and sensitively is vital to homeland security, spurring development of compact detection systems at Sandia and elsewhere. One such system is Sandia's microseparations-based μChemLab. Many bio-agents are serious health threats even at extremely low concentrations. Therefore, a universal challenge for detection systems is the efficient collection and selective transport of highly diffuse bio-agents against the enormous background of benign particles and species ever present in the ambient environment. We have investigated development of a "front end" system for the collection, preconcentration, and selective transport of aerosolized biological agents from dilute (1–10 active particles per liter of air) atmospheric samples, to ultimate concentrations of ~20 active particles per microliter of liquid, for interface with microfluidic-based analyses and detection systems. Our approach employs a Sandia-developed aerosol particle-focusing microseparator array to focus size-selected particles into a mating microimpinger array of open microfluidic transport channels. Upon collection (i.e., impingement, submergence, and liquid suspension), microfluidic dielectrophoretic particle concentrators and sorters can be employed to further concentrate and selectively transport bio-agent particles to the sample preparation stages of microfluidic analyses and detection systems. This report documents results in experimental testing, modeling and analysis, component design, and materials fabrication critical to establishing proof-of-principle for this collection "front end." Outstanding results have been achieved for the aerodynamic microseparator, and for the post-collection dielectrophoretic concentrator and sorter. Results have been obtained for the microimpinger, too, but issues of particle-trapping by surface tension in liquid surfaces have proven difficult. Subsequent particle submergence into liquid suspension for microfluidic transport has been demonstrated only inefficiently despite significant and varied effort. Importantly, the separate technologies whose development is described, (inertial microseparator, dielectrophoretic corduroy concentrator/sorter) should each, independently, prove greatly useful in a variety of additional applications.

Acknowledgement

This is the final report in fulfillment of reporting requirements for Sandia's Laboratory Directed Research and Development project 52713, "Bioaerosol Collection and Concentration for MicroSeparations-based Detectors." The support of Sandia National Laboratories and the U. S. Department of Energy for enabling this work through the Laboratory Directed Research and Development program is gratefully acknowledged. Sandia is a multi-program laboratory operated by Sandia Corporation, a Lockheed-Martin company, for the United States Department of Energy under contract DE-AC04094AL85000.

Table of Contents

Abstract **3**
Acknowledgement **4**
List of Figures **7**
Introduction **9**
Background 9
Laboratory Directed Research and Development Project 9
Specific "Front End" Technologies and Summary of Results 12
Chapter 2 Experimental Studies of Microseparator Performance **15**
Introduction 15
Particle Inertia 15
Experimental Test Bed 16
Opposed Flow Virtual Cyclone (OFVC) 18
Experimental Characterization of a Second-Generation OFVC 21
Conclusions from OFVC Testing 26
Modeling of the OFVC "wiggle" 26
References **29**
Chapter 3 Microimpinger Development and Testing **31**
Introduction and Previous Work 31
Development Summary 32
First Generation Microimpinger Design 33
Second Generation Microimpinger Design 33
Foturan Microimpinger Chips 35
Plastic Microimpinger Chips 37
Experiments with Open Microchannels 38
Evaporation from Open Microchannels 38
Flow in Open Microchannels 38
OFVC Integration with Plastic Microimpinger Chips 40
Aerosol Impingement Experiments 44
Microparticle Capture by Surface Tension 45
Particle impingement calculations 46
Particle Submergence Strategies 52
Water Droplet Bombardment to Force Particle Submersion 54
Conclusions 57
References 58
Chapter 4 The Corduroy Design Methodology for Dielectrophoretic Particle Concentration and Sorting **59**
Introduction 59
Post-based Batch Concentrators 60
Post-based Continuous Concentrators 62
Facet-based Devices 64
Corduroy-based Devices 65
The Corduroy Design Methodology 66
Interaction of a Particle with a Corduroy Obstacle 66
Experimental Results 69

MuCAD 72
Conclusions 73
References 73
Chapter 5 Remaining Challenges to Integration 75
Further Work for Readiness Development 75
Microseparator – Micromolding/Microembossing Development 75
Microimpinger – Integration with Inkjet Printhead Technology 76
Dielectrophoretic Devices – Micromolding/Microembossing Demonstration 77
Integrated Demonstration 77
Sample Preparation – Another Need for Successful Integration 77
References 78
Chapter 6 Additional Potential Applications 79
Applications for OFVC Microseparator 79
HERD – Hybrid Emergency Radiation Detector 79
Bioaerosol Trigger 80
Aerosol Lab-on-a-Chip 80
Applications for Corduroy DEP Concentrators and Sorters 81
Applications for Direct Microimpingement Technology 82
Appendix A MuCAD 83
Distribution 90

List of Figures

Chapter 1 – Introduction

Figure 1-1 Schematic of Proposed Technical Approach to Bioaerosol Sampling Problem 12
Figure 1-2 Schematic Plot of the Proposed Particle-sorting Strategy 13

Chapter 2 – Experimental Studies of Microseparator Performance

Figure 2-1 Schematic diagram of experimental test bed 19
Figure 2-2 Schematic of a 2-D Opposed Flow Virtual Cyclone (OFVC) 21
Figure 2-3 Calculated air flowstreams and particle trajectories for a 2-D OFVC 23
Figure 2-4 Disassembled View of Modular OFVC Test Apparatus 24
Figure 2-5 Micrographs of particle deposits in an OFVC 25
Figure 2-6 Micrographs of exit-slit width and particle deposit widths in an OFVC 26
Figure 2-7 Dependence of particle deposit width on droplet aerodynamic diameter 27
Figure 2-8 Demonstration of Linear and Oscillatory Particle Deposits 28
Figure 2-9 Micrograph of unexpected OFVC particle deposition pattern 29
Figure 2-10 Three-Dimensional Finite Element Model of OFVC 30
Figure 2-11 Calculated Particle Deposition Pattern for OFVC with Asymmetric Velocity Boundary Condition 30
Figure 2-12 Finite Element Model of OFVC with Bump at its Inlet 31
Figure 2-13 Calculated Particle Deposition Pattern for OFVC with a Bump at Inlet 31

Chapter 3 – Microimpinger Development and Testing

Figure 3-1 Photograph of First Generation Microimpinger Fabricated from Glass 36
Figure 3-2 Maximum / Minimum Pressures for Surface Tension in a Microchannel 37
Figure 3-3 First and Second Generation Microimpinger Designs 38
Figure 3-4 Process Schematic for Second Generation Foturan Microimpinger 39
Figure 3-5 Micrograph of a Deep Aspect Ratio Foturan Microchannel 39
Figure 3-6 Microbalance Method for Determining Microchannel Evaporation 41
Figure 3-7 Experimental Setup for Gravity Flow Through an Open Microchannel 42
Figure 3-8 Calculated and Measured Reservoir Elevations for Overflow Limits 42
Figure 3-9 Micrograph of Microchannel End With and Without Overflow 43
Figure 3-10 Various Views of Acrylic Microimpinger Chip used in Experiments 44
Figure 3-11 Schematic Diagram of the Aerosol Collection and Impingement Experiment 44
Figure 3-12 Calculated Reservoir Elevations and Liquid Flow Velocities for Steady Flow in Open Microchannels 46
Figure 3-13 A Comparison of Calculated and Measured Liquid Reservoir Elevations Resulting in Overflow From an Open Microchannel 46
Figure 3-14 Micrograph of PSL Microspheres Deposited into Open Microchannel Through OFVC Operation, Showing Dried and Stuck Particles 47
Figure 3-15 Schematic Diagram Showing Qualitatively the Free Surface Deformation Needed for Surface Tension to Support Hydrophilic, Neutral, and Hydrophobic Particles Against Gravity 50

Figure 3-16 Calculated Pressure and Shear Stress Due to Particle Impingement at Low Impingement Velocity 52
Figure 3-17 Calculated Results for Particle Impinging Free Surface 52
Figure 3-18 Impulse of Various Fluid Forces as Particle Impinges a Free Surface 53
Figure 3-19 Effect of Various Parameters on Impingement Depth of Penetration 54
Figure 3-20 Calculated Pressure and Shear Stress Due to Particle Impingement at High Impingement Velocity 49
Figure 3-21 Droplet Size Distribution used for Bombardment Submergence Tests 52
Figure 3-22 Micrograph Showing Fluorescent Particle Evidence of Submergence 58
Figure 3-23 Composite Micrograph Showing Fluorescent Particle Evidence of Particle Capture by Surface Tension, and of Particle Transport via Submergence and Suspension 58

Chapter 4 – Testing and Development of the Corduroy Design Methodology for Dielectrophoretic Particle Concentration and Sorting

Figure 4-1 Selective Dielectrophoretic Trapping of *B. Cereus* vs. *B. Subtilis* in an Array of Circular Posts on 200 μm Centers. 66
Figure 4-2 Steady-state Dielectrophoretic Trapping of *B. Cereus* vs. *B. Subtilis* 66
Figure 4-3 Combined Electrokinetic and Dielectrophoretic Flow of Particles Down an Array of Insulating Square Posts on 63 μm Centers 67
Figure 4-4 A Post-based Continuous-Flow Dielectrophoretic Concentrator Design 68
Figure 4-5 A Facet-based Dielectrophoretic Concentrator 70
Figure 4-6 Numerical Simulations of Particle Motion Past a Corduroy Ridge Obstacle 65
Figure 4-7 Numerical Simulations of Particle Motion Past a Corduroy Valley Obstacle 65
Figure 4-8 Filter/Concentrator Response of a Straight-Central-Section Corduroy Obstacle 73
Figure 4-9 The Use of a Convex Curved Obstacle as a Dispersive Element 74
Figure 4-10 Design of the First Corduroy Test Chip 75
Figure 4-11 Steady-state Operation of a Hybrid Continuous/Batch Corduroy Concentrator 76
Figure 4-12 MuCAD Screen Shot of Top-Level View of Device Hierarchy 77

Chapter 6 – Other Potential Applications

Figure 6-1 Hybrid Emergency Radiation Detector (HERD) Prototype Incorporating An Opposed-Flow Virtual Cyclone Aerosol Collector 86
Figure 6-2 Schematic of Aerosol-Lab-on-a-Chip (ALOC) Concept Using Large Arrays of Identical Parallel OFVC Samplers 87

Appendix A – MuCAD

Figure A-1 MuCAD Screen Shot of Top-Level View of Device Hierarchy 90
Figure A-2 MuCAD Screen Shot with the Rectangular Element Hierarchy Selected 91
Figure A-3 MuCAD Screen Shot with the Array Element Selected 92
Figure A-4 MuCAD Screen Shot of the Master Element of the Array 93
Figure A-5 Automated Intelligent Etch-back Compensation 94
Figure A-6 MuCAD Screen Shot of Etch Simulation of Etchback Compensated Design 94
Figure A-7 MuCAD Etch Simulation in a Format Compatible with *Laplace* Flow Solver 95
Figure A-8 Combination of MuCAD and *Laplace* Supports Development and Simulation of Designs 96

Chapter 1 Introduction

Background

The vulnerability of the United States to attack by airborne biological pathogens was demonstrated in 2001 by the circulation of anthrax-bearing letters through the US Postal Service. Additional terrorist attack scenarios using biological aerosols (bioaerosols) are readily conceivable. The intentional spread of bioaerosols among civilian populations is an emerging Weapons of Mass Destruction (WMD) threat. New technologies are needed to effectively counter such threats. A critical need exists at this time for small, integrated, effective sensors to rapidly detect and identify airborne pathogens. Mobile sensors could accompany military troops or civilian responders to warn of attack, while fixed sensors could be deployed throughout buildings to provide rapid warning of exposure to civilian or military residents. The ability to rapidly detect and correctly identify pathogens will dramatically increase human survival rates: faster responses save lives.

A universal challenge limiting the development of real-time bioaerosol sensors is the discrimination of a small number of airborne pathogens from an enormous background of benign environmental particles. Inhalation of biological pathogens can be infectious at extremely low concentrations, for example, 1–10 active pathogens per liter of air. In contrast, ambient particle concentrations range from thousands to billions of particles per liter. As much of the ambient aerosol load is man made, high ambient particle levels can be expected in high population areas. The discrimination of a pathogen from an urban particle background is a daunting task. Consequently, DOE, DARPA and DTRA have all identified sampling and sample preparation as critical unresolved issues in the implementation of micro-analytical systems.

Laboratory Directed Research and Development Project

The goal of this project was to demonstrate proof-of-concept for a complementary set of "front end" technologies for the collection, characterization, concentration, and selective transport of bioaerosol agents to a down-stream micro- total analysis system (μTAS) for careful pathogen identification. Ideally, a "front-end" for such systems would selectively extract pathogens from an air sample while excluding the benign background particles, and would concentrate the pathogens into a liquid microliter sample at concentrations of ~20/μl. To accomplish this task, the system we investigated has engineerable selectivities—sensitive to mass, size, geometry, internal structure, and charge—to provide aerosol particle pre-screening. The goal of a front-end system is to enhance the chances of pathogen particle collection, while dramatically lowering the number of background particles, and thereby increasing the sensitivity of the down-stream analytical system. A secondary benefit of this strategy is to reduce the likelihood of fouling the downstream sensors by particle overload. Our project focused on the development of key front-end particle manipulation technologies which can ultimately be integrated into a prototype that will be sufficiently flexible to allow it to be coupled to a wide range of down-stream analytical systems. Such systems include Sandia National Laboratories' μChemLab, the joint Sandia/LLNL BioBriefcase, a miniaturized version of Lawrence Livermore National

Laboratory's Autonomous Pathogen Detection System (APDS), as well as candidate systems for the Joint Point Biological Detection System (JPBDS) program, and commercial μTAS instruments.

Our approach is designed to sample air at a flow rate of ~5 l/min and to transport selected airborne agents to a microfluidic sample-preparation stage of a μTAS instrument for subsequent analysis. This scheme is shown conceptually in Figure 1-1.

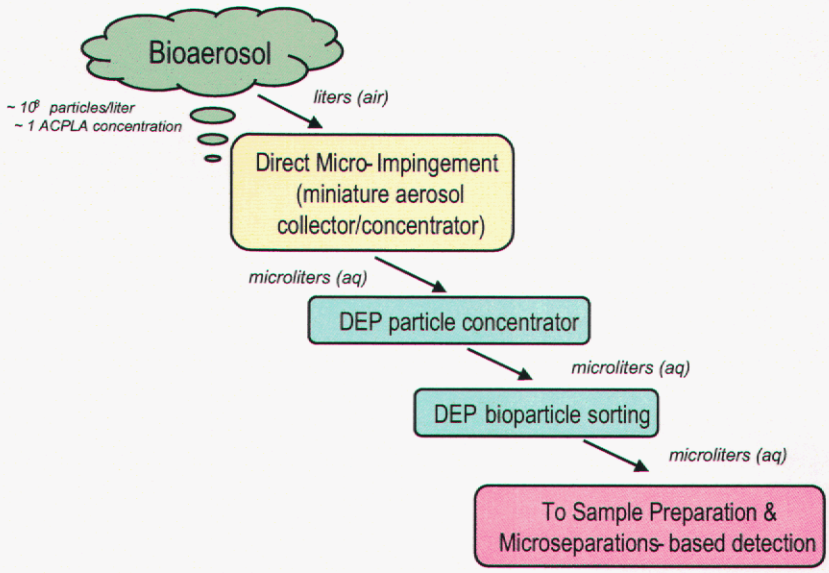

Figure 1-1 Schematic diagram of the technical approach to the bioaerosol sampling problem.

The approach embodies novel techniques of collection or concentration for which Sandia has received, or is presently pursuing, patent protection. The concept of a direct microimpingement concentrator is a bold approach enabled by Sandia's microfabrication capabilities. Direct impingement of particles into a microchannel is intended to minimize fluid volume inventory and dramatically reduce evaporative losses. Traditional aerosol collection means require collection volumes in excess of milliliters, which would necessitate a thousand fold further solution concentration, into mere microliters, for chip-based assay. Instead, a microseparator can be used to impinge particles into liquid flowing in an open, three-sided microfluidic channel, from which the liquid microsuspension would be transported to "back-end" preparation and analysis stages. Sandia's patented opposed-flow virtual cyclone aerosol particle separator/concentrator was first conceived in the context of this direct microimpingement concentrator application, and its most effective utilization is best realized at this mesoscale. This aerosol separator/concentrator geometry allows tightly focused particles to impinge directly at the microscale, for example onto the liquid surface of open microchannels. Electrokinesis, a phenomenon we extensively exploit in microseparations, is a practical method to transport the minute volume of liquid in this free-liquid-surface impingement system. Once particles are collected in liquid microsuspension, we can exploit dielectrophoretic particle vectoring for

concentration, and for subsequent particle sorting. This cascade of separation, concentration, and sorting can be used to present a highly-selected sample to a μTAS system for analysis and detection. The concept is shown schematically in Figure 1-2.

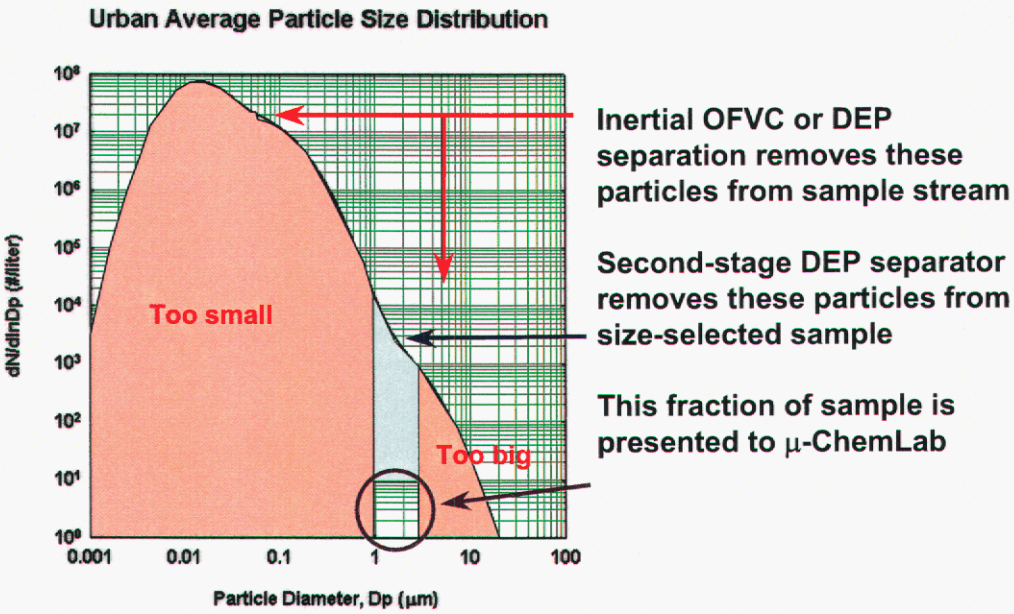

Figure 1-2 Schematic plot of the proposed particle-sorting strategy.

The ultimate goal of the project is to equip highly specialized bio-analysis systems with the needed flexibility to address a wide spectrum of bioaerosol threat scenarios. Compared to alternate technologies, the proposed systems would be:

1. Smaller: these systems will be compact by virtue of their microfabricated components, integrated optoelectronics, and microfluidic devices.

2. More selective: the staging of complementary approaches sorts particles based on independent measurements of particle composition and physique, e.g. size, polarizability, geometry, and conductivity. The combination of independent stages should achieve bioaerosol number density enrichment factors up to 10^6 over ambient particle background and absolute concentration factors exceeding 10^9.

3. More broadly applicable: the selectively-concentrated sample can be delivered to collection plates, screens or a microfluidic manifold for transport to a wide range of bio-analytical detection systems. Of course, for each detection system, a sample preparation stage would likely also be required, specific to the analysis and detection to be performed. This final stage provides an automated means to exchange solutions and lyse and label samples for analysis down-stream. Its specificity to the analysis and detection to be done precludes its inclusion in the cascade of "front-end" technologies; rather it belongs with "back-end" technology.

Specific "Front End" Technologies and Summary of Results

A concept of a miniature bioaerosol collector/concentrator has been investigated which exploits direct microimpingement to achieve its goals. This collector/concentrator is configured in two stages. The first stage employs a miniature air collection fan to draw particle-laden ambient air through an array of microseparators that inertially separate and concentrate particles falling within a user-specified aerodynamic size range (e.g., 1–3 μm). Particles in this desired size range are selectively focused by the microseparator into streams of particles for direct microimpingement into O(10 μl) of liquid contained in open microchannels within the microimpinger. Microseparator development and testing results are discussed in Chapter 2. Microimpinger development, performance issues, and testing results are discussed in Chapter 3.

Once particles have been collected into liquid suspension, they are concentrated by the microfluidic dielectrophoretic particle concentrator, wherein concentration is achieved through manipulation of the difference in conductivity between particles and transporting fluid within electric fields caused to vary by changes in the geometrical structure of the dielectric microchannels. A second stage can further sort the concentrated particles, again by manipulation of dielectrophoretic sensitivities to size, surface charge, complex conductivity, and the variation in complex conductivity with frequency—a window into the internal physical structure of particles. Dielectrophoretic concentrator and sorter development are discussed in Chapter 4.

This report documents results in experimental testing, modeling and analysis, component design, and materials fabrication critical to establishing proof-of-principle for our selected approach to bioaerosol collection and concentration. In several respects, the results of this LDRD project have exceeded initial expectations.

Through refinement of the Opposed Flow Virtual Cyclone microseparator technology, we have developed a highly effective means to continuously separate the respirable (1–10 μm particle diameter) fraction of particles from aerosol samples, and deliver those respirable particles in an extremely focused stream (line or spot) for impingement collection, deposition collection, real-time laser interrogation, etc.

With the direct microimpinger development, we have demonstrated a rudimentary ability to impinge a highly focused stream of respirable particles directly into a microfluidic collection and transport system. In the course of this microimpinger work, we encountered the phenomenon of the capture and trapping of microparticles (< 10 μm particle diameter) in (on) the free surface of a collection liquid by surface tension forces. This phenomenon obtains for microparticles if impinging at any velocities less than extremely high velocity (i.e., ~100 m/s, or "hurricane" wind velocity). The existence of this surface tension particle trapping phenomenon is a significant hurdle to the use of direct microimpingement. After testing a number of approaches to overcome surface tension effects, we found that bombarding the particle-laden surface with microdroplets wetted and submersed a reasonable fraction of the particles. Nevertheless, one of the central findings of this LDRD is that this surface tension phenomenon severely complicates and limits

the approach of direct impingement into a microscopic liquid stream and likely steers one away from such designs.

With the invention and development of the Corduroy Dielectrophoretic Design Methodology for the dielectrophoretic concentration and/or sorting of particles, Sandia researchers have produced a world class technology that significantly advances the state of the art. One can anticipate this development is likely to achieve significant recognition, and ultimately, important application in the field of microfluidics. Easy to engineer and intuitive, the technique incurs little or no added costs, and achieves great performance improvements, compared to the previous state-of-the-art. In principle, this methodology allows one to engineer a continuous particle spectrometer comprising two patterned ridges on a microchannel surface driven by two electrodes that supply a single D.C. voltage. This remarkable advance exceeds our most optimistic hopes at the project start.

Some important goals remain unmet because of performance problems with the direct impingemer. An initial objective of this LDRD project was the demonstration of an integrated "front end" system capable of the collection, preconcentration, and selective transport of aerosolized biological agents from dilute atmospheric concentrations to microliter liquid concentrations for interfacing with μTAS systems such as Sandia's μChemLab for identification of bioagent bacteria and spores. Although our work has demonstrated, to a greater or lesser extent, individual needed front-end technologies, we were, unfortunately, not able to achieve our goal of an integrated demonstration before the LDRD project ended with key microimpingement issues not yet fully resolved. It should be noted that, although integration and an integrated demonstration was one of the stated goals of this project when it began, the inertial microseparator and dielectrophoretic corduroy concentrator/sorters are separately useful technological products of this project, as discussed in Chapter 6 on additional applications. Our study of the issues of direct impingement is also important for understanding flow regimes needed for efficient gas-to-liquid particle transfer, which provides Sandia an enhanced ability to evaluate future approaches to such transfers.

This page intentionally contains only this sentence.

Chapter 2 Experimental Studies of Microseparator Performance

Introduction

The goal of this activity was to experimentally demonstrate a new microseparator technology for selectively depositing respirable aerosol particles onto a small, well-defined region of a solid or liquid substrate. For the purposes of this work, respirable particles are considered to be those with aerodynamic diameters in the 1–10 μm range (although the proposed technology is flexible enough to allow the user to select the final operational size range). While a variety of macroscopic separation technologies are commonly available (e.g., inertial impactors and virtual impactors), the key challenges in the present work are: 1) to demonstrate particle impingement into MEMs-scale regions (e.g., ~100 μm trenches) and 2) to demonstrate size-selective collection (e.g., only collect particles in the 1–10 μm aerodynamic size range).

The novel microseparator concept that was studied experimentally in this work was the Opposed Flow Virtual Cyclone (OFVC). The OFVC concept relies on particle inertia to initially sort and ultimately impinge airborne particles onto a collection substrate. Inertia-based particle manipulation relies on the fact that airborne particle densities are much larger than gas densities; consequently, particles cannot follow sharp changes in the gas flow direction. By careful design of the gas-flow path, particles can be focused into small regions or can be made to deposit onto adjacent surfaces. A brief review of the parameters controlling particle inertia is presented in the following section. A description of the experimental test set up used in evaluating the OFVC is presented next. The final section describes the experimental results.

Particle Inertia

The role of particle inertia in determining the extent of focusing or impaction is known to depend on the dimensionless particle Stokes number, which is defined as the ratio of the particle relaxation time, τ, to a characteristic time scale of the flow, t_f (Hinds, 1982). After being concentrated in the opposed-flow region of the OFVC, final particle collection is accomplished by inertial impaction. The gas exiting a narrow slit is turned by a flat plate normal to the resulting jet. Although the flow can turn quickly enough, particles cannot because of their inertia and consequently impact the plate. For inertial impactors, the slit half-width, $W/2$, and the mean gas velocity in the slit, V, are traditionally used to define the characteristic flow time scale. The dimensionless particle Stokes number, Stk, can then be written (Hinds, 1982, p.114):

$$\mathrm{Stk} = \rho_p D_p^2 V C / (9 \mu W) \tag{1-1}$$

where μ is the fluid viscosity, and D_p, ρ_p and C are the particle diameter, density and slip correction factor, respectively. The factor C is introduced to correct the particle drag law for rarefied effects; C is a function of particle size that tends to unity for large particles (Hinds,

1982, p. 45). In the present work, where the particles of interest are larger than ~1 μm, the slip correction factor differs from unity by at most 10% and $C = 1$ is assumed in the following discussion. The strength of the inertial effect depends on both particle diameter and particle density as given by Equation (1-1); thus a 1-μm particle with a density of 1 g/cm^3 will behave the same (aerodynamically) as an 0.5-μm particle with a density of 4 g/cm^3. When discussing particle inertial behavior, the aerosol community typically refers to a particle's *aerodynamic diameter,* D_{ae}, which is the diameter of the unit density (ρ_p = 1 g/cm^3) sphere that has the same settling velocity (and Stk) as the particle (Hinds, 1982, p. 49). Thus, a 1-μm, 1-g/cm^3 spherical particle and an 0.5-μm, 4-g/cm^{3}spherical particle have identical aerodynamic diameters of 1 μm.

A benefit of using the Stokes number is that for a given geometry, Stk is nearly constant over a wide range of fluid Reynolds numbers. For example, in inertial impactors it is customary to define a characteristic aerodynamic diameter, $D_{ae,50}$, for which 50% of the incoming particles are collected. Previous experimental and numerical studies (Hinds, 1982) have shown that the corresponding Stk_{50} is approximately 0.53 for a rectangular (slit) impactor such as is of interest here. In this case, the definition of the Stokes number can be used to write:

$$D_{ae,50} = \{ 9\, \mu\, W\, Stk_{50} / V \}^{1/2} \qquad (1\text{-}2)$$

where the particle density and slip correction have been assumed to be unity (according to the definition of $D_{ae,50}$ as the aerodynamic diameter) and the value of Stk_{50} is approximately constant. The potential value of micromachined parts is clearly evident, as the ability to make smaller slits (smaller W) translates into the ability to collect smaller-sized particles.

Experimental Test Bed

The experimental test bed used to characterize the OFVC prototype is shown in Figure 2-1. Monodisperse (same-sized) drops for microimpinger calibrations were generated using a TSI (St. Paul, MN) Vibrating Orifice Aerosol Generator (VOAG). The VOAG is based on the instability of a cylindrical liquid jet, which tends to break into droplets when subjected to mechanical disturbances. When these mechanical disturbances are regular and of sufficient amplitude, a uniform break-up of the liquid jet results, creating equal-sized droplets over a specific frequency range. The final drop size is determined by the frequency of the disturbance driving the break-up; the operating frequency is controlled by a signal generator and can be used to quickly change the droplet size. The basic operating principles of a monodisperse aerosol standard generator based on uniform droplet break-up were first published by Berglund and Liu (1973), and were later incorporated into a commercial instrument. To generate particles in the 1 to 10 μm range, trace quantities of oleic acid (olive oil) were dissolved in isopropanol and the combined solution was pressed through a 20 μm orifice plate to create the liquid jet. After break-up, the droplets are allowed to dry to remove the volatile solvent, leaving behind a monodisperse oleic acid aerosol. As the drops dry, they are also charge neutralized by exposure to ions generated in the suspending gas (air) by a radioactive Kr-85 source. Under the present operating conditions, the monodisperse oleic acid droplets leaving the VOAG drying chamber should have time to reach a quasi-steady Boltzmann charge distribution (only a few charges per droplet on average).

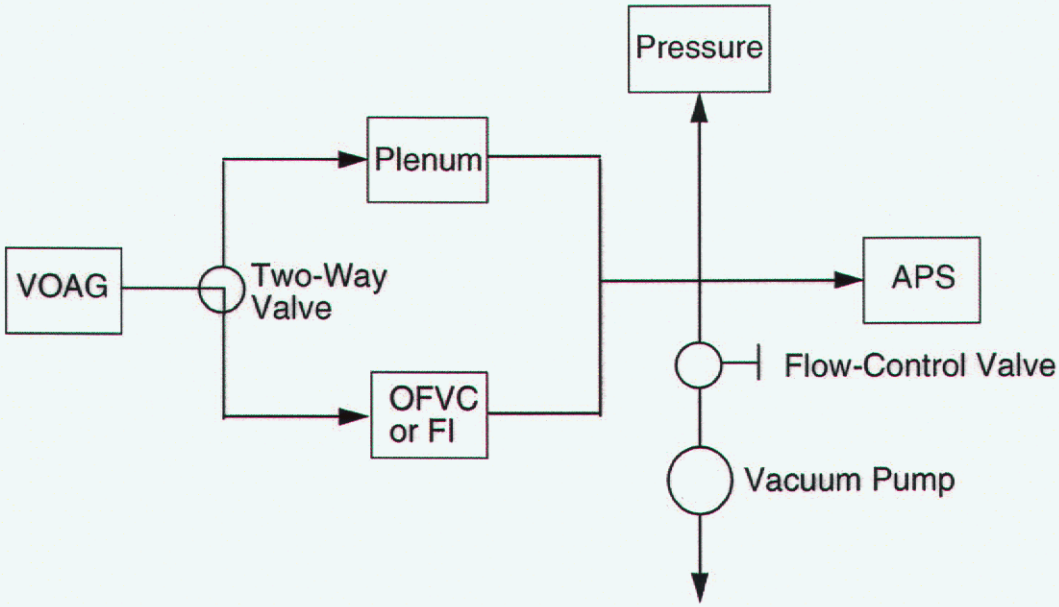

Figure 2-1 Schematic diagram of the experimental test bed.

After the VOAG, the calibration aerosol can be routed in one of two directions: 1) through an empty cylindrical tube (plenum), or 2) through an identical cylindrical tube containing the OFVC. The collection efficiency (fraction of particles entering the OFVC which are collected on the impaction plate) is determined from the ratio of the droplet concentration measured downstream of the OFVC to the concentration measured downstream of the plenum. This definition of the collection efficiency makes two implicit assumptions: 1) the concentration exiting the plenum equals the inlet concentration (to both tubes) and 2) all of the particles lost in passing through the OFVC are collected on the desired impaction plate. Both of these assumptions rely on negligible particle losses within the flow path; e.g., losses to walls inside the OFVC (FI) would reduce the measured downstream concentration and would lead to a high estimate for the collection efficiency. The magnitude of wall losses has not been determined in this work, although it is expected that losses should not be significant (say less than ~10%). The width of the deposited particle stripe is determined by direct examination of the collection substrate under a low-power microscope. A precision reticule is used to calibrate the optical system.

The particle concentration and size distribution is measured with a TSI Aerodynamic Particle Sizer (APS). The APS is a commercial instrument based on a method first proposed by Wilson and Liu (1980). A real-time extractive sampler, the APS measures aerodynamic diameter by determining a particle's velocity lag in a well-characterized accelerating flow. After being drawn into the APS, sampled particles are accelerated as the entraining gas flows through a converging nozzle. Depending on their size (and density), particles will lag the flow; particle size is related to this velocity deficit as measured with a two-spot laser velocimeter. The APS provides particle concentration (number of particles per cm^3 of air) versus aerodynamic diameter over the range of 0.5 to 30 μm at a sample flow rate of 5.4 liters per minute (LPM). As the particle response curve (velocity vs. size) cannot be predicted *a priori,* a calibration is required (e.g., Rader et al. 1990). In this study, commercially prepared monodisperse polystyrene latex (PSL) calibration particles (Duke Scientific, Palo Alto, CA) were used to verify the APS calibration curve. Three sizes of

PSL particles were used to span the size range of interest: 1.034, 1.335, and 1.588 μm. Because the specific gravity of PSL is about 1.05, the corresponding aerodynamic diameter for these three PSL samples is 1.060, 1.368, and 1.627 μm.

The downstream pressure was measured with a Paroscientific Model 760-15A absolute pressure transducer. To determine pressure drop through the particle collectors, the pressure measured with the gas flowing through the particle collector path was subtracted from the pressure measured through the plenum path. Typically, the largest pressure drop in the system was through the particle collectors (OFVC), so that the pressure downstream of the plenum was close to atmospheric.

Opposed Flow Virtual Cyclone (OFVC)

The Opposed Flow Virtual Cyclone (OFVC) provides a novel method for the selective focusing and collection of respirable particles. The OFVC is a variation on the virtual cyclone theme first described by Torczynski and Rader (1997). The virtual cyclone uses inertia to separate particles from a turning main flow and concentrates these particles into an adjacent chamber. In the virtual cyclone, the main particle-laden flow follows a wall that curves away from the original flow direction. A wall forms an inward-curving boundary to the main flow, while the outer boundary is formed by an adjacent, confined recirculating flow into which particles migrate by centrifugal action. Thus, in the virtual cyclone, particles are separated from the main flow by crossing a dividing streamline that separates the main flow from the adjacent recirculating flow. One attractive feature of the virtual cyclone is that it accomplishes particle separation with greatly reduced particle deposition on walls. The major drawback is that no convenient method presents itself for removing the enriched particles from the recirculating flow region.

The patented OFVC concept (Rader and Torczynski, 2000) preserves the inherent advantages of the virtual cyclone (no-impact particle separation in a simple geometry), while providing a more convenient design for concentrating particles in a flow-through geometry. A schematic of one embodiment of an OFVC is shown in Figure 2-2. The OFVC consists of two virtual cyclones arranged such that their inlet jets (of width H) are inwardly directed and symmetrically opposed. A top plate bounds both jets on one side of the inlets, while the other two walls curve away (with radius of curvature R) from each inlet jet before merging into a throat of width W. As in the standard virtual cyclone, the underlying principle of the OFVC is that each inlet jet follows its adjacent wall as it curves away, creating a recirculation region between the jets and the top plate. Because of centrifugal forces, particles move away from the wall and migrate towards the plane of symmetry. These particles eventually cross from the main flow, becoming concentrated in the central recirculating zone. Eventually particles escape the recirculation zone to be highly focused into a narrow region about the plane of symmetry between the two converging flows. A small flow could also be provided through a porous top plate for the purpose of purging particles from the recirculating region. Once focused near the centerline, the particles are collected into a deposit of width Δw using an impaction plate downstream of the OFVC.

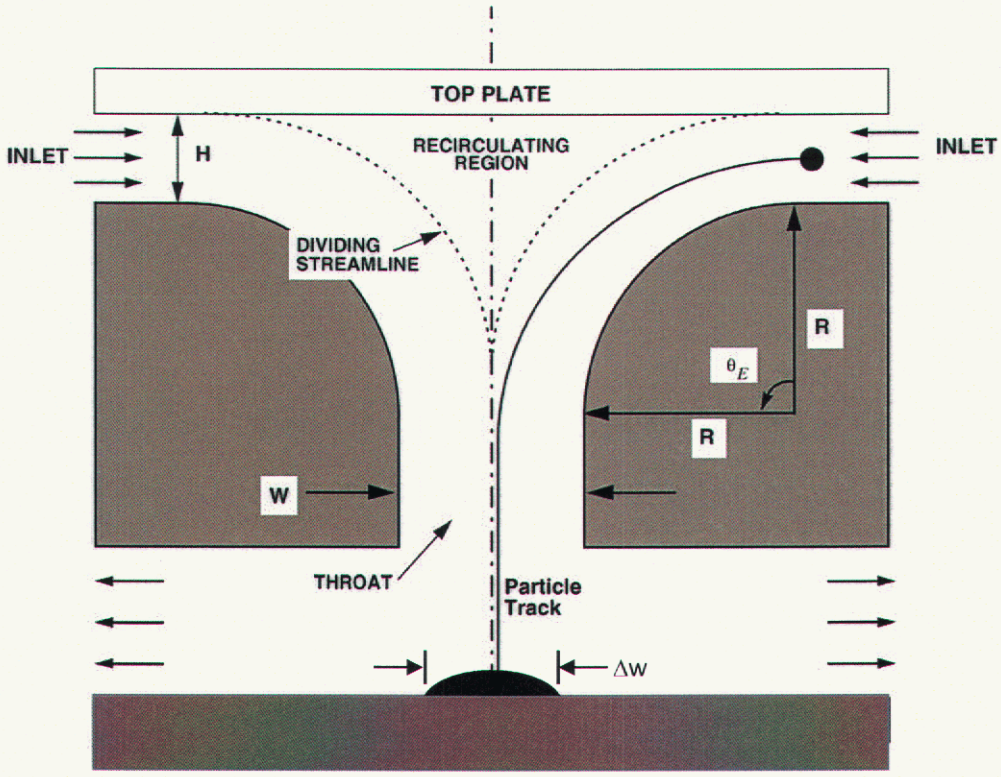

Figure 2-2 Schematic diagram of a 2-D Opposed Flow Virtual Cyclone.

An approximate analysis suggested that the OFVC only concentrates particles within a specific size range (Wally, 2001). Too small particles will tend to follow the main flow instead of moving centrifugally across the dividing streamline. Too large particles will overshoot the recirculating region and pass into the opposing jet and thereby resist focusing. A closed-form result for the focused particle size range was derived which identified the key controlling parameters: the inlet width H, inlet velocity U, total turning angle θ_E, radius of curvature R, throat width W, particle density, and gas viscosity. The analysis showed that smaller particles are concentrated by decreasing the slit width or by increasing the inlet gas velocity or the turning angle. This has interesting implications for MEMs devices, as the fabrication of OFVC devices with very thin slits allows concentration of very small-sized particles (for a fixed inlet velocity), or of larger particles with lower inlet velocities. The ability to concentrate particles at low gas velocities would greatly reduce the pressure drop (and power consumption) through such devices.

Numerical fluid/particle simulations (using a commercial flow code FIDAP, Fluent International) of several two-dimensional OFVC designs confirmed that a properly designed OFVC could provide significant respirable particle focusing along the OFVC plane of symmetry (Wally, 2001). For example, a series of simulations were performed with a 2-dimensional OFVC geometry (without the impaction plate) with W=2H and $\theta_E=\pi/2$. The following conditions were assumed: air at standard conditions, U=50 m/s, H=0.6 mm, W=1.2 mm, and R=3.5 mm. A small purge flow (~10% of the main flow) was introduced through an assumed porous top plate to avoid development of a large recirculation flow. Simulation results are shown in Figure 2-3.

Note that because of symmetry, each of the four plots is used to show two results, one on the left-hand side and one on the right-hand side. As shown in Figure 2-3*a*, the calculated streamlines stay attached to the lower wall. Particle trajectories are shown in Figures 2-3*b,c,d*; note that particle trajectories that cross the plane of symmetry are specularly reflected back so that the entire path can be shown on one side of the plot. Particle behavior was found to be in good agreement with the analytic predictions: 1.5 μm particles showed moderate focusing, particles between 2 and 5 μm showed excellent focusing, and focusing was lost for particles larger than about 5 μm. The predicted extent of particle focusing along the plane of symmetry is very high for particles in the range 1.5–5 μm. A key potential advantage of the OFVC geometry is the ability to focus particles from a relatively wide, user-selectable size range into the same small region of flow.

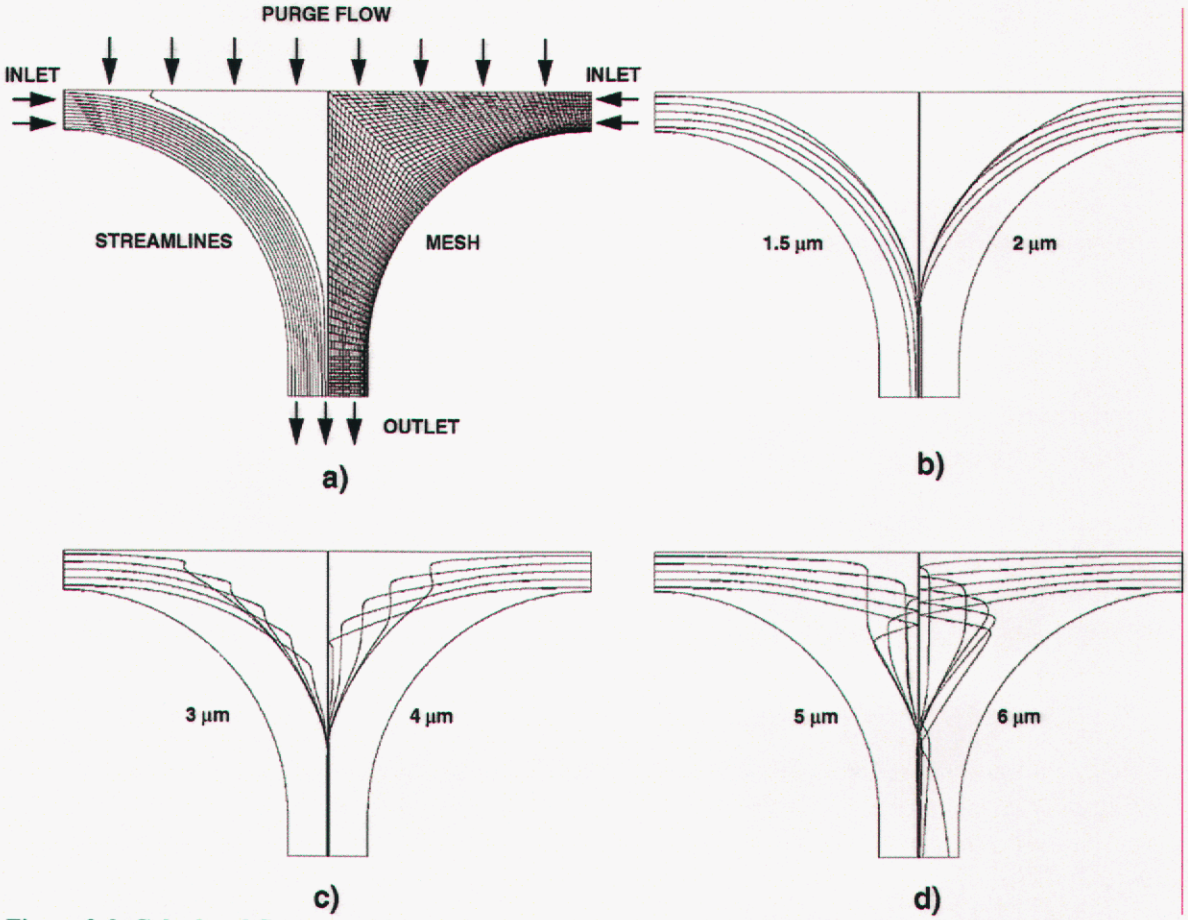

Figure 2-3 Calculated flow streamlines and particle trajectories for a 2-D OFVC: a) flow streamlines (left) and computational mesh (right); particle trajectories for b) 1.5 μm (left) and 2 μm (right), c) 3 μm (left) and 4 μm (right), and d) 5 μm (left) and 6 μm (right) .

Experimental Characterization of a Second-Generation OFVC

Previous work (Wally et al., 2002) described experimental characterization of a first-generation OFVC design. Particle focusing was clearly demonstrated with this device, although oscillating, "wiggly" (instead of straight) particle deposits were occasionally observed. It was conjectured that the oscillatory deposition pattern resulted from several weaknesses in the original design, most notably that tolerances were not well controlled during assembly and that there was evidence of gas leakage around the stages. A second-generation OFVC was designed and built to address these weaknesses. The results of tests with this second-generation device are presented here.

The second-generation OFVC employs a modular design that allows for flexible testing (Figure 2-4.) Critical tolerances were tightly controlled. In particular, a single-nozzle-piece design replaced the original design in which the nozzle was assembled from two symmetric pieces (although easily manufactured, the two-piece design contributed greatly to difficulties in controlling critical tolerances each time the system was assembled for testing). The new design introduced a system of shims to allow for fine adjustment (25-μm increments) of the inlet (H) and exit (S) gaps. A variety of interchangeable rectangular nozzles were made. All of these nozzles contained 1-cm-long slits with varying widths (W = 100, 200, 300, and 400 μm) and radii (R = 600, 700, 1100, 1300, 2000, and 2600 μm) – although not all width/radius combinations were made. Several circular nozzles of varying diameters were also built, but were not tested during this project.

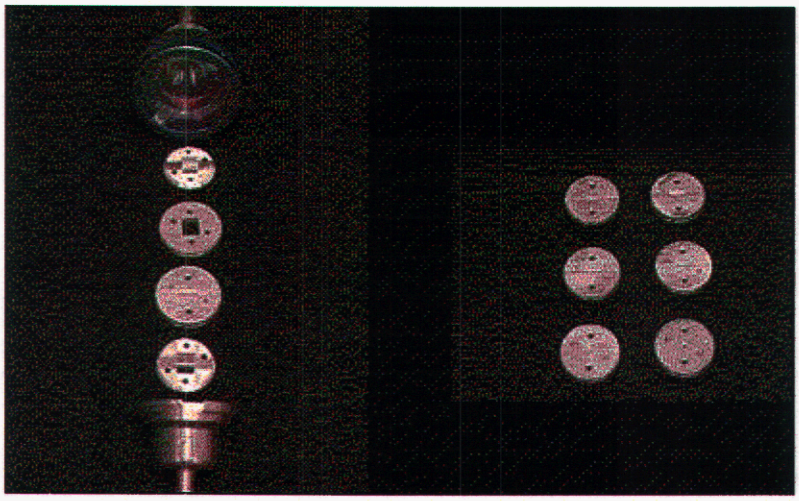

Figure 2-4 Disassembled view of modular OFVC (*left*) and assorted nozzles (*right*).

The second-generation OFVC was tested with both liquid drops and solid particles. Mono-disperse oleic acid (olive oil) drops in the range of 1–4 μm diameter were generated with the VOAG as described above. In addition, several tests were performed with solid 2 μm fluorescent Polystyrene Latex (PSL) particles (the impaction substrate was greased for these tests). A range of gas flow rates, 0.5–2 liters/min (LPM), was studied. Images of the "stripe" resulting from particles impinging on the impaction plate were photographed. For the oleic-acid drops, the

stripe was easily observable when deposited on a polished stainless-steel surface. Imaging of the PSL particles was greatly simplified by taking advantage of their fluorescence.

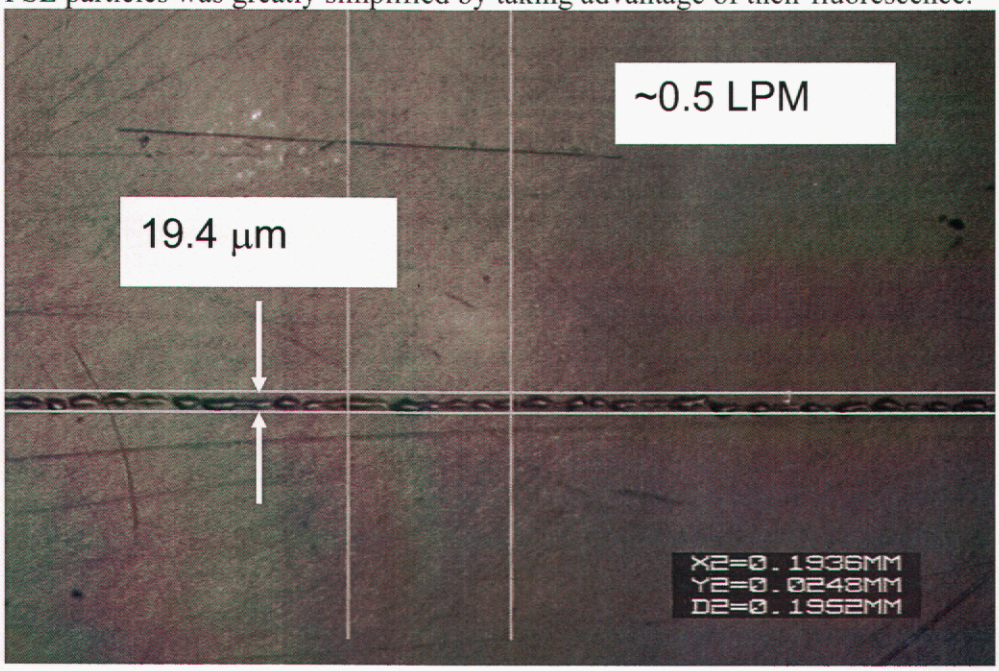

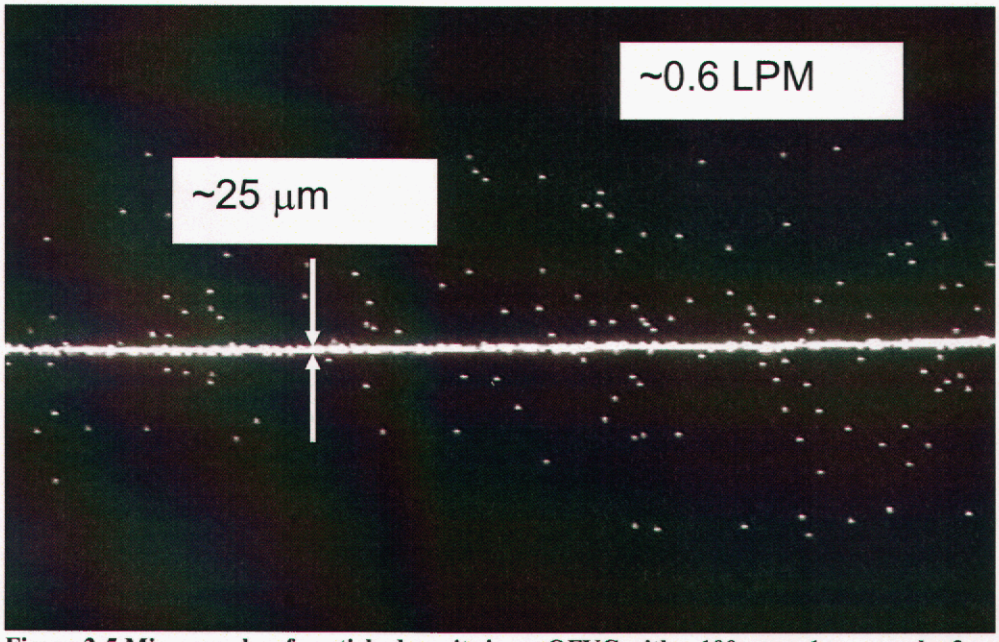

Figure 2-5 Micrographs of particle deposits in an OFVC with a 100-µm x 1-cm nozzle: 2 µm olive-oil drops (top), 2 µm PSL particles (bottom).

Images of deposited-particle stripes are shown in Figure 2-5 for 2–μm olive-oil drops and 2–μm PSL solid particles. A rectangular 100-μm-wide by 1-cm-long slit was used to deposit the particles at a nominal gas flow rate of 0.5 LPM. Both photographs show sharply linear deposits with strong evidence of particle focusing—the deposits are 20–25% of the nozzle width. A few particles are observed to lie outside the stripe for the PSL-particle tests. These are likely particles that have bounced off previously deposited particles (note that strong fluorescence signal from the build-up of particles in the stripe). Very few olive-oil droplets are observed outside the stripe, although they are admittedly more difficult to see than the fluorescent PSL particles. The significant extent of focusing that has been achieved with the OFVC can be realized by considering that the particle deposits are only ~10 particle-diameters wide.

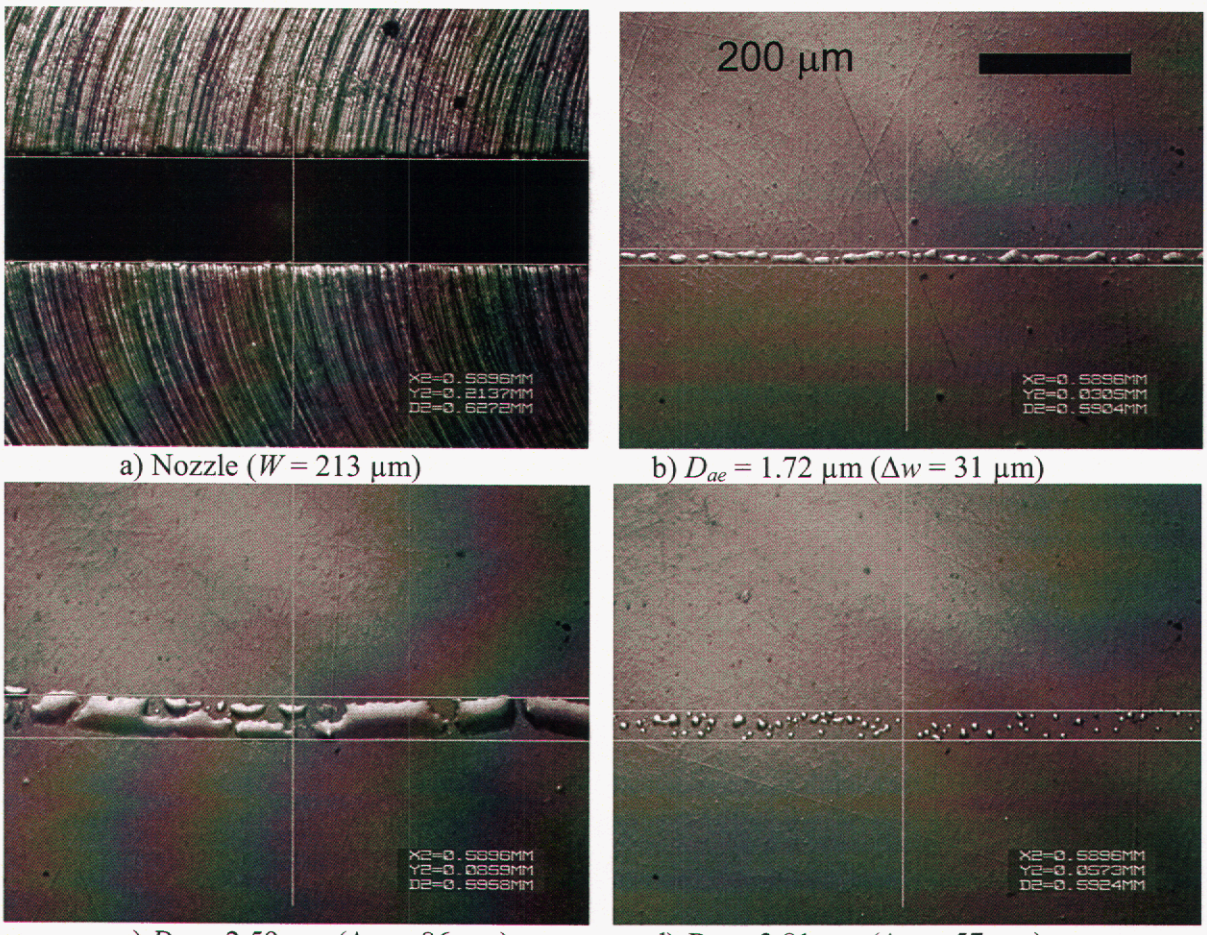

a) Nozzle (W = 213 μm)

b) D_{ae} = 1.72 μm (Δw = 31 μm)

c) D_{ae} = 2.59 μm (Δw = 86 μm)

d) D_{ae} = 3.81 μm (Δw = 57 μm)

Figure 2-6 Micrographs of exit-slit width (a) and particle-deposit widths in an OFVC (b-d) for several particle sizes.

Microscope images of the "stripe" resulting from olive-oil droplets impinging on the impaction plate were photographed for a variety of particle diameters for an OFVC flow rate of 2 LPM. Microphotographs of the particle stripe are shown in Figure 2-6*b-d* that clearly demonstrate particle focusing; for comparison, a microphotograph of the OFVC exit slit is shown under the same magnification in Figure 2-6*a*. These images show that the width of the "stripe" of deposited

oil drops was always narrower than the slit width. Particularly strong focusing for drops with aerodynamic diameters between ~1.5 and 2.0 μm. The extent of particle focusing does show some size dependence, but this is much less than observed in standard impactors. The size dependence of the particle stripe is more clearly quantified in Figure 2-7. Clearly the particle deposit is always narrower than the nozzle width, although variations with droplet size are apparent. These experiments demonstrate a key potential advantage of the OFVC design: the ability to focus and impinge particles from a user-selectable size range into region smaller than the nozzle width.

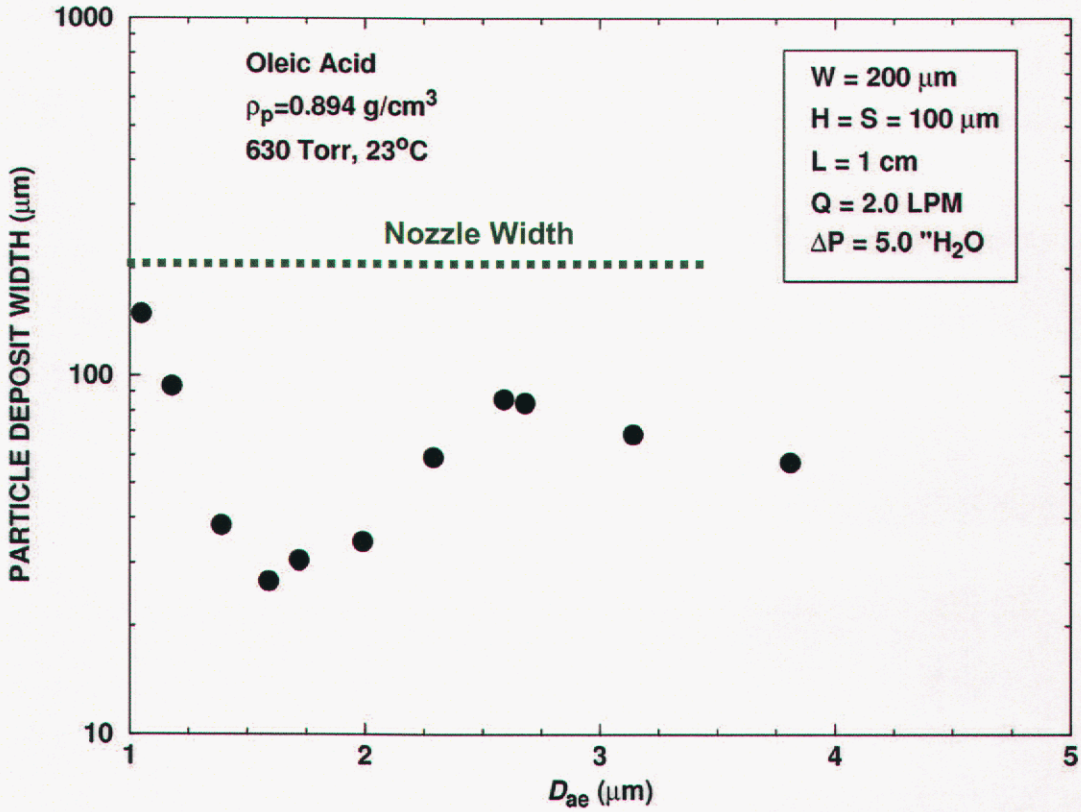

Figure 2-7 Dependence of particle deposit width on droplet aerodynamic diameter.

Although the second-generation design of the OFVC greatly improved the repeatability of measurements, "wiggly" deposits were still observed. The microphotograph in Figure 2-6*c* provides a hint of the difficulty: careful observation reveals that the particle stripe is not perfectly straight, showing small oscillations. In other tests, strong oscillations in the deposited particle stripe were observed. For example, Figure 2-8 (bottom) shows a 2 μm PSL case where the deposited stripe exhibits a strongly oscillatory pattern for a 2 LPM flow rate. The same nozzle and particles yield a linear deposit if the flow rate is reduced to 0.6 LPM (see Figure 2-8 top).

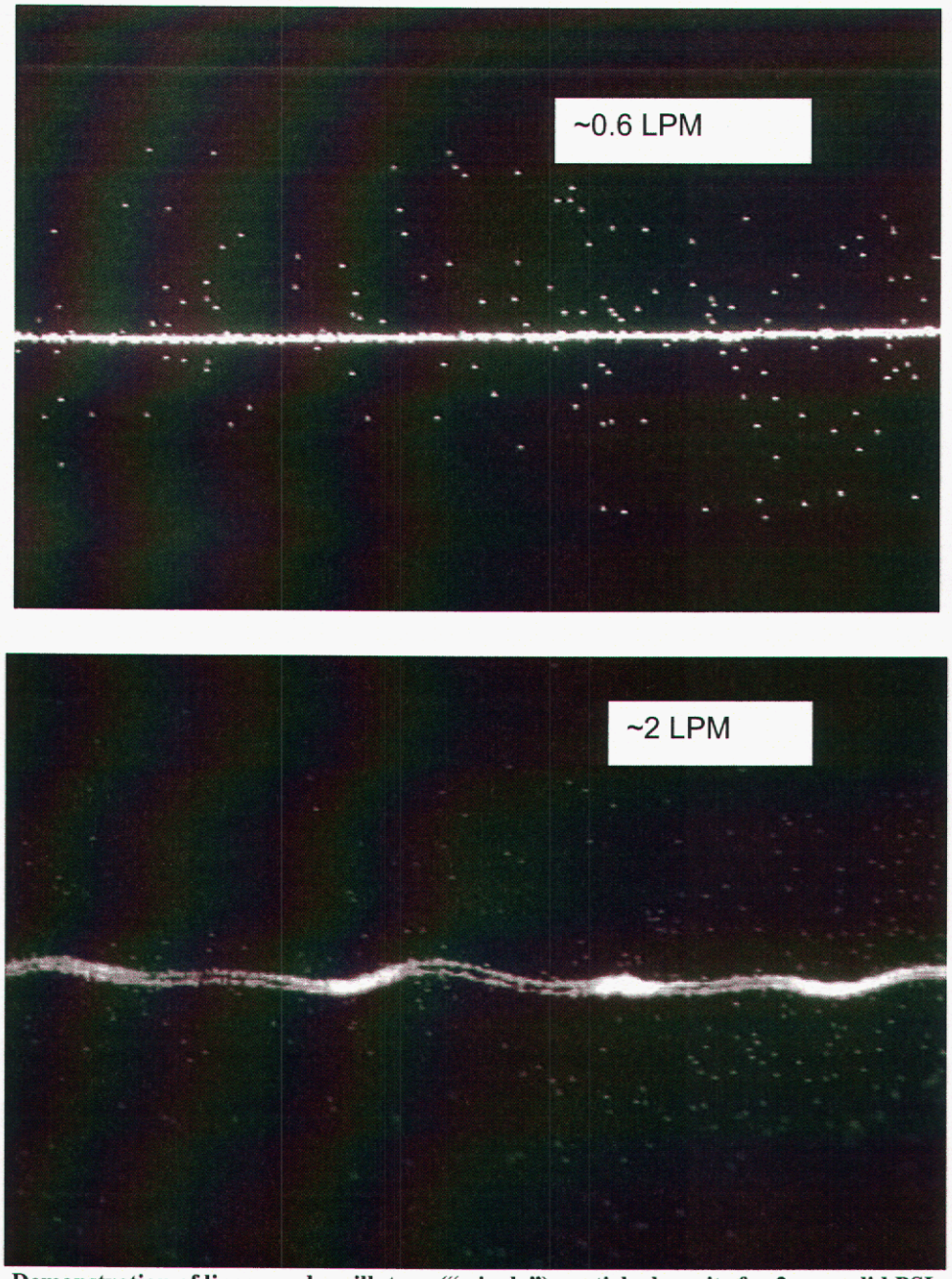

Figure 2-8 Demonstration of linear and oscillatory ("wiggly") particle deposits for 2-µm solid PSL particles. (rectangular nozzle 100-µm wide × 1-cm long)

Despite the oscillatory appearance of the stripe, particle focusing is still evident as the width of the stripe (Δw = ~25 µm) is 4× smaller than the OFVC exit slit width. The observed deposition pattern is steady in time (typical droplet exposures took from 10 to 20 seconds), indicating that the flow condition yielding the oscillation must also be steady over the exposure time. The use of small nozzle widths and low flow rates tends to suppress the appearance of the oscillatory deposition behavior, suggesting that the phenomena may be related to the flow Reynolds

number. Only a limited number of studies were conducted in the high-flow regime and the appearance of oscillatory particle deposits continues to be an open question.

Conclusions from OFVC Testing

The following conclusions can be made based on the present tests: 1) the OFVC provides sufficient particle focusing to provide particle deposits that are smaller than the nozzle width, 2) the width of the deposited stripe is much less dependent on particle size than for traditional impactors, and 3) small nozzles and low flow rates can be used to obtain linear deposits. Over certain particle-size ranges and under specific operating conditions, the extent of focusing can be dramatic – with particle deposits that are 5–10 times narrower than the nozzle width. Thus, the particle-focusing performance of the OFVC has been clearly demonstrated.

Two open issues regarding OFVC operation remain. First, future opportunities for the OFVC would be expanded if a clear physical explanation for the appearance of "wiggly" particle stripe could be found. Second, it would also be of interest to explain the observation that the extent of particle focusing shows greater particle size dependence than is predicted by theory.

Modeling of the OFVC "wiggle"

During testing of the OFVC an unexpected result was obtained for the particle deposition pattern made on a witness plate. A portion of the pattern resembled a "sine wave" (Figure 2-9), in stark contrast to the straight-line pattern that was expected and required to deposit particles in an open microchannel. The deposition pattern is over ~300 μm wide and would result in many of the particles missing the open microchannel. This asymmetric deposition pattern suggests there may be an asymmetry in the OFVC. A modeling effort was undertaken to investigate the sensitivity of the particle trajectories and deposition points to asymmetries in the OFVC.

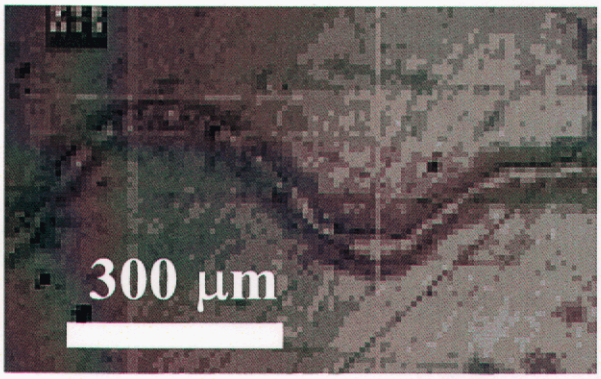

Figure 2-9 A photograph of an unexpected OFVC particle deposition pattern on a witness plate.

A two dimensional model for the OFVC cross section was constructed and used to calculate particle trajectories and deposition patterns. Various degrees of asymmetries were built into the model to determine how much the particle deposition point could be pushed off the OFVC centerline. It was found that the deposition point was very insensitive to these asymmetries.

A three dimensional model of the OFVC was also constructed that was used to study the effects of three dimensional asymmetries. The model is shown in Figure 2-10. The flow of air through the OFVC and resulting particle trajectories were calculated using this model. Various forms of asymmetry in the OFVC were considered in these calculations.

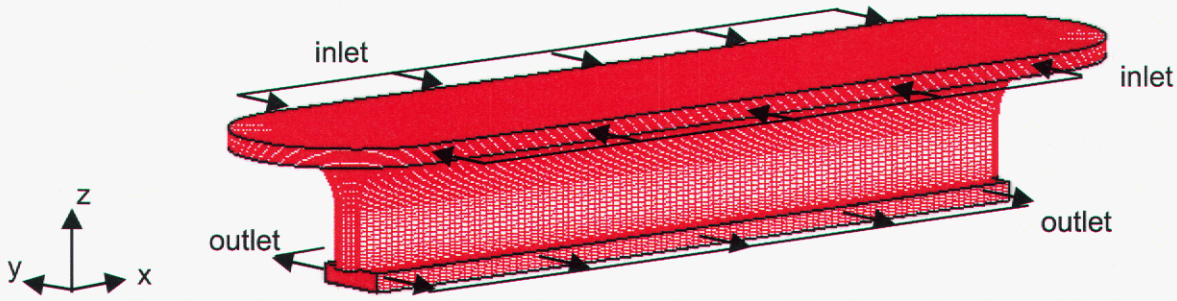

Figure 2-10 The three dimensional finite element model of the OFVC used to study the effect of asymmetries on particle deposition patterns.

One class of asymmetries considered was in the form of a velocity boundary condition specified at the inlet to the OFVC. That is, a uniform velocity was specified over the entire inlet to the OFVC except for a 500 μm long region on one side of the OFVC where the velocity was specified to be 93% of that specified everywhere else. The calculated particle deposition pattern resulting from these conditions is shown in Figure 2-11. Unlike the results for a two dimensional asymmetry, particle deposition points were found to be very sensitive to a three dimensional asymmetry. Note the similarities between the calculated deposition pattern and the experimental result shown in Figure 2-9. Thus, this appears to be a reasonable explanation for the peculiar particle deposition pattern found experimentally. A likely cause of such a localized reduction of the velocity is some sort of geometric obstruction in the inlet of the OFVC.

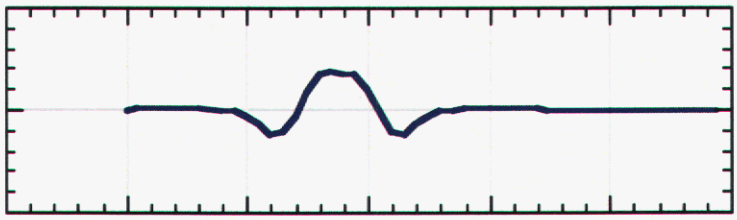

Figure 2-11 The calculated particle deposition pattern from an OFVC with an asymmetric velocity boundary condition at the inlet.

A geometric asymmetry was included in the model in the form of a small bump on one side of the OFVC near the midpoint of the inlet as shown in Figure 2-12. Such a bump could result from a fabrication defect or the deposition of debris on the inlet surface of the OFVC during the experiments.

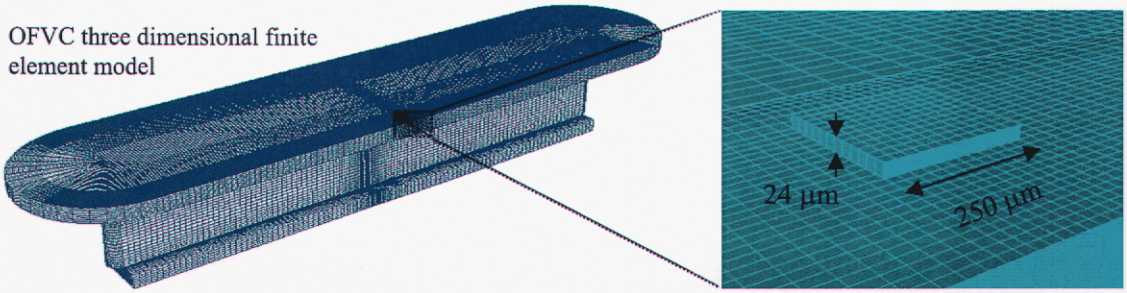

Figure 2-12 The finite element model of the OFVC with a bump at its inlet.

The resulting particle deposition pattern calculated using the model described above is shown in Figure 2-13. Again, the calculated result shows the characteristic 'sine wave' pattern seen in the experimental result. This shows that one of the requirements for focusing particles into a straight-line is that the inlet to the OFVC must be smooth, symmetric and free of debris.

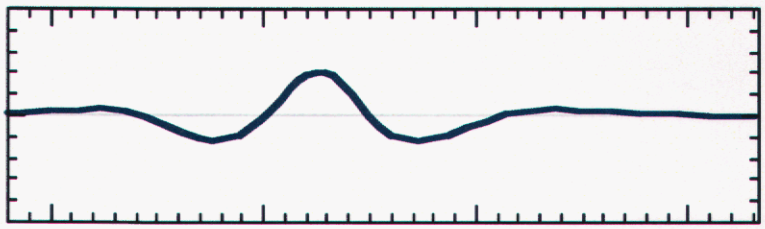

Figure 2-13 The calculated particle deposition pattern from an OFVC with a bump at its inlet.

References

1. R.N. Berglund and B.Y.H. Liu (1973) "Generation of Monodisperse Aerosol Standards," *Environ. Sci. Technol.* **7**(2): 147.

2. W.C. Hinds (1982) *Aerosol Technology: Properties, Behavior, and Measurement of Airborne Particles*, John Wiley & Sons, New York.

3. D.J. Rader, J.E. Brockmann, D.L. Ceman, and D.A. Lucero (1990) "A Method toEmploy the Aerodynamic Particle Sizer Factory Calibration under Different Operating Conditions," *Aerosol Sci. Technol.* **13**: 514.

4. D.J. Rader and J.R. Torczynski (2000) "Opposed-Flow Virtual Cyclone for Particle Concentration," U.S. Patent #6,156,212, issued December 5.

5. J.R. Torczynski and D.J. Rader (1997) "The Virtual Cyclone: a Device for Nonimpact Particle Separation," *Aerosol Sci. Technol.* **26**: 560.

6. K. Wally (2001) "Miniature Bioaerosol Concentrator: Progress Through FY2000," Sandia National Laboratories Report SAND2001-8381.

7. K. Wally (2002) "Particle 'Front End' for Compact WMD Threat Detection Systems: Integrated Microsystem Concepts for Intelligent Particle Collection, Separation, Preconcentration, and Processing," Sandia National Laboratories Report SAND2002-8586.

8. J.C. Wilson and B.Y.H. Liu (1980) "Aerodynamic particle size measurement by laser-doppler velocimetry," *J. Aerosol Sci.* **11**: 139.

This page intentionally contains only this sentence.

Chapter 3 Microimpinger Development and Testing

Introduction and Previous Work

For microseparations-based analysis and detection systems like Sandia's μChemLab, the particles separated and concentrated in the opposed flow virtual cyclone (OFVC) must be suspended in a small amount of liquid in order to carry out a chemical analysis. This can be accomplished by directing the particles to impinge into a water filled open microchannel. This is made possible by the OFVC, which focuses the particles into a narrow band less than 100 μm wide. Electro-osmosis can be used to pump the water along the microchannel, transporting the suspended particles to the sample preparation and chemical analysis system.

Direct microchannel impingement requires that an open microchannel must operate under some severe conditions and still perform as desired. The high velocity air created in the OFVC will result in relatively large evaporation rates from the microchannel. (Overall evaporation will be reduced, however, compared to conventional aerosol collectors, due to the minimal surface area for evaporation in the direct microimpingement version). To avoid microchannel dry-out, capillary forces can be harnessed to draw evaporation make-up water from a "source" reservoir. This evaporation make-up capillary flow is an additional flow, over and above the electro-osmotic flow designed to transport fluid through the microchannels. Under operational conditions, the evaporation make-up flow can become the dominant flow in the system. Therefore, the overall microfluidic system must be carefully designed to avoid a capillary-pumped reverse flow from a "sink" reservoir against the electro-osmotic forward flow. This would be unacceptable because it would prevent the transport of particles out of the channel, and might contaminate later samples.

The dynamic pressure of the air flow as it is brought to stagnation above the open microchannel must be balanced by the capillary forces due to surface tension in the microchannel. Fortunately, at the microchannel scale (100–150 μm), the capillary force derived from surface tension is adequate to this job, and microchannels can be designed to stand-off dynamic pressure, make-up evaporative losses by capillary pumping, and still, with the aide of electro-osmotic flow, maintain "forward-flow-only" operation. Science-based modeling helped gain understanding of these phenomena and to identify a successful design for the microchannel system. These modeling results were presented in our previous report (SAND2002-8586) describing microimpinger development carried out under a precursor LDRD project.

Including precursor work, two generations of microchannel structures have been investigated for the microimpinger. These include an earliest version that had been isotropically etched in fused silica wafers, a second-generation version photolithographically produced in Schott Foturan photoactivatable glass, and a second generation version micromachined in PMMA acrylic plastic. The following sections describe the testing and evaluation conducted using these second generation versions of the microimpinger.

Development Summary

The present work encompassed the fabrication and testing of two Foturan microimpinger designs. Fabrication of Foturan structures was performed for us at Sandia's Compound Semiconductor Research Laboratory (CSRL) in Albuquerque, New Mexico. Despite unforeseen Foturan fabrication process capability interruptions at the CSRL which prevented completion of all the Foturan chips we had planned, data for surface tension, evaporation, flow, and pressure were obtained from the few Foturan chips that were delivered. With the unavailability of a Foturan process during the latter part of the project, later second generation work switched to using a PMMA acrylic chip with microchannels that were machined to acceptable tolerances using subminiature conventional milling tools.

Extensive modeling was used to guide the design of the second generation microimpinger wafers. Following modeling of dynamic pressure stand-off and modeling of pressure-induced fluid flow to check the anticipated performance of the design, an OFVC package was modified to mate with an acrylic microimpinger chip plumbed for inlet and outlet flow through vias leading to the backside of the chip. The combined system was shown repeatedly to operate at various airflow rates, and yielded data related to evaporative make-up flow. Aerosolized polystyrene latex (PSL) beads were shown to be properly focused and aligned by the OFVC for direct impingement into the mated microchannel.

During this testing, an unanticipated issue was brought to light, as sub-10-μm-diameter particles were found only to impinge onto the fluid surface, never to submerge and exit into the closed outflow capillary. We identified this phenomenon as a surface tension effect and believe this phenomenon to exist in any aerosol collector wherein impingement is at modest velocity into relatively quiescent liquid. A literature survey suggested that this phenomenon had been previously encountered, observed, and modeled. Additional modeling by us supported the finding that sub-10-μm-diameter particles at velocities on the order of 10 m/s did not have enough kinetic energy to break the tension of an air-water interface. In aerosol collectors with violent agitation, or where post-collection sample processing can induce particles into suspension, this may not be an issue. But for automated aerosol collection systems intended to flow collected sample into the closed microchannels or microcapillaries of μTAS systems this issue of "surface tension capture" is a significant phenomenon which must be overcome.

Several experimental methods to induce particle submersion were then postulated and experimentally tried. Of these, only bombardment of surface-trapped particles with water droplets could reproducibly fold the particles into suspension. The project ended before we could optimize or integrate droplet impingement as a means of particle submergence. It is encouraging that a solution to the seemingly insurmountable issue of surface-tension trapping has been demonstrated since it could be employed in future systems. However, the main conclusion of this study is that the direct-impingement technique is seriously compromised by surface tension effects and alternative approaches should be taken when possible.

First Generation Microimpinger Design

In work done under an earlier LDRD project, a glass chip design with isotropically etched open microchannels was fabricated and tested (Figure 3-1). At the time of fabrication it was recognized that the resultant wider-than-deep microchannels might prove inadequate, but was pursued nonetheless as the only material and fabrication option available at the time. As feared, this earliest design proved inadequate due to the shallow aspect ratio of the microchannels, which exhibited insufficient capillary wicking to replace evaporative losses, and could not stand off dynamic pressure. A second problem with this preliminary design was complicated priming of the open microchannels due to a poorly chosen intermittent transition from closed channels to open channels. This preliminary research emphasized the absolute need for deep aspect ratio microchannels to deal with evaporation make-up and to deal with the effects of dynamic pressure. Also highlighted was the need for carefully designed transitions from closed to open channel back to closed channel.

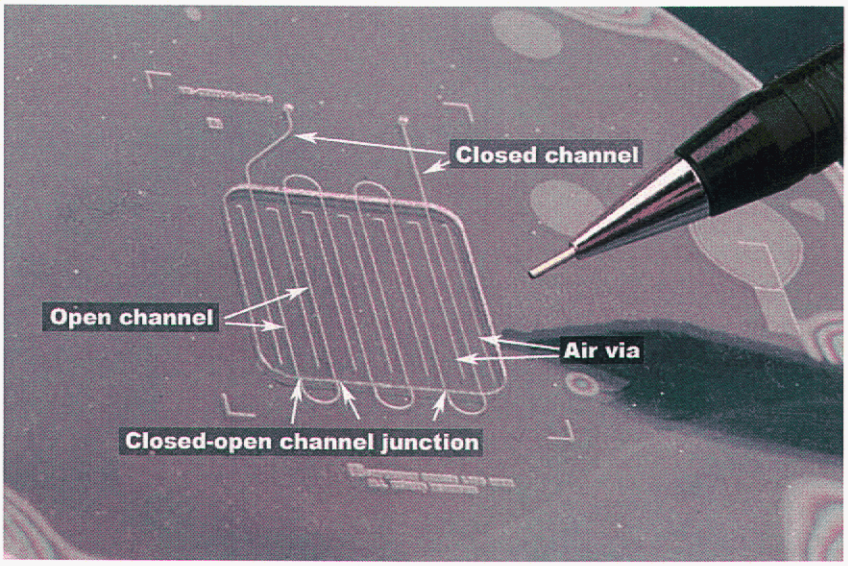

Figure 3-1 Photograph of first generation microimpinger fabricated on a glass substrate.

Second Generation Microimpinger Design

Limitations from the earliest design prompted extensive modeling to identify the degree of challenge posed by evaporation, priming, and flowing. Simulations reinforced the notion that the interplay between wicking and surface evaporation required a channel as narrow, deep, and short as possible to encourage robust wetting. The open channel surface loses relatively significant amounts water to evaporation during OFVC operation. Recession rates as large as 18 μm/s were predicted by modeling, and this water needs to replenish to avoid dry-out. Since it is wicking that draws water from either channel entrance, the hydrostatic pressure in the open channel drops to its midpoint. Surface tension at the free interface keeps the water from overflowing or underflowing the channel banks. The fluid pressure is required to remain below an upper limit at which

tension is lost and the channel overflows, as well as above a lower limit at which dry-out proceeds.

The continuum of acceptable pressures is dictated by the dimensions of the open channel aperture, and, with long, narrow channels, simply relates to the inverse of aperture width, δ. In Figure 3-2, the maximum and minimum pressures are plotted versus δ. For proper mating to an OFVC separator the practical limit of δ to accept most particles is around 25–100 μm, corresponding to minimum pressures of –0.19 to –0.75 psi. A narrow channel is most desirable for water retention. Fabrication limitations set a lower limit on minimum channel width. Channel length need only be as long as an OFVC slit required to pass the desired airflow. The longer the channel, the greater the pressure drop over its exposed length, and thus the closer the channel approaches dry-out. Depth, on the other hand, should be maximized to encourage adequate volumetric flow, but is again limited by fabrication considerations to a maximum fabrication aspect ratio. Stretching the limits of the design (*e.g.*, wider, shallower, longer channels) will put a strain on acceptable operating conditions, thereby challenging field robustness.

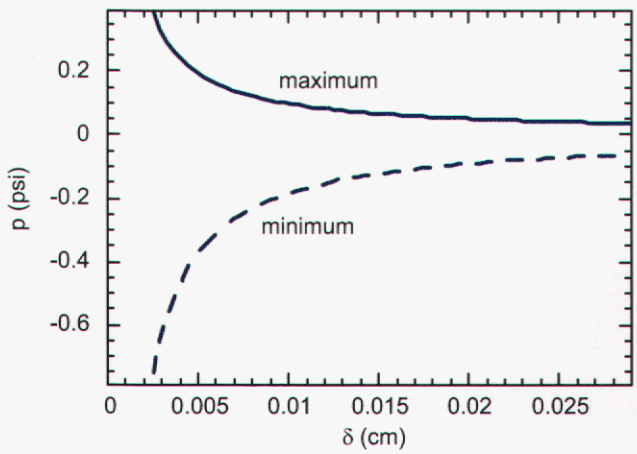

Figure 3-2 The maximum and minimum pressures that can be held by surface tension within a microchannel of width δ.

For priming, we discovered that open sections could not include any additional corners or edges that promote stray wicking. The closed-open junction could not be at wafer bond interface but, rather, needed to be through a "via" to a buried closed channel. In Figure 3-3, a comparison of old (first generation) and new (second generation) designs is shown.

The second generation design, consisting of a buried supply channel and an open access channel, could be made, as before, with two bonded wafers. We assessed designs that would allow minimal pressure drop in the open sections while encouraging dominant fluid flow from the entrance port, not the exit. Since a majority of flow would come from evaporative loss make-up, we found that a tapered supply channel could allow unrestricted flow from the source reservoir. The open-channel aperture was kept small to mitigate evaporative loss. Inclusion of a buried channel, as in Figure 3-3(b), wider than the open aperture, and possibly tapered from source end to sink end, would cut the

minimum pressure loss by a factor of eight from a deep aspect ration rectangular channel with similar aperture area. To insure a forward transport of captured bioparticles, the channel must operate with a pump. The ideal is electro-osmotic pumping from channel sidewalls and floor and/or inlet and outflow glass capillaries. For this Electrokinetic flow, channels need to be formed of an insulator and ideally have a high zeta potential with water. The other option is pressure pumping, achieved with a hydrostatic fluid head, syringe pump, hydrostaltic pump, or similar device. We prefer to pursue the electrokinetic pumping option for its simplicity.

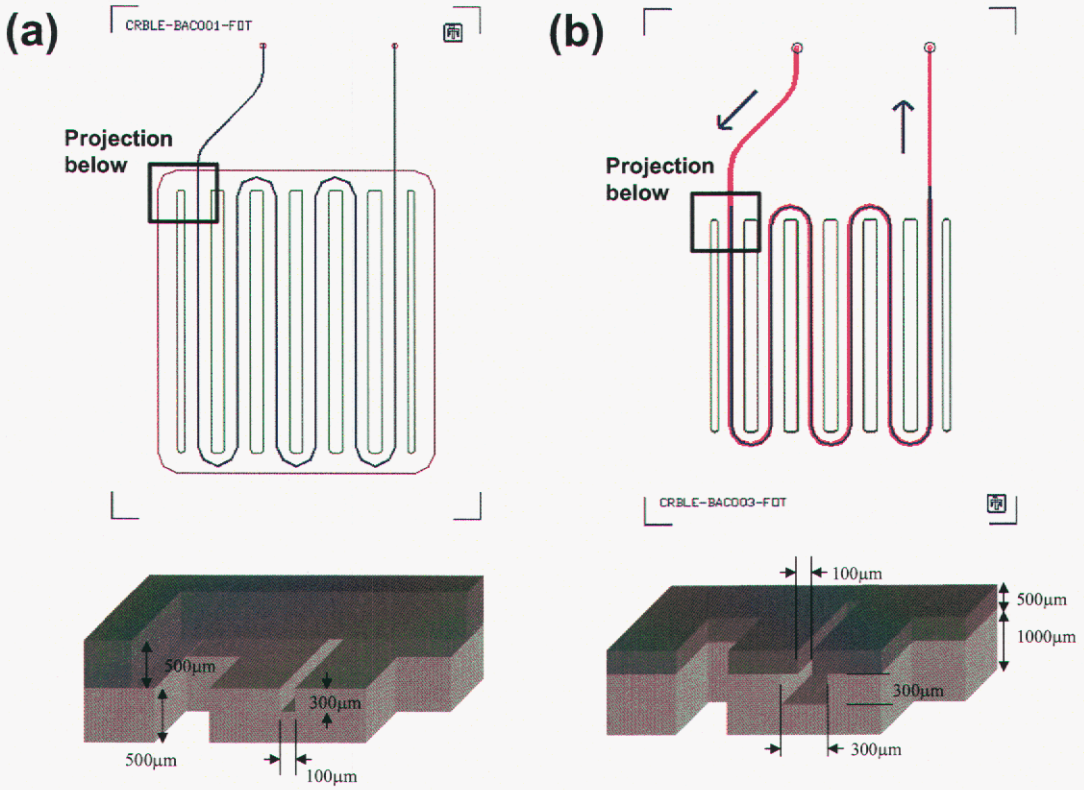

Figure 3-3 Mask layout and projection views of microimpinger chip designs. (a) First-generation glass chip; (b) second-generation Foturan chip.

Foturan Microimpinger Chips

Our specialized design requirements called for a unique fabrication process. We desired an insulating device with two channels, one buried and one surface, with channels formed using high aspect ratio techniques. Ideally, the material would also be capable of pumping water with a reasonable and reproducible zeta potential. These criteria eliminated several popular materials including silicon and glass. We chose a relatively new material for this study: Schott's Foturan® glass. Foturan is a glass matrix with embedded photo-definable silver. Instead of using a photoresist mask to transfer patterns, Foturan is directly exposed and heat cured to activate regions of interest, then etched in hydrofluoric acid. Baking transforms exposed regions into a ceramic with etch rates tens

of times greater than the unexposed glass. Therefore, aspect ratios exceeding 20:1 are possible. Furthermore, a specialized polishing and bonding technique had been developed by our colleagues at Sandia's Compound Semiconductor Research Facility. Three lithography steps (two to define channels and one to add exit vias) could be combined with a bonding step to generate the desired device. Figure 3-4 is a schematic representation of the Foturan process flow. A single published limitation of Foturan is its minimum definable feature size. Grains within the matrix generally prevent channels much narrower than 25 μm from being resolved. Our design was well within this tolerance.

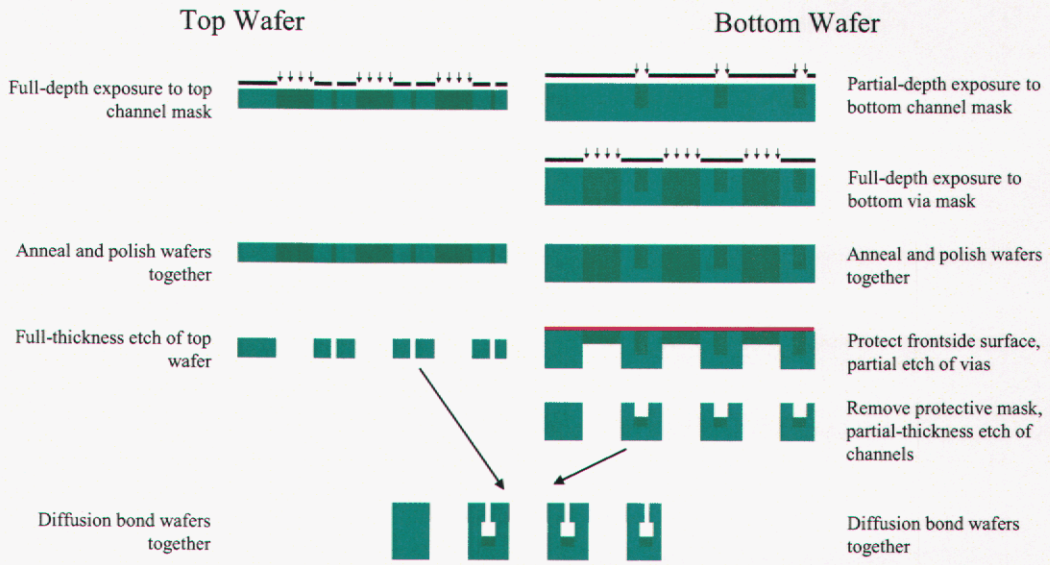

Figure 3-4 Process flow schematic for the second-generation Foturan microimpinger chip.

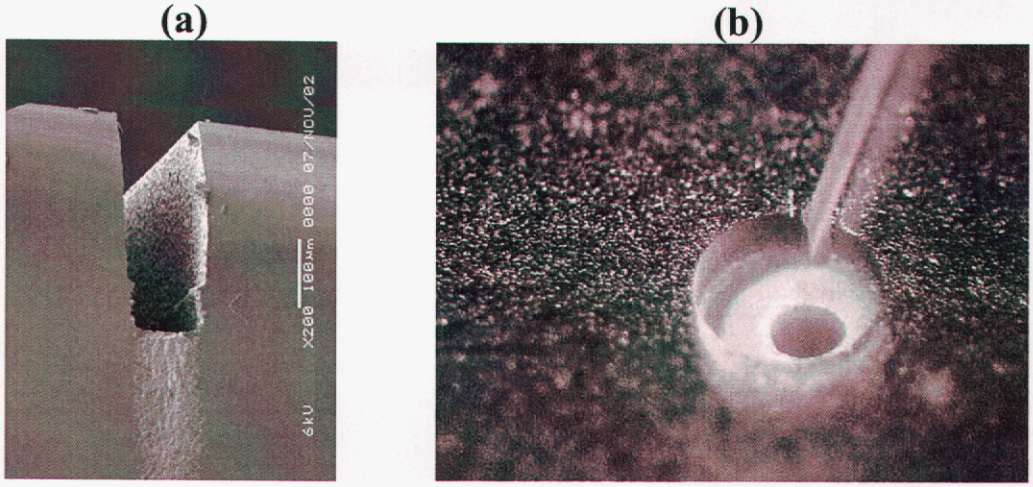

Figure 3-5 (a) SEM cross-sectional photomicrograph of a Foturan microchannel. (b) Photograph of a Foturan channel and cul-de-sac with drilled porthole.

With the assistance of the CSRL, we dedicated the first year of the project to fabrication of the second generation impinger design in Foturan. Unfortunately, the fabrication process was difficult and often subject to unforeseen complications. Problems in satisfactorily operating the Lapmaster polishing equipment ultimately resulted in the loss of Foturan processing capability for an indefinite time. Other fabrication complications arose as well. Although conceptually sound, the success of the bonding step was strongly dependant on polished surface smoothness, compressive stress caused by conversion of glass to ceramic, and a tight operable temperature regime. A bonded wafer pair was produced but with very deformed and often sealed channels.

Some Foturan test devices were created from a single mask set; these comprised simple rectangular channels. The channels were accessed through vias drilled using a 360 μm diamond-tipped bit using a CNC drilling tool, from the backside of the wafer (Figure 3-5). This run of parts was used to assess channel uniformity, surface roughness, and aspect ratio through microscope examination. Sidewall angle approximated 85° for features 100 μm wide and 300 μm deep. These wafers were intended to be the buried channels in a bonded sandwich structure; they were instead tested as unbonded open-channel elements.

Ultimately, pursuit of Foturan microimpinger chips was abandoned due to the processing difficulties. In its place, we adopted a PMMA plastic wafer microimpinger with milled microchannels.

Plastic Microimpinger Chips

In response to fabrication difficulties with Foturan we reevaluated the need for glass substrates. We discovered, through additional modeling, that Electro-osmotic pumping solely in inlet and exit capillaries could suffice to impress a forward transport of fluid sample. The substrate material still needed to be insulating yet could have nearly zero zeta potential with water. Furthermore, the same constraints on open channel dimensions applied, and a buried tapered channel was still of value for robust operation. We verified with some testing that CNC operated machining tools were capable of milling high aspect ratio microchannels into hard plastics. Although we compromised on minimum channel width, we successfully machined reproducible, burr-free channels measuring 160 μm wide and 400 μm deep. Channels were machined using a custom 0.006" endmill. Backside port connections were drilled using a 0.014" drill. The chips in this study were made in acrylic but the process would be transferable to diffusion-bondable polymers like Zeonor. Chips evaluated during the second project year had simple rectangular channels with backside capillary connections. Test chips with channel lengths ranging from 5 to 10 mm were used for our tests.

Experiments with Open Microchannels

The microimpinger relies on a flow of liquid through an open microchannel. Some experiments were carried out to gain experience operating this part of the system. The model for flow in an open microchannel, described in Ref. 3-2, provides the analytical basis for understanding the behavior of a flow in an open microchannel, while the experimental testing is described below.

Evaporation from Open Microchannels

Figure 3-6 shows the experimental set-up used for measuring evaporation rates in open channel microimpinger chips. Inlet ports were connected to source vials using glass capillaries, with vials placed on a Sartorius microbalance stage (sensitivity 10 μg) with isolated bulkhead capillary connections maintaining the enclosed quiescent airspace about the microbalance. Water lost to evaporation was measured as net mass loss in the vials. The open channel was exposed to still air and various air currents. This test was used primarily to establish a conceptual range of possible evaporation rates to expect, which were measured to vary from 1.5 μm/sec in dry, still air, to more than 10 μm/sec with air velocities of only 10 m/s.

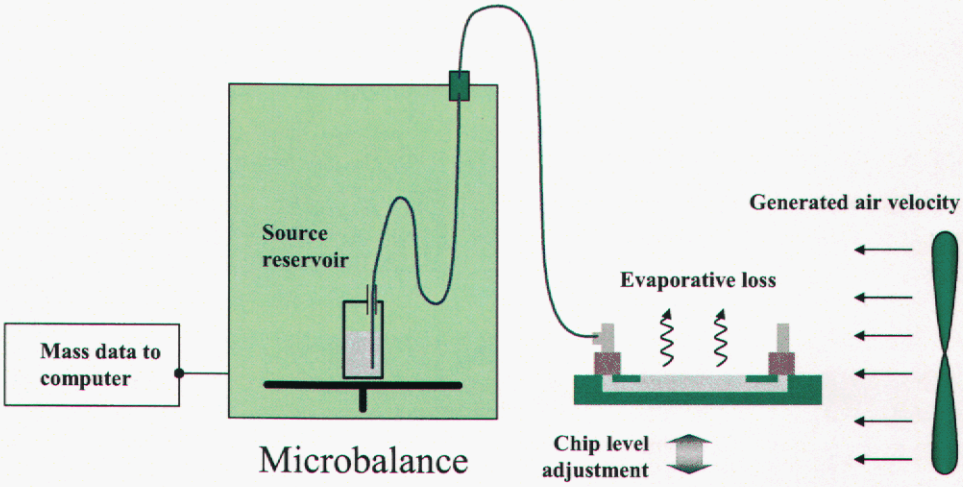

Figure 3-6 Microbalance method used to establish steady state and transient flow rate into the microimpinger chip.

Flow in Open Microchannels

Figure 3-7 shows a schematic diagram of the experimental setup for the microchannel flow experiments. Capillaries are connected to the chip on the side opposite to the open microchannel, so it was held in an inverted position, which presented no problem as surface tension easily kept liquid in the channel against the pull of gravity. The capillaries were used to connect liquid reservoirs to the chip. One of the reservoirs was raised relative to the chip while the other was lowered. This created a pressure gradient forcing liquid to flow through the chip, from the upper reservoir to the lower reservoir. The chip was positioned on a microscope so that the state of the liquid in it could be monitored.

Figure 3-7 also shows an optional particle and water sprays that could be directed at the free surface in the microchannel that were used in experiments as described later.

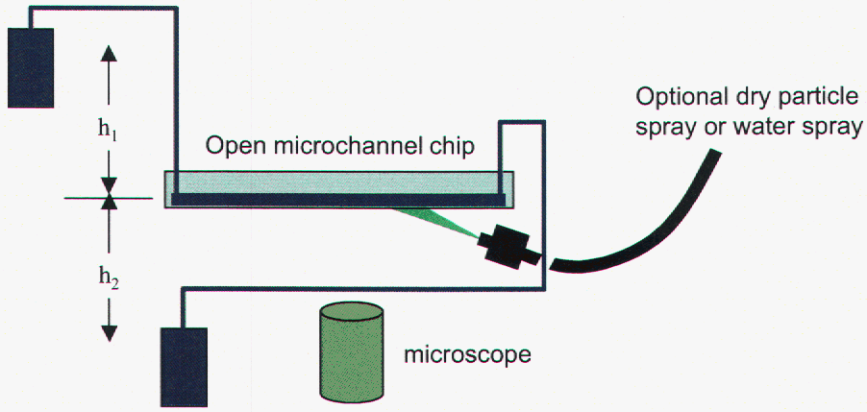

Figure 3-7 A schematic diagram of the experimental apparatus used to study liquid flow and particle submersion in an open microchannel.

The model described in Ref. 3-2 was used to calculate the range of reservoir heights that could be used without causing overflow or dry-out of the channel. The results from these calculations are shown in Figure 3-8 for two evaporation rates, 1 μm/s corresponding to quiescent laboratory conditions, and 18 μm/s corresponding to the conditions in an OFVC. For the low evaporation rate and short channel lengths used here, the upper reservoir needs to be approximately the same distance above the chip as the lower reservoir is below it. There is a small range of permissible elevations the lower reservoir may assume, to maintain the channel between overflow and dry-out conditions, as shown in Figure 3-8a. The larger these distances are, the faster the liquid flows through the channel, as shown in Figure 3-8b. Note that Figure 3-8b shows there is a region of flow reversal for the 18-μm/s evaporation rate. Thus, while it is possible to operate in this regime without overflowing or drying out, liquid will be flowing into the chip from both the source and sink ends and there will be no possibility of transporting particles out of the chip by convection. To overcome this, it would be necessary to use an elevation for the upper reservoir that is 8 inches or larger for the larger evaporation rate.

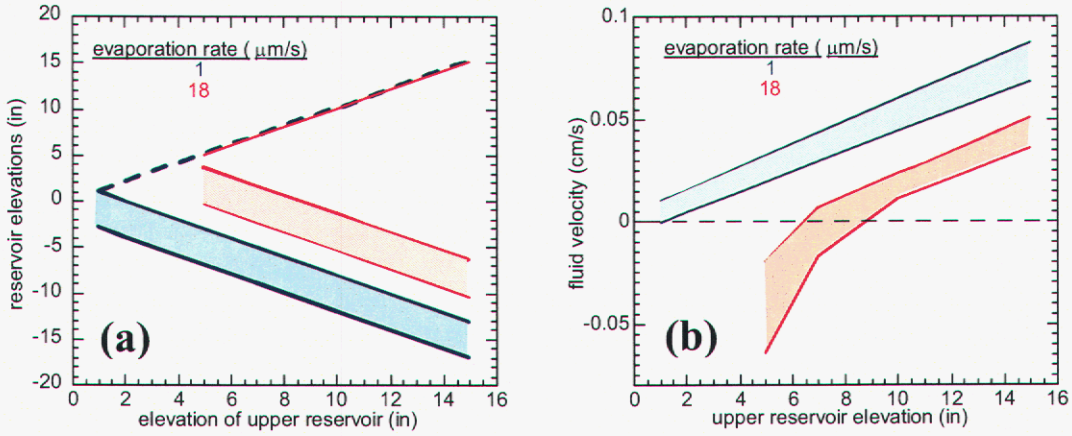

Figure 3-8 Calculated results for the liquid reservoir elevations and flow velocities that avoid overflow and dry-out of an open microchannel.

The bounds on the reservoir heights that avoid overflow and dry-out were identified experimentally by choosing an elevation for the upper reservoir, and then varying the elevation of the lower reservoir until either overflow or dry-out occurred as observed in the microscope. Overflow was observed to occur near the ends of the channel where the via hole was drilled making a 'cul-de-sac'-like geometry as shown in Figure 3-9. The first sign of overflow almost always occurred at the point of inflection near the cul-de-sac. This is because it is a weak point in the free surface, i.e. a point of negative curvature of the free surface. The onset of overflow is shown in Figure 3-9. Channel designs with smaller or no cul-de-sacs would be more robust in terms of avoiding overflow.

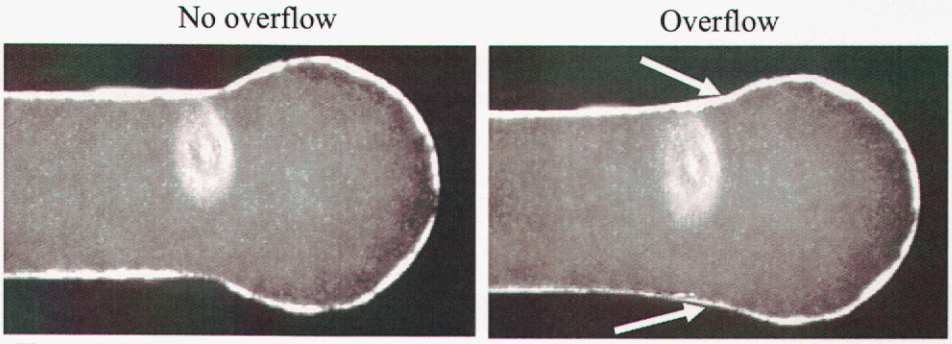

Figure 3-9 Photomicrographs of the end of an open microchannel with and without overflow. The initiation of overflow occurs at oblique corners marked by arrows.

OFVC Integration with Plastic Microimpinger Chips

The OFVC test assembly was modified to accommodate a plastic microimpinger chip. Acrylic chips were machined to replace the "nose" part onto which particles impinge, with fluid capillaries accessing the chip from below. The chip is shown in Figure 3-10, and has a single 5 mm length of channel that is manually aligned below the microseparator slit. A 100 μm slit was used to provide the narrowest focusing stripe with the most challenging aerodynamic pressure. When clasped, the OFVC assembly fit between o-rings in a modified Millipore air filter holder and capillaries exited through a bulkhead connection in the exit airstream. The capillaries both passed in front of a microscope objective before terminating at their respective reservoirs. The complete experimental setup is detailed in Figure 3-11.

A TSI, Inc. Aerosol Particle Sizer (APS) unit was used to draw air through the OFVC at constant flow rate while simultaneously measuring downstream particle counts. A bleed valve permitted air to bypass the OFVC, allowing a range of operating flowrates through the device. A solution of PSL particles were atomized in water and passed through two desiccators and a radioactive ^{85}Kr neutralizer to produce dry and relatively chargeless aerosols. During operation it was not possible to view fluid or particle behavior inside the OFVC, however we were able to monitor water flow and check for downstream particles by imaging the two capillaries. We included 200-nm red fluorescent tracer latex

particles in the reservoirs to assist with visualizing flow in the capillaries. We also measured OFVC airflow and pressure using a Gilian Gilibrator and a water-column manometer, respectively.

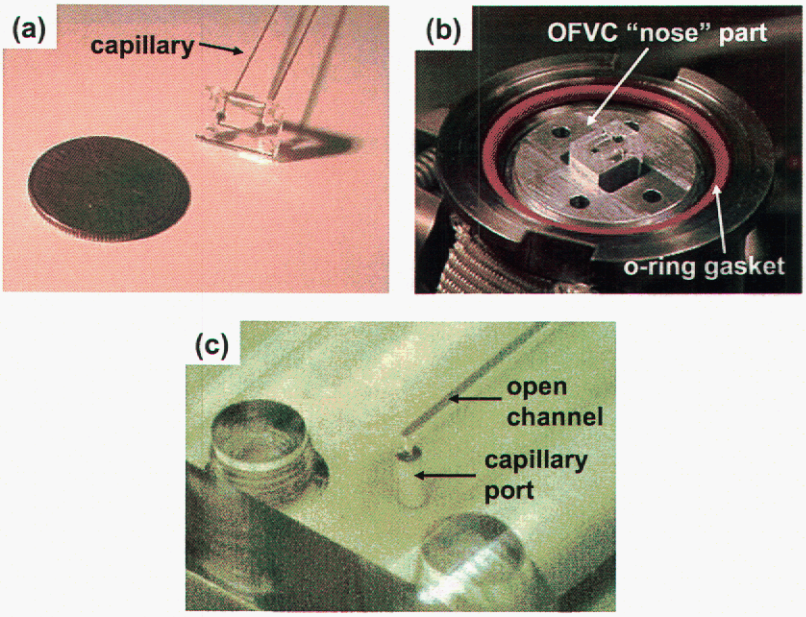

Figure 3-10 Various views of an acrylic microimpinger chip. (a) With attached capillaries, (b) mounted to the OFVC "nose" part and in place in the Millipore filter housing, (c) close-up photograph of machined features.

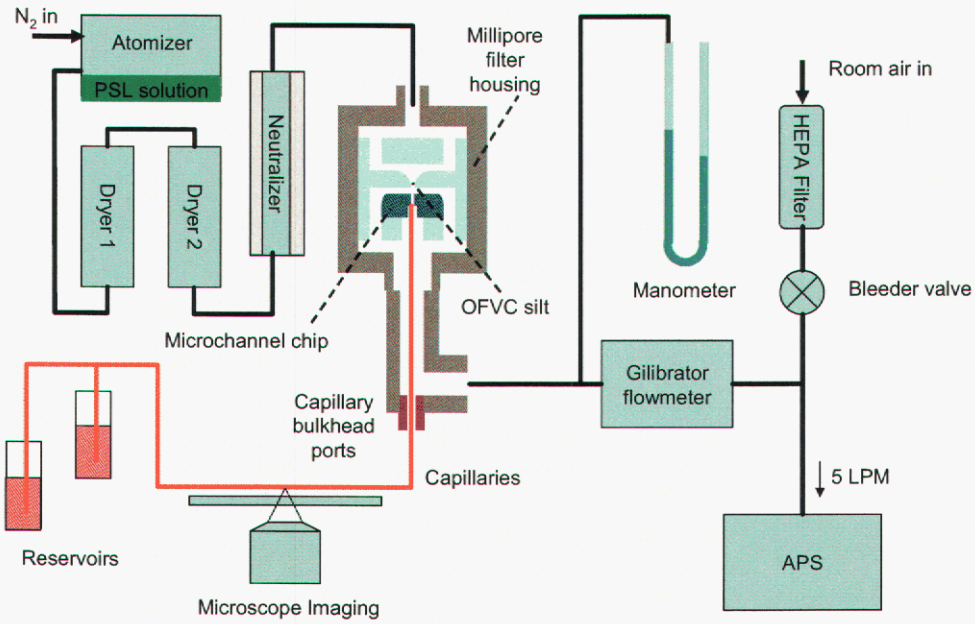

Figure 3-11 Schematic diagram of the aerosol collection and impingement experiment.

Several challenges presented themselves when preparing the chip for operation. Inherent to the modifications, the chip had to be inserted into the OFVC and capillaries threaded through the bulkhead before sealing the OFVC assembly and joining the external microscope capillaries. We first attempted to prime the chip and then join capillaries, but this invariably led to trapping bubbles and eventual flow stoppages. The better solution was to join the entire fluidic circuit and prime both entry and exit lines using a syringe. This caused channel overflow but a short blow from an air duster was enough to clear the chip surface and return water to its trap by surface tension.

We had an initial success by proving steady state water flow through the chip during operation of the OFVC. Fluid was pumped solely by hydrostatic head simply by raising and lowering the two reservoirs. Dry-out was easily discerned as a sudden stop in the outflow capillary. Overflow was manifested as a suddenly rising inflow capillary velocity, but was more difficult to ascertain. Experiment showed that only a range of reservoir heights were acceptable to keep the channel from overflowing or drying out, and this range differed greatly with and without active air flow through the microseparator. Switching on the APS pump creates a momentary instability that must be corrected by readjusting reservoir elevations to re-establish stable liquid flow. Liquid flow rates in the capillaries were also seen to change dramatically when the OFVC air flow was active. In some instances the inlet liquid flow tripled and exit flow decreased threefold.

Due to the lack of visual access, it was difficult to experimentally determine bounds on reservoir heights for avoiding overflow/dry-out for the microimpinger chip in the OFVC. The flows through the long capillaries were monitored on the microscope to provide some information on the status of the chip during operation of the OFVC. Flows were made visible by seeding them with red microspheres. After operating the microimpinger chip in the OFVC test assembly for O(10 minutes), it was disassembled for visual examination. Some determination could be made regarding channel overflow by looking for fluorescent beads covering the upper surface of the chip.

A model was developed to investigate the range of acceptable reservoir elevations needed to sustain stable liquid flows with and without the OFVC air flow. The model was used to carry out calculations for the acceptable reservoir elevations for operating the open channel in the OFVC where the large air velocities result in a much increased evaporation rate. Calculations suggested that the evaporation rate in the OFVC could be as large as 18 μm/s (see Ref. 3-2), although this depends on the relative humidity of the air. Figure 3-12 shows that for an upper reservoir height of 7 inches the lower reservoir must be between 2 inch above and 2 in below the chip to avoid overflow and dry-out. Figure 3-12a shows the pressure distribution in the inlet capillary, the chip, and the outlet capillary that would result when the upper reservoir is 7 inch above the chip and the lower reservoir is 1 inch below it. Most of the pressure drop occurs in the capillaries due to their large length. Long capillaries were required to span the distance between the OFVC and the microscope. Figure 3-12b shows the velocity distribution in the capillaries and chip.

The velocity is large and uniform in the inlet capillary. There is a large reduction in velocity in the channel due to evaporation. Velocity is small and uniform in the outlet capillary.

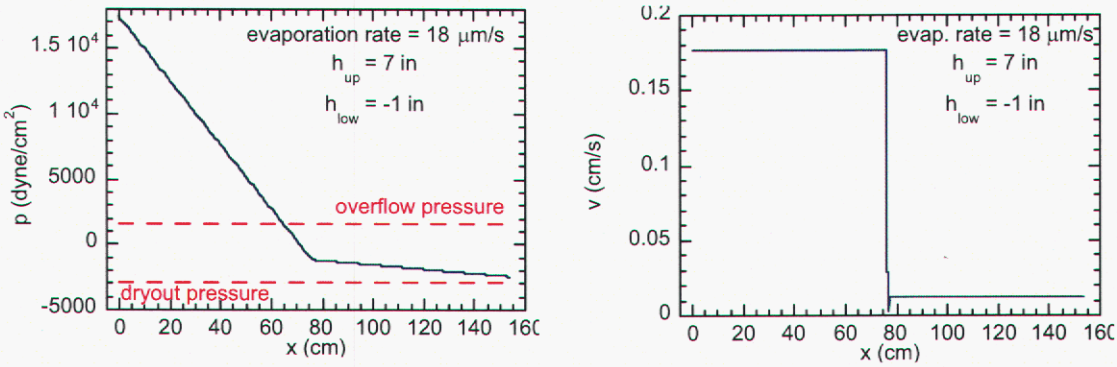

a. b.

Figure 3-12 Pressure ($p + \rho gz$) (a.) and velocity (b.) distributions in an open microchannel plus capillaries.

Experimental results for the lower reservoir elevation resulting in overflow are shown in Figure 3-13, where the results are compared with calculations for the model. The experimental results generally show that the lower reservoir must be kept below the elevation predicted by the model, which could be explained by a slightly smaller evaporation rate than that assumed in the calculations.

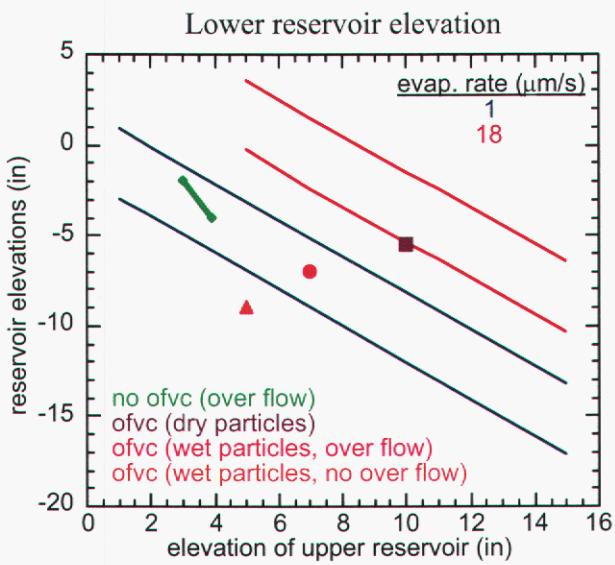

Figure 3-13 A comparison of calculated and measured liquid reservoir elevations resulting in overflow from an open microchannel.

Using these results, we were able to select upper and lower reservoir elevations that would result in stable flow operations. One of the data points shown in Figure 3-13 is for

the operation of the chip in the OFVC where the channel did not appear to dry-out or overflow. This one data point lies within the bounds predicted by the model, and identifies an operating condition where liquid flow is stable when the air flow through the OFVC is active.

Aerosol Impingement Experiments

As an aerosol simulant we adopted carboxylate-modified polystyrene latex (PSL) microspheres (Molecular Probes Fluospheres®) for all experiments. These particles are a safe, practical alternative to aerosolized bacteria, and have moderately hydrophilic surface properties much like bacteria. We chose to use 2 μm diameter green fluorescent beads and used fluorescence microscopy for visualization. Owing to their near monodispersity, the PSL particles appear in the APS as a well-defined peak with mean diameter of 2.0 μm and standard deviation less than 0.1 μm. It was a simple task to perform particle counts before and after the OFVC separator, so long as counts were normalized to measured airflows at those points. This simple experiment verified that between 50–70% of PSL particles introduced into the OFVC escaped downstream when the chip was in place and properly flowing. This is in stark contrast to the oil droplet experiments mentioned in the previous chapter, and can best be explained as a particle bounce phenomenon. Dry particles left to impinge on a flat plastic surface saw upwards of 90% particle loss. The same chip coated with a thin film of petroleum jelly brought the loss rate to between 20–30%. It appeared that the wetted channel did not act as a perfect sticky surface. For all remaining experiments in this section, the number of particles visualized in-capillary or on-surface already reflected this loss.

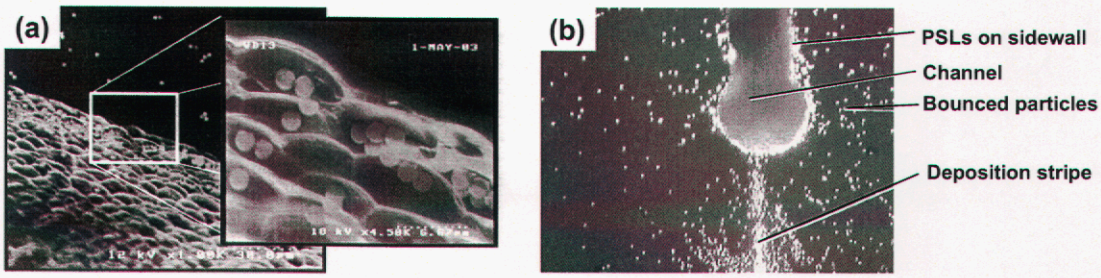

Figure 3-14 (a) SEM micrograph of PSL particles dried onto sidewall surfaces. (b) Fluorescence image of PSLs deposited onto a chip after operating the OFVC.

The first particle impingement experiments used the experimental setup shown in Figure 3-11. Channel-to-slit alignment was first verified with an initial impingement run with a dry channel. Subsequently, the channel was primed, confirmed to flow under continuous OFVC operation, and then an aerosol of PSL particles was introduced. Under repeated tests, none of the 2 μm PSL particles were observed in the outflow in the exit capillary. A number of particles were found suspended on the channel surface, again with none present in bulk solution below. Over time, these particles were seen to migrate along the

surface to the exit cul-de-sac and to channel walls. Particles reaching the walls were inexorably caught there amidst evaporation. One fact was always seen to be true: once a particle dried onto a surface the binding forces (from electrostatics as well as adhesive contaminants) were strong enough to keep the particle there despite future wetting. In Figure 3-14, an SEM photomicrograph illustrates many PSL particles stuck to the upper channel walls.

Microparticle Capture by Surface Tension

These experimental observations led us to understand that particles of less than 10 μm diameter were being captured in the surface tension of the liquid free surface. A rudimentary consideration of the various physical forces to which particles might be subjected—surface tension, inertial, gravitational, viscous drag, buoyancy, electrostatic, electrokinetic, electrophoretic, dielectrophoretic etc.—reveals that for particles of less than 10 μm diameter, i.e. microparticles, the surface tension force is by far the dominant force, exceeding all other forces, in most cases, by several orders of magnitude for particles ≤ 1 μm diameter [Ref. 3-2]. Only the inertial forces of a high velocity impingement can come close to equaling or exceeding the surface tension force. A quick survey of the literature regarding particle impingement and particle capture by surface tension led to some few references on the subject [Refs. 3-3 through 3-8], all of which reinforce our own findings. Ref. 3-3, presents a fairly comprehensive review of reported experimental investigations into "colloidal particle sorption onto a stagnant air-water interface". The authors put the findings of their review succinctly: "...a general consensus has emerged, based on the reported data, that particle sorption onto the interface is irreversible. Such irreversibility has been attributed to a capillary trapping caused by a net negative change in the interfacial energies..."

We also soon came to recognize that this microparticle capture or trapping phenomenon is not merely as an issue for our microimpinger only, but is a universal issue for <u>all</u> aerosol collectors in which small ($\leq$ 10-μm-diameter particles) particles impinge at relatively modest velocity onto quiescent liquid surfaces. For some collection purposes, this may not be a problem, e.g., collection for later bacterial culture. For the purpose of bioaerosol collection for subsequent analysis and detection in microfluidic μTAS systems, this becomes an important problem indeed. Bacteria and spores are typically <1-μm-diameter particles. Getting these species of interest into liquid suspension for subsequent transport through the microcapillaries or closed microchannels into microfluidic systems requires that the problem of microparticle capture by surface tension be successfully overcome. This phenomenon has been little considered in traditional aerosol collector design, where development has historically been largely empirical. The problem only comes to the fore for integrated microfluidic-based detection systems. These systems impose this relatively new requirement on the wet aerosol collector: that collected particles must be transported from the wet collector through microcapillaries or closed microchannels. And this requires that particles be in true submerged liquid suspension.

It is important to note that this capture of microparticles by surface tension is not a consequence or artifact of the microchannel geometry. That is, the fact that strong capillary forces are developed in a microchannel of ≤ 100 μm width does not cause or enhance the capture of microparticles. Rather it is the small size of the microparticles, ≤10 μm diameter, and the interfacial interactions between the microparticles and the liquid, which solely give rise to the surface tension forces that hold and retain the microparticles. Microparticles would be equally captured whether the liquid surface were in a large expanse or in a 100-μm-wide channel.
We observe that to successfully transport bacteria and spores in liquid microsamples through capillaries or closed microchannels, the particles must be truly *in* liquid suspension, and for that to occur, the particles must, after impingement collection, become first fully wetted and then submerged. In an ideal collector, this might be achieved in one continuous step of particle impingement at high velocity, liquid surface penetration, submergence and suspension. And so it happens rather easily for larger particles. But for microparticles of ≤ 10-μm diameter impinging at less than "hurricane" velocities, surface tension forces lead to particle capture and trapping. For these particles, which include most bacteria and spores of interest for bioaerosol agent detection instruments, steps need to be taken to assure particle submergence and suspension.

We examined this issue through modeling to determine whether direct submergence and suspension could be achieved through impingement at velocity. Our calculations supported the conclusion that dry microparticles would require a substantial amount of energy to break surface tension and submerge. Several variables are available for improving a particle's penetration efficiency. Although a major benefit is derived from decreasing surface tension, e.g., by adding a surfactant or using an alcohol, the very success of the microimpinger concept relies on adequate tension to keep water in the channel against dynamic pressure. Increasing particle velocity has a substantial benefit, but this solution is limited if target particle size selectivity of the OFVC design is to be maintained, and if dynamic pressures above the open microchannel are not to exceed those for which wicking flow may be maintained. For example, for direct submergence, a 2 μm PSL particle would likely require a 100-fold decrease in surface tension or a tenfold increase in impingement velocity. Both options are impractical to achieve in a real device.

Particle impingement calculations

The magnitude of this problem may be better appreciated by considering the equilibrium position of spherical particles in the free surface of a liquid, as shown in Figure 3-15a. Consider a particle stuck in the free surface of a liquid with a density less than that of the particle. The particle is held up by surface tension in a position partially protruding out of the liquid. Due to the weight of the particle, the surface of the liquid deforms where the angle of inclination of the free surface with respect to the horizontal at its contact point with the particle is β. A force balance between the vertical component of surface tension and the weight of the particle gives Equation 3-1 for the angle of inclination of the free

surface (assuming there is no buoyancy and the contact line is at the equator of the particle).

$$\beta = \sin^{-1}\left(\frac{\rho g D^2}{6\gamma}\right) \tag{3-1}$$

This equation shows that β decreases with the particle diameter, D. Using $D = 2$ μm, $\rho =$ 1.3 g/cc, and $\gamma = 73$ g/s^2 gives $\beta < 10^{-5}$ degrees, i.e. the deformation of the surface is negligible and the free surface may be approximated as flat. The elevation of the particle relative to the free surface is simply determined by the contact angle the liquid has with the particle.

Figure 3-15b shows the positions that hydrophobic, hydrophilic and neutral particles would have in the free surface. These are the equilibrium depths of the particles when at rest in the surface. Thus, unless the contact angle, θ, is equal to zero the particle will not spontaneously submerge into the liquid. Note that many particles are hydrophobic and have small equilibrium depths such that they ride high on the free surface.

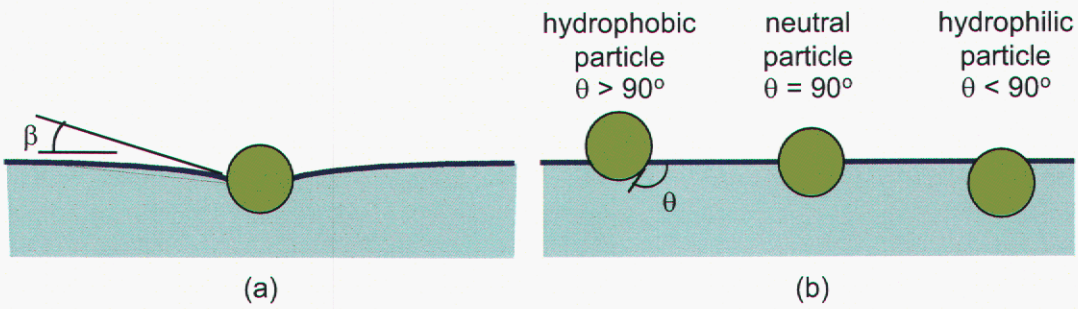

Figure 3-15 A schematic diagram showing qualitatively the free surface deformation of a liquid needed to support a particle against the pull of gravity, and the equilibrium positions of particles with different contact angles in a free surface.

Theoretically, equilibrium will only exist in static conditions, but the conditions inside the OFVC are not static. Rather, it accelerates particles to a large velocity so that when they hit the free surface of the liquid they have a non-zero momentum. Depending on the magnitude of this momentum it could be sufficient to drive the particle through the liquid free surface. A model was developed and used to determine the impact velocity required for the particle to fully penetrate the free surface. As the particle penetrates the free surface it will experience pressure, viscous shear and surface tension forces acting to resist the penetration. These fluid forces exert an impulse on the particle acting to decelerate the particle. The particle velocity is determined by integrating this impulse, as shown by Equation (3-2),

$$V = V_0 - \frac{1}{m}\sum_i \int F_i dt \tag{3-2}$$

where V is the time dependent particle velocity, V_0 is the initial particle velocity, m is the particle mass, and F_i are the fluid forces. The fluid forces will depend on how the free surface deforms during the penetration process. A general purpose finite element fluid mechanics code [Ref. 3-1] was used to calculate the free surface deformation and fluid forces.

The initial stage of the penetration process where the particle is still above its equilibrium depth is very complex. The liquid would have to be drawn upwards to satisfy the contact angle requirement. In this state the free surface would actually pull down on the particle assisting its downward motion. However, due to the short time interval required for the particle to traverse through this early penetration stage, inertia might significantly reduce the upward deformation of the liquid towards the particle and the associated downward pull that it would exert. In any case, pressure and viscous shear forces in the liquid would still resist penetration. As a way of simplifying the problem, the surface is assumed to remain flat between the time of the initial contact of the particle with the liquid and the time of the particle reaching its equilibrium depth.

The model also assumes the particle penetration process is axisymmetric, i.e. the particle impact trajectory is perpendicular to the free surface, the particle is a sphere and the particle has no rotation. The contact angle of the liquid with the particle is assumed to be constant and have a value of 110° (i.e. the particle is assumed to be hydrophobic). The location of the contact line of the free surface on the particle is determined by this contact angle and the deformation of the free surface. A shooting method is used in the calculations where the particle deceleration rate for some small time interval is guessed, and then the fluid forces on it are calculated and used to calculate the particle deceleration rate, which is compared to the guessed rate. Several iterations are taken at each step to obtain convergence.

Figure 3-16 shows the pressure and shear stress distributions in the liquid during the early stage of a 10 m/s impact by a 2 μm particle. There is a region of high pressure directly beneath the particle, and a region of lower pressure circumventing the lateral surface of the particle. The region of high pressure creates a large force resisting the particle penetration. The shear stress is large on the lateral surfaces of the particle, which also resists the particle penetration. The pressure and shear stress distributions are integrated over the surface of the particle to obtain the force on the particle for a given time. This is the force used in Equation (3-2) to get the particle velocity as a function of time.

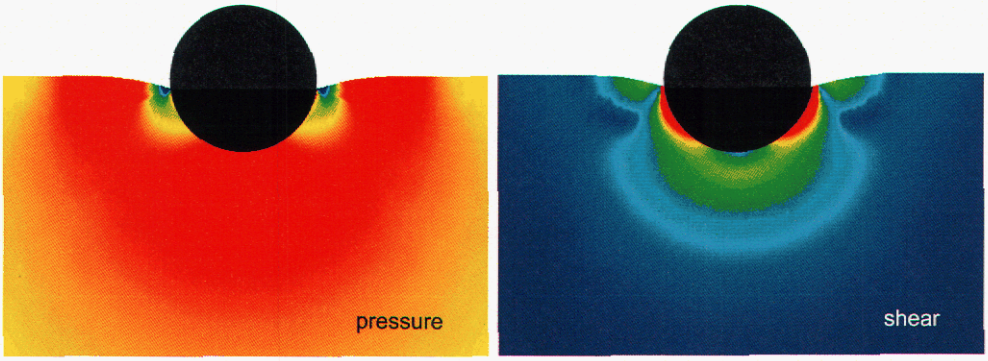

Figure 3-16 The calculated pressure and shear stress distributions in water due to the penetration of its free surface by a particle (impact velocity = 10 m/s, particle diameter = 2 μm).

Figure 3-17 shows the results of a simulation of a 2 μm particle impacting the free surface of water at 10 m/s. The figure shows a sequence of images corresponding to the particle in various stages of penetration. The second image from the top shows the particle after it has reached its "equilibrium depth" where the free surface has been kept flat up to this point. Beyond this point the free surface is allowed to deform. The last image shows the depth the particle got to after it had been decelerated to zero velocity. The simulation was stopped at this point. In reality the free surface would then snap back to a flat shape raising the particle with it, and the particle would rise relative to the free surface until it reached its equilibrium depth. So, while the momentum of a 2-μm particle impacting at 10 m/s was able to carry the particle to a depth below its equilibrium depth, it was far from sufficient to result in complete penetration of the free surface.

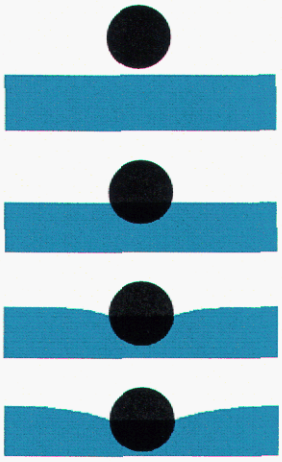

Figure 3-17 Calculated results showing a sequence of particle positions as it partially penetrates the free surface of water (impact velocity = 10 m/s, particle diameter = 2 μm).

Figure 3-18 shows the impulse imparted to the particle by pressure, viscous shear and surface tension forces. During the early portion of the penetration process pressure is the dominant force resisting penetration. Later, as the particle gets deeper into the liquid and more of the particle surface is exposed to the liquid, viscous shear becomes the largest resistance to penetration. Then, in the later stages of penetration when the free surface has deformed sufficiently to give the deformed surface a large vertical component at its contact line with the particle, the surface tension force becomes the largest resistance to penetration.

Figure 3-19 shows the effect of various parameters on the degree of particle penetration through the free surface. The degree of penetration is defined as the depth of the bottom of particle below the contact line of the free surface with the particle, divided by the particle diameter. When the degree of penetration is one the particle is fully submerged. Five cases are shown, the first referred to as the nominal case where the particle diameter is 2 μm, the impact velocity is 10 m/s, and the surface tension is 73 dyne/cm. Its degree of penetration is 0.5. The effect of decreasing the surface tension by a factor of two is to increase the degree of penetration to approximately 0.6. Decreasing the surface tension

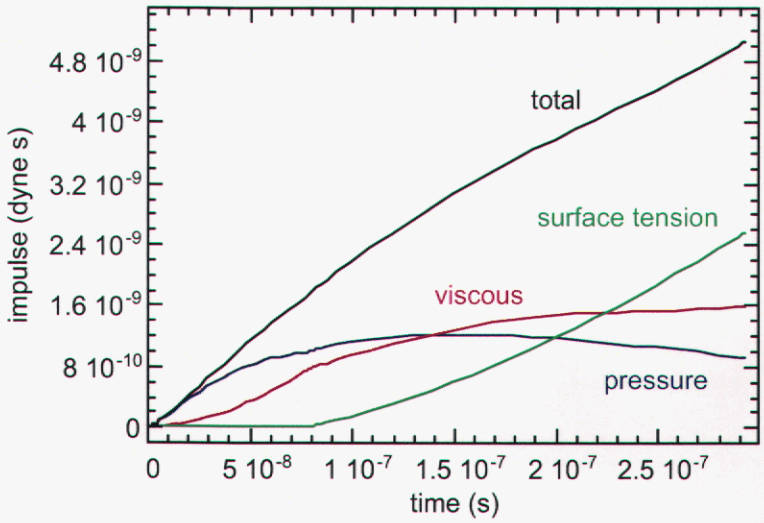

Figure 3-18 The impulse of various fluid forces on a particle as it partially penetrates the free surface of water (impact velocity = 10 m/s, particle diameter = 2 μm).

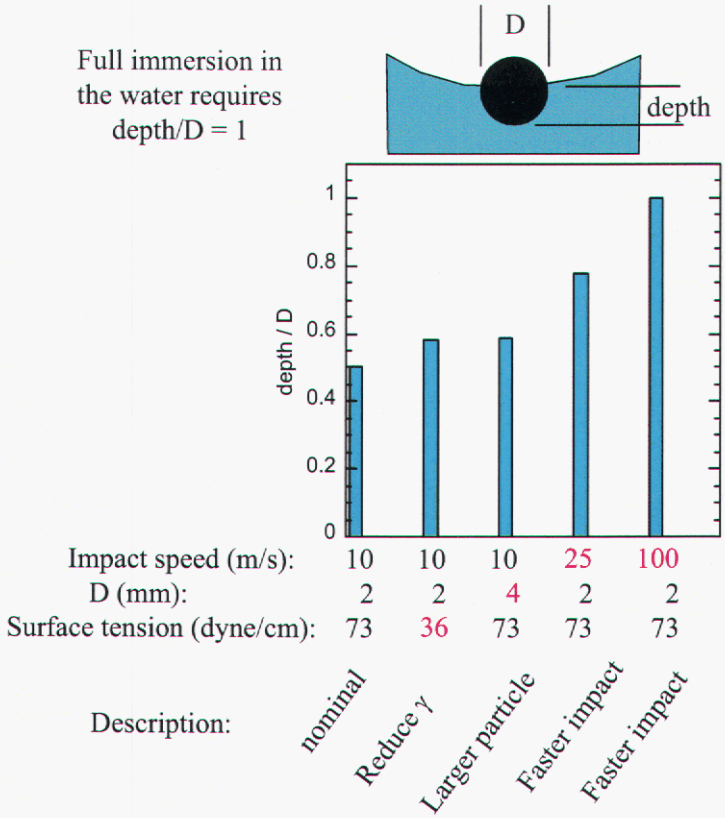

Figure 3-19 The effect of various parameters on the depth of penetration by a particle through the free surface of water.

might be accomplished by adding a surfactant to the liquid, although this would also change the contact angle, which was not included in these calculations. Increasing the particle diameter by a factor of two also results in a degree of penetration of 0.6. Increasing the impact velocity to 25 m/s gives a degree of penetration of 0.8, and an impact velocity of 100 m/s results in full penetration.

Figure 3-20 shows the large deformation of the free surface that occurs when a particle penetrates the free surface with a high impact velocity of 100 m/s. Figure 3-20a shows the pressure distribution. As was seen in Figure 3-16, there is a region of high pressure directly beneath the particle resisting its penetration. The regions of low pressure near the liquid contact line is due to surface tension acting to close the hole that has been created by the particle penetrating the liquid. The regions of high pressure in the upper regions of the free surface are due to surface tension acting on the convex portions of the free surface. The shear stress shown Figure 3-20b shows that there are regions of high shear along the lateral surfaces of the particle resisting the particle penetration. While full penetration was obtained in this latter case, an impact velocity of 100 m/s would be difficult to obtain. Consequently, methods were investigated for submerging the particles after they have been deposited in the free surface.

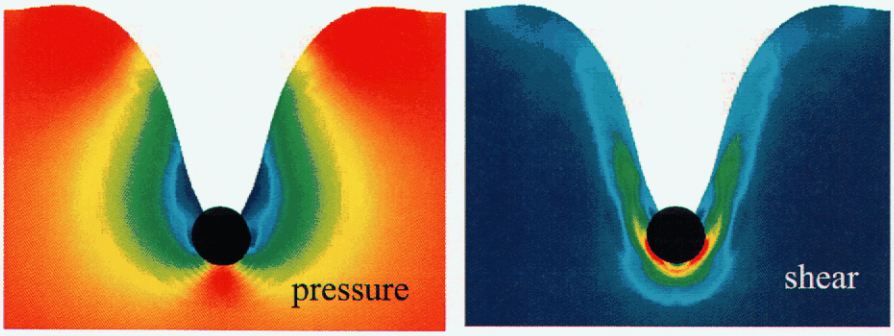

Figure 3-20 The calculated pressure and shear stress distributions in water due to the penetration of its free surface by a particle (impact velocity = 100 m/s, particle diameter = 2 μm).

Particle Submergence Strategies

Having come to understand the nature of the problem to be overcome, several strategies for particle submergence were conceived and investigated.

One set of strategies centered on our knowledge that microparticle-size liquid droplets readily merge with the liquid free surface. We theorized that if aerosol micro-particles could be fully wetted prior to impingement, the wetted particles might readily submerge and go into suspension. The efficacy of this approach was confirmed in simple experiments, wherein PSL particles in liquid suspension were sprayed from a nebulizer directly onto the open microchannel, bypassing the drying column. Wetted PSL particles were observed to readily submerge and be transported in liquid suspension. The strategy that emerged was to somehow "pre-wet" the particles prior to impingement. Schemes emphasizing this strategy included:

i) humidifying the air flow to saturation to get liquid condensation accretion onto particles. A variation of this scheme might be:

*i**) where the attempt to achieve saturation condensation, were to be restricted only to the secondary flow of concentrated particles and air from the microseparator after the particle-stripped bulk air flow has been diverted.

ii) co-mingling of the collected dry particles with liquid droplets separately introduced into the co-mingled flow to get liquid droplets to impact and wet the collected dry particles. A variant of this scheme might be:

*ii**) wetting through droplet co-mingling, restricted only to the secondary flow of concentrated particles and air from the microseparator after the particle-stripped bulk air flow has been diverted.

A second set of strategies centered on forcing the submergence of particles *after* impingement and particle capture. Based on our evaluation of the magnitude of the forces involved, this could only be achieved by defeating the surface tension forces, which requires complete wetting of the captured particles. Submergence schemes emphasizing the post-impingement wetting strategy which were considered by us included:

iii) film-wise vapor condensation onto the surface of liquid and trapped particles alike, and its variant:

*iii**) film-wise vapor condensation of a miscible low surface tension vapor (e.g. alcohol),

iv) water droplet bombardment of the trapped particles, and, its variant:

*iv**) droplet bombardment with added surfactants.

v) immobilizing particles in-situ through freezing of the microchannel, followed by film-wise vapor condensation, and its variant:

*v**) immobilization by freezing followed by droplet flooding

These post-impingement strategies had the merit that they might only need to be applied to the limited surface area of the "cul-de-sac" at the end of the open microchannel, where the surface-captured particles might be expected to accumulate. This cul-de-sac accumulation would be expected due to the underlying microfluid liquid transport flow passing down a via through the microchannel chip itself, to pass on to other closed microchannels downstream.

It might be initially supposed that any of the post-impingement wetting schemes could benefit from collection into solutions with surfactants added to reduce surface tension. However, it must be remembered that microimpinger operation depends on surface tension to 1) maintain liquid in the open microchannel against the dynamic pressure of the stagnating air stream, and 2) to wick evaporation make-up liquid to the microchannel. The addition of surfactants compromises both of these functions, and so, cannot be done without taking these performance requirements into consideration.

Some wetting schemes could be dismissed as impractical or infeasible after some consideration. For example, scheme *i*), saturation of the bulk air flow to promote condensation onto particles, was deemed impractical because it would consume too much liquid to saturate the entire bulk air flow. After all, one operational advantage leading to selection of a direct microimpingement scheme was that it reduced consumable liquid use to a minimum by absolutely minimizing evaporation losses relative to conventional wetted-cyclone aerosol collectors. Scheme *i**) was judged to be infeasible because the very short time-of-flight between the emergence of the concentrated particle stream from the microseparator and its subsequent direct impingement into the open microchannel was thought to be too brief to allow any satisfactory opportunity for humidification and condensation.

Some of the schemes were qualitatively tested experimentally, as available resources, apparatus and methodology allowed. More comprehensive testing was not possible within the limited time and resources remaining to the project. All testing used elements of the aerosol collection and impingement test apparatus described in Figure 3-11. As described in greater detail under the water droplet bombardment results below, results were judged using visual inspection, looking for evidence of surface-trapped particles, and for the inference of particle submergence, suspension, and transport derived from visual observation of particles in the microimpinger outflow.

Scheme *ii*), introducing droplets to the OFVC microseparator to co-mingle with collected dry particles, was tested using an air-pressurized nebulizer which generated droplets in the 2 – 6 micron size range. The observed result for this scheme was an occasional particle passing through the exit microcapillary, but it was clear that most particles were not colliding with droplets, and were therefore not being wetted before impingement. After more thorough consideration of the droplet concentrations that could be achieved in the nebulizer, and the resulting number counts of particles and droplets involved, it was not surprising that the probability of collisions between particles and droplets remained so very low.

Scheme *iii*), vapor condensation onto surface-trapped microparticles, was tested using a micro steam generator with superheater assembled from some borosilicate glass microtubing, a borosilicate microvial, and Nichrome resistance wire. Although we observed ample drop-wise condensation onto the liquid surface of the microchannel and its surrounds, little or no evidence of wetting and submergence could be observed for the surface-trapped microparticles. We theorize that differential hydrophilicity or differential heat transfer qualities between the water surface and particles may have limited the condensation rate at particles, so that it was insufficient to flood and wet the trapped particles.

Scheme *iv*), water droplet bombardment of surface-trapped microparticles, was tried with some limited success; these results are reported in more detail below.

Scheme *v*), freeze immobilization of surface-trapped particles, followed by vapor or liquid wetting, was tested using liquid nitrogen droplets applied to the backside of the microimpinger chip to quick freeze the microchannel, and the previously described micro steam generator as the source of condensing vapor. After several cycles of freezing and subsequent thawing under the action of the condensing vapor and heat transfer from the ambient, little or no evidence of wetting and submergence could be observed.

Water Droplet Bombardment to Force Particle Submersion

As mentioned above, droplet bombardment was the most successful of the schemes investigated to wet microparticles trapped in the liquid free surface of the microchannel by surface tension. The experimental setup is the same as that shown in Figure 3-6, where the microscope could be used to observe the particles on the liquid (water) free surface before and after they had been bombarded with water droplets. The water was seeded with 0.2 μm red fluorescent particles for flow visualization. The flow in the outlet capillary was monitored with the microscope. Green fluorescent particles 2 μm in diameter were used to simulate the aerosol particles. These were deposited in a dry state on the water free surface using an atomizer, drying column and a nozzle. The green particles on the free surface were counted before and after bombardment. The water droplets were generated using an atomizer. The size distribution of the water droplet spray was measured using an aerosol sizer. Typical droplet size distributions for various

driving pressures are shown in Figure 3-21. After bombardment the outlet capillary was monitored for green particles, which were counted using the microscope. The rate of water flow in the spray was measured before each bombardment process by directing the spray into a vial for 20 seconds and weighing it. The water flow rate was found to vary from experiment to experiment.

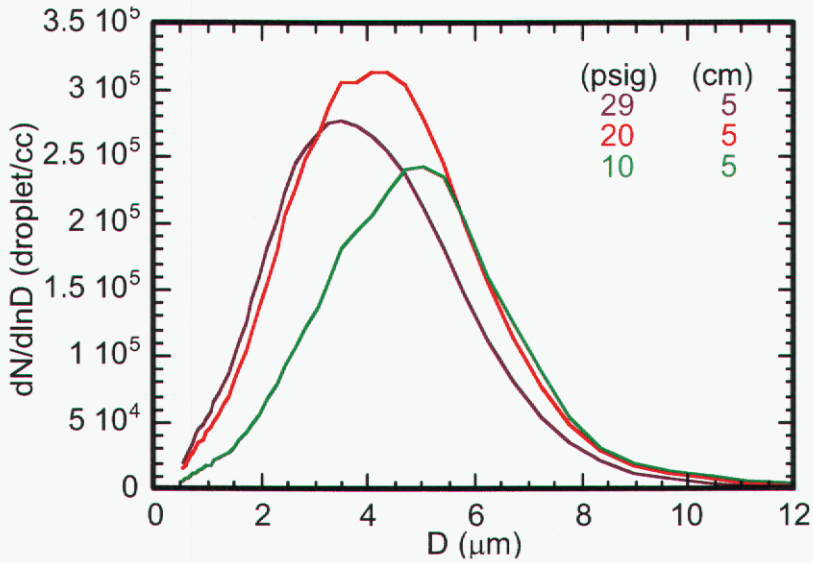

Figure 3-21 Water droplet size distributions in the sprays used to bombard and submerge particles stuck in the free surface of liquid in an open microchannel.

Figure 3-22 shows an image of the outlet capillary where several green beads are present and are easily detected against the background of red particles used to seed the flow.

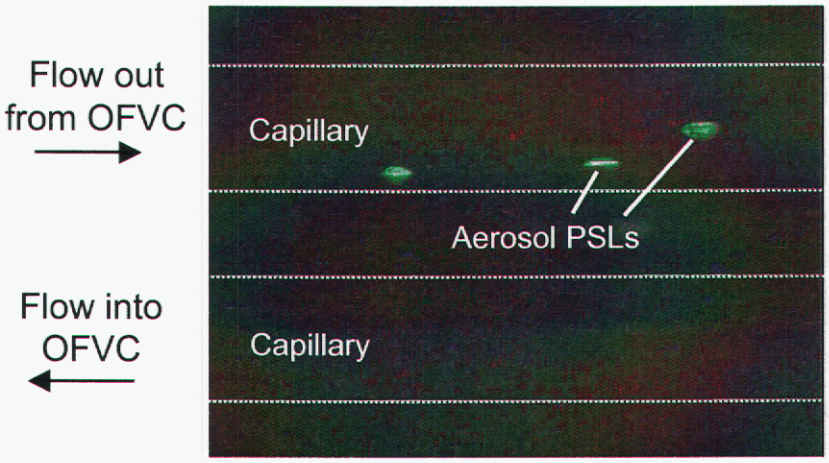

Figure 3-22 Photomicrograph showing 2 μm green fluorescent particles in the outlet capillary from an open microchannel after the particles were submerged by water droplet bombardment.

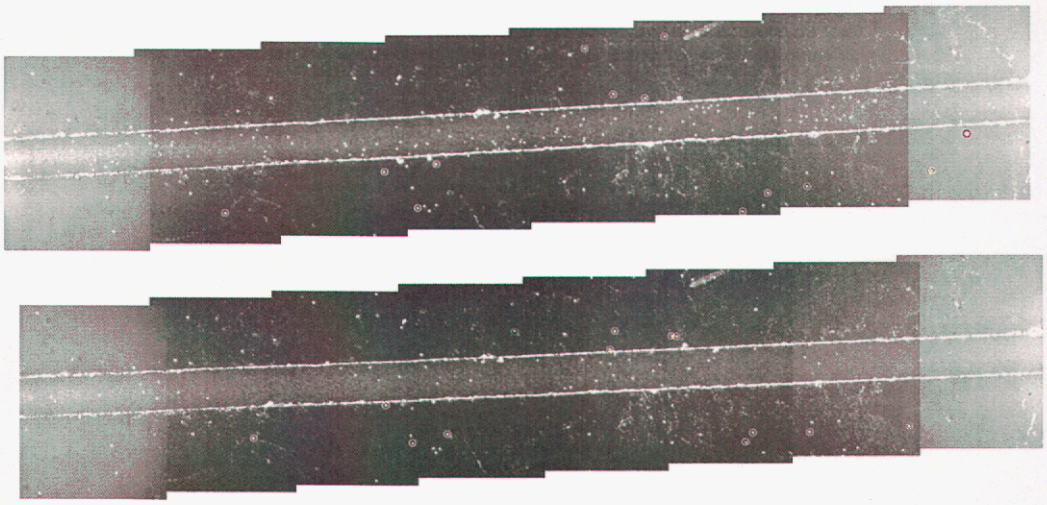

Figure 3-23 A composite photomicrograph of the open microchannel showing particles on the free surface of the water in the channel and the particles on the chip surface surrounding the channel.

Figure 3-23 shows a composite image of the open channel before and after water droplet bombardment. Actual observations through the microscope are in color making it easy to detect the green particles. The process used to deposit particles on the free surface also deposits them over the surrounding chip surface. Most of these were observed to still be in their original locations after water droplet bombardment, i.e. they did not get washed into the free channel by the water spray. The flow rate of water through the open channel appeared to be important because it determines how quickly submerged particles could be swept out of the channel before they had a chance to resurface. Other operating parameters found to be important are the flow rate of water in the bombardment spray, the distance that the spray nozzle was held from the open channel, and the duration of the spray.

Mixed results from the water droplet bombardment experiments were obtained as shown in Table 3-1. Ideally, the particles counted on the free surface after bombardment plus the particles counted in the outlet capillary should be equal to the particles counted on the free surface before bombardment. As shown in the table, the sum ranged from 72% to 122% of the count before bombardment. The particle submersion efficiency, defined as the particles counted in the outlet capillary divided by the particle count on the free surface before bombardment ranges from 2% to 116%, with an average of ~50%.

Table 4-1 Results from experiments using water droplet bombardment to submerge particles held by surface tension in the free surface of water in an open microchannel.

h_1 (cm)	h_2 (cm)	Δt (s)	Δs (cm)	spray (cc/s)	Channel Before	Channel After	Outflow Capillary	After+out before	Out before
15	22	6	1	0.0005*	32	20	16	112%	50%
15	22	10	1	0.0005*	156	10	181	122%	116%
15	22	8	1	0.0005*	122	65	49	93%	40%
15	22	8	1	0.0005*	67	47	20	100%	30%
13	15	8	1	0.0006	92	64	2	72%	2%
13	15	10	1	?	64	49	13	97%	20%
18	23	10	1	0.00075	106	104	23	120%	22%
18	23	10	1	0.00015	104	81	16	93%	15%
18	23	10	0.5	0.0001	81	72	19	112%	23%
18	23	10	0.5	0.00085	170	119	100	129%	59%
18	23	10	0.5	0.00075	129	39	60	77%	47%
18	23	10	0.5	0.00065	158	106	61	106%	39%

The reasons for the scattered results are not clear. However, as a piece of firm anecdotal evidence that water droplet bombardment does submerge particles stuck in the free surface the following observation was made during the experiments. A clump of many red particles and approximately 30 green particles was observed to be floating on the free surface. The water spray was directed at the location of this clump of particles for two seconds. Immediately following this the clump of particles was observed to be completely gone, and approximately 30 green particles were observed flowing in the outlet capillary.

Conclusions

Three iterations of microimpinger design have now been completed, replete with experiments that have both solved and unveiled several challenges related to direct microfluidic particle impingement. Through several tiers of open-channel modeling we ascertained that a very simple microimpinger chip is capable of working in conjunction with an inertial separator. For the device to work on a lab bench there is no need for electrokinetic pumping or complex channel geometry. However, a field-portable design will invariably demand much more of system robustness. Electro-osmotic pumping and buried supply channels fit into a category of safeguards that indeed will permit an open channel system to run free of overflows, dry-outs, and susceptibility to shock. Plastic chips are a cost-effective solution for mass production and ideally suited for this device, albeit hard to produce with ideal feature sizes and aspect ratios. Silicon still remains the most practical material for micromachining; patterned wafers could be electroplated into a reusable nickel master for forming plastics. This would allow a workaround from the conventional, limiting machining techniques employed in this study. Also, while the test

OFVC assembly did work in conjunction with a microimpinger chip, there were several limitations because of an inability to see the channel during operation. Certain behaviors, including overflow, particle bounce, and submergence due to bombardment, would be best to visualize during operation.

Perhaps the most pertinent findings were on the behavior and rudimentary management of particles caught in surface tension. Half of the particles from the air stream bounced off the water surface and were lost, resulting in poor capture efficiency from the very start. Moreover, we discovered that nominal incident kinetic energies of 1–10 μm particles are insufficient for direct submergence. While particles may be forced under the air-water interface with physical bombardment from water droplets, this process is, at present, neither extremely efficient nor 100% effective. Droplet bombardment may merit future study, however the approach of direct impingement is intrinsically physically unfavorable for our application and should be avoided where possible in future engineering developments.

References

1 K. Wally, E. B. Cummings, C.R. B. Ellis, M. P. Kanouff and D. J. Rader, "Particle Front End for Compact WMD Threat Detection Systems: Integrated Microsystem Concepts for Intelligent Particle Collection, Separation, Preconcentration, and Processing", SAND2002-8586, Sandia National Laboratories, 2002.

2 Masiliyah, Jacob H., "Electrokinetic Transport Phenomena", Alberta Oil Sands Technology and Research Authority, 1994

3 El-Genk, Mohammed S. and Amr. I. Abdel-Fattah, "On Colloidal Particle Sorption in a Stagnant Air-Water Interface", Advances in Colloid and Interface Science, Vol. 78, 1998, 237-266.

4 P. Gehr , S. Schurch, Y. Berthiaume, V. Im Hof, and M. Geiser, "Particle Retention in Airways by Surfactant", Journal of Aerosol Medicine, Vol. 3, no. 1, 1990, 27-43.

5 A. V. Rapacchietta, A.W. Neumann, and S. N. Omenyi, "Force and free-energy analysis of small particles at fluid interfaces. II. Spheres.", Journal of Colloid Interface Science, Vol. 59, 1977, 555-567.

6 T. R. Sosnowski, L. Gradon, A. Podgorski, "Transport of Aerosol Deposits at the Active Surface of Liquid Layer", Journal of Aerosol Science, Vol. 26, 1995, Suppl. I, pp. S541-S542.

7 T. R. Sosnowski and L. Gradon, "Behavior of hydrophilic and Hydrophobic Particles at the Monolayer of Alveolar Surfactant – A Model Study", Journal of Aerosol Science, Vol. 27, 1996, Suppl. I., pp. S501-S502.

8 A. Podgorski, and T. Sosnowski, "Dynamic Analysis of the Process of an Aerosol Particle Deposition Onto an Extracellular Lining Layer in the Human Lung", Journal of Aerosol Science, Vol. 31, 2000, Suppl. I, pp. S500-S501.

9 P.R. Schunk, P.A. Sackinger, R.R. Rao, K.S. Chen, R.A. Cairncross, T.A. Baer and D.A. Labreche, 'GOMA 2.0 – A full-newton finite element program for free and moving boundary problems with coupled fluid/solid momentum, energy, mass, and chemical species transport: User's guide", SAND97-2404, Sandia National Laboratories, 1998.

Chapter 4 The Corduroy Design Methodology for Dielectrophoretic Particle Concentration and Sorting

Introduction

Even with size selectivity and concentration in the aerosol stage, additional filtration and concentration can be needed in the liquid phase before particles in a collected sample are sized and sorted for injection into microanalytical instruments. This "hydrosol" processing can be performed a number of comparatively non-selective ways, including membrane (mechanical) concentration and electrokinetic trapping. However, these techniques typically force and immobilize particles onto surfaces where Van der Waals and other interactions can complicate the process of re-mobilizing and transporting particles to a subsequent stage. The alternative approach that was selected for this project is the use of dielectrophoresis (DEP) to collect and redirect particles from the flow. Dielectrophoresis collects via body forces exerted on the particles throughout the flow volume by non-uniform electric fields. Unlike mechanical and electrokinetic concentration which involve forces that act when particles contact surfaces, dielectrophoretic interactions occur throughout the volume and should therefore be intrinsically less susceptible to irreversible particle sticking.

A selective concentrator requires a competition between particle-specific transport phenomena. The concentrator designs considered in this LDRD employ a primary flow that flushes particle-laden liquids through a microsystem, and a secondary flow that redirects or retains particles. For selectivity either or both transport mechanisms must depend on particle properties.

Two kinds of primary flow are generally used in microsystems. One kind is advection, in which particles are simply dragged through a microsystem by a conventionally driven flow, e.g., from a pressure gradient or gravity. Another kind of primary particle flow, electrokinesis, is driven by applying an electric field along a flow channel. In the ideal electrokinetic limit typically approached by microfluidic devices, the electrokinetic velocity of an immersed particle in an applied electric field is everywhere proportional to the local electric field and the difference between its net surface charge and that of the channel boundaries. Ideal electrokinesis neither concentrates nor rarefies particles but can transport particles at speeds up to several millimeters per second through a microchannel. The simulations and data that follow employ electrokinesis as the primary flow.

The secondary flow used in this study is dielectrophoresis. As has been studied and published extensively, dielectrophoresis is a transport phenomenon that can be used to concentrate and filter particles suspended in a fluid. The dielectrophoretic force is produced by the action of an electric field gradient on the dipole moment of particles. This force is proportional to the volume of the particle, the square of the applied electric field, and the real part of the Clausius-Mossotti factor

$$CM = \frac{\tilde{\sigma}_p - \tilde{\sigma}_m}{\tilde{\sigma}_p + 2\tilde{\sigma}_m}$$

that describes the electrostatic effect of a relative difference between the complex conductivities of the particle, $\tilde{\sigma}_p = \sigma_p + i\omega\varepsilon_p$, and the suspending liquid, $\tilde{\sigma}_m = \sigma_m + i\omega\varepsilon_m$, where i is the unit imaginary number, ω is the angular frequency of the electric field in the particle frame, and σ_p and σ_m are the respective conductivities and ε_p and ε_m are the respective dielectric constants of the particles and immersion medium. At frequencies ω near zero (D.C.) this factor depends only on real conductivities. Live biological particles and spores are generally significantly less conductive than normal aqueous solutions, e.g., drinking water or buffered solutions. Thus, near or at D.C., the sign of the Clausius-Mossotti factors of these particles is negative. These particles have negative dielectrophoretic mobility. Particles that are more conductive than their immersion medium have a positive Clausius-Mossotti factor and positive dielectrophoretic mobility.

Because of its quadratic dependence on the electric field, dielectrophoretic transport dominates at sufficiently high fields. In this regime, the electrostatic potential energy of a more-conductive-liquid/less-conductive-particle system is at a minimum—and the current flowing through the system is at a maximum—when the liquid occupies the regions of high electric field and the particles occupy the regions of low electric field. The gradient of this electrostatic potential produces the dielectrophoretic force on the particles. The resulting motion of the less conductive particles away from regions of high field is called negative DEP. The opposite argument holds for particles that are more conductive than the liquid. These particles exhibit positive DEP, motion toward regions of high field.

The concentrator designs in this study work by applying a combination of electric fields (and, optionally pressure gradients) so that the secondary flow nearly balances or exceeds the primary flow for particles of interest. In a competition between dielectrophoresis and electrokinesis, this balance is adjusted simply by changing the magnitude of the applied voltage. Dielectrophoresis restrains and redirects targeted particles from the primary flow either into dielectrophoretic "traps" or "streams" depending on this flow balance.

Post-based Batch Concentrators

The design of a dielectrophoretic concentrator requires a mechanism for producing the non-uniform electric fields required to drive DEP. One approach is to produce a spatially non-uniform surface conductivity, e.g., by embedding and possibly actively driving electrodes within a flow channel. An alternative approach is to bound the flow with geometrically non-uniform insulating obstacles. This approach, called iDEP for insulator-based dielectrophoresis, is favored for its manufacturing simplicity, ease of analysis, resistance to fouling, and compatibility with electrokinetic means of transport.

We have previously tested a simple class of these designs that employ quasi-two-dimensional post-like insulating obstacles that span the floor to the ceiling of a flow

channel. These obstacles force the electric field lines to curve around them, producing the field non-uniformity. We have demonstrated >3000× concentration of bacteria, the separation of live from dead bacteria by their cell-membrane conductivity, and the separation of different types of live bacteria by their size and shape in such an array of circular posts [ref. 4-1]. Figures 4-1 and 4-2 show photomicrographs of the green fluorescence of DNA-stained *Bacillus cereus* and the red fluorescence of DNA-stained *Bacillus subtilis* at two different applied electric fields. The images were taken after the system had reached a dynamic equilibrium state: the particle "traps" are saturated so that when a new particle arrives, on average, it dislodges another particle from the trap. At the lower applied field Figure 4-1, only the *B. cereus* are immobilized. At the higher applied field (Figure 4-2), a much larger number of *B. cereus* are captured, but *B. subtilis* are also captured.

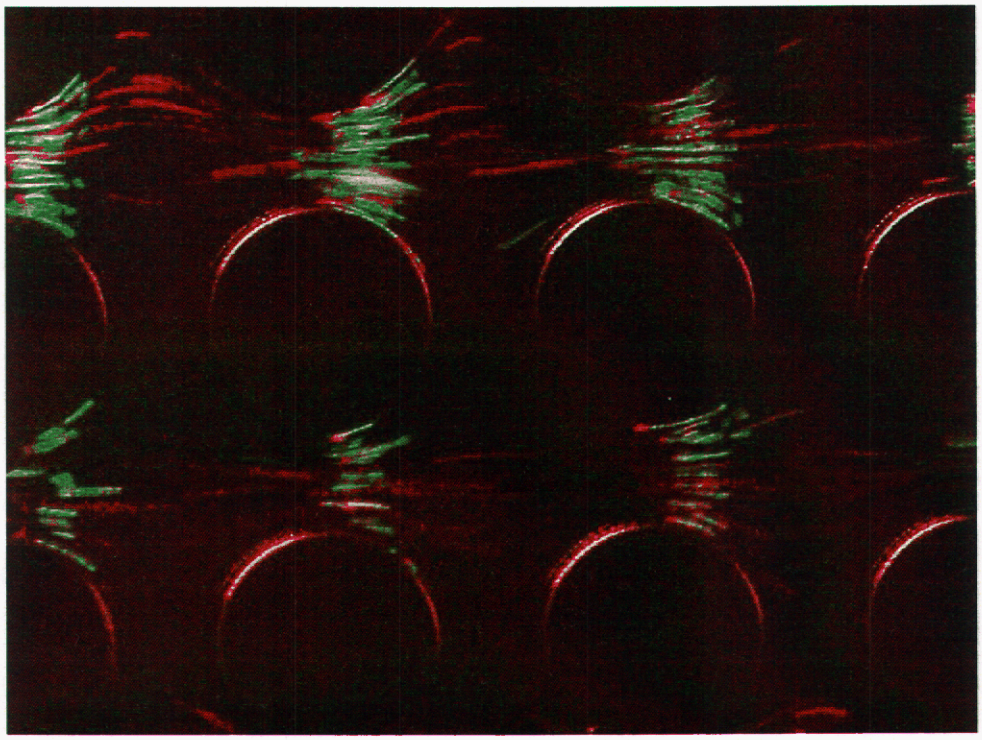

Figure 4-1 Selective dielectrophoretic trapping of B. cereus (green) vs. B. subtilis (red) in arrays of circular posts on 200-μm centers. Flow is from right to left at ~1 mm/s. Traps are fully saturated and in a dynamically steady state.

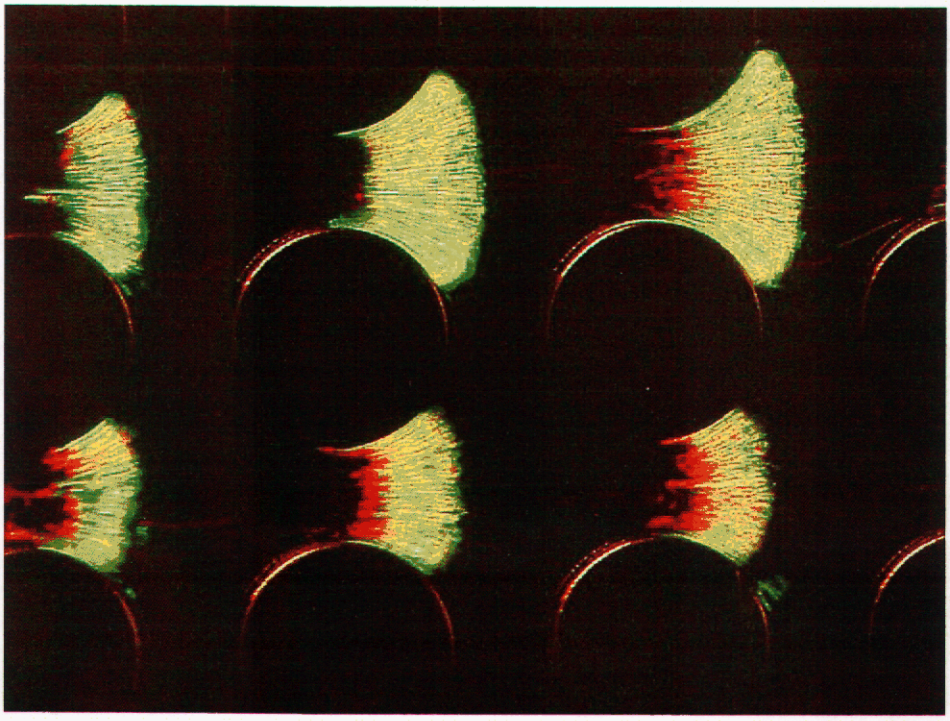

Figure 4-2 Steady-state dielectrophoretic trapping of B. cereus and B. subtilis in the same system as in Fig. 4-1, but at a 50% higher applied electric field. The capacity of the trap is significantly greater at the expense of selectivity, a general saturation problem with batch concentrators.

While different designs have different performance, all purely batch concentrator designs are limited by saturation effects. Saturation forces designers to trade selectivity for capacity. Whether the tradeoff is tolerable depends on an application, but it is untenable for needle-in-a-haystack collection, since target particles can be purged from the traps by relatively small numbers of similar background particles. Furthermore, at saturation, particle-particle interactions become dominant and particles are observed to affect the global flow field in wildly nonlinear ways by behaving like electrokinetic pumps and clogs. Precision collection and sorting devices must avoid saturation at least in critical regions.

Post-based Continuous Concentrators

One strategy to limit saturation effects is to employ continuous-flow devices. In these devices, particles are not immobilized, but dielectrophoretically redirected. Such behavior had been numerically modeled and experimentally observed in insulating-post-based devices as shown in Figure 4-3. According to these studies, the columns of posts create a pattern of dielectrophoretic potential energy bumps and dips that shuffle particles around the flow and collectively produce a barrier to passage of the particles across the columns. Depending on the post shape and particle properties, these columns of posts operate either by enhancement, in which the net effect of the field non-uniformities is to attract particles toward the post columns and depletion, in which the net effect is repulsion from the post columns.

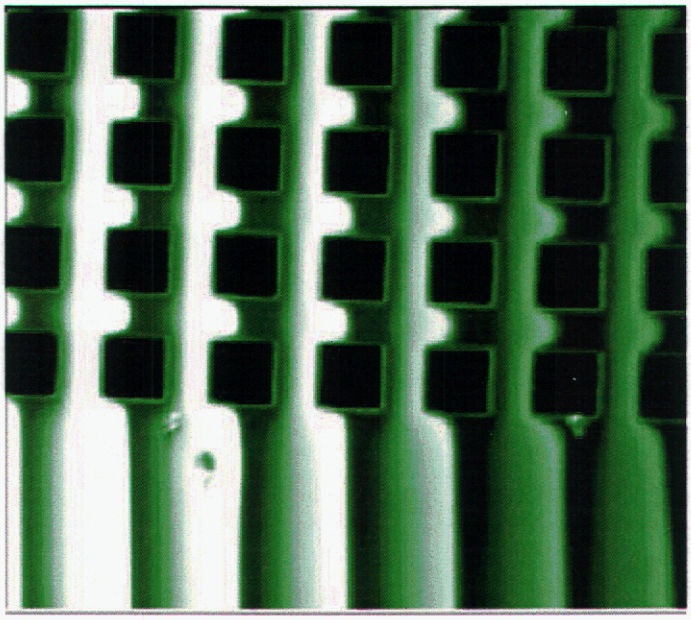

Figure 4-3 Combined electrokinetic and dielectrophoretic flow of particles down an array of insulating square posts on 63-μm centers. The posts collectively produce a potential barrier that prevents the green fluorescent 200-nm polystyrene particles, flowing from top to bottom under an applied electric field, from crossing the columns, producing the marked non-uniform concentration profile at the bottom. This effect can be exploited to produce continuous dielectrophoretic concentrators.

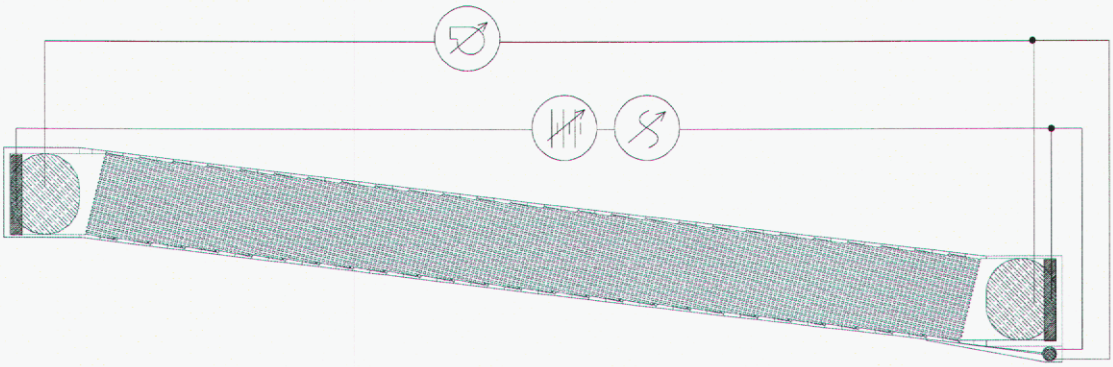

Figure 4-4 A post-based continuous-flow dielectrophoretic concentrator design. A D.C. voltage is applied from the left port to the right ports. The particle suspension enters in the left port and emerges at 160× concentration at the lower right port.

With either enhancement or depletion, when post columns are oriented at a modest angle with respect to the liquid flow, the secondary dielectrophoretic flow continuously sifts particles from the liquid passing between the posts, like in the device shown in Fig. 4-4. In this device, an electric field is applied from the left ports to the right ports. Particle-laden liquid enters the left port, the angled array of posts continuously displaces the

particles toward the lower wall of the array, and particles emerge concentrated by a factor of 160 in the lower right port.

The problem with this class of devices is that the maximum tilt angle between the primary and secondary flows is severely limited because the barrier to crossing the columns arises from a tug-of-war between potential energy bumps and dips along the columns: a particle that is attracted to the posts passes through repulsive regions while it propagates along the columns. Consequently, the net barrier potential is considerably smaller than the individual bumps and dips. This barrier cannot produce a secondary flow that is a large fraction of the primary flow without the potential energy dips turning into dielectrophoretic particle traps. This limitation on the tilt angle forces these devices to be much longer than wide. Since the dielectrophoretic interactions are sensitive to the magnitude of the applied field, the longer the device, the higher the applied voltage must be, and accordingly, the greater the thermal energy dumped to the fluid through joule heating. Beyond a certain amount of heating, the liquid temperature rises too high to preserve the sample. Thus these devices must be kept shorter than some limit and consequently narrower than some much smaller limit, severely limiting the volumetric flux the device can process without using extremely large-aspect-ratio insulating posts or some other considerable complication.

The problem of unwanted trapping in potential energy dips and the limited barrier height these features collectively produce is inherent to continuous-flow, post-based devices. It can be improved incrementally only through meticulous patterning and fabrication. Fortunately, one need not restrict the devices to two dimensions.

Facet-based Devices

While post-based designs are favorable because they can be fabricated in a single etch step and the posts double as spacers for the channel ceiling and floor, the inherent limitations of these designs motivate the development of architectures that require more complicated fabrication. Fortunately, effective device architectures exist that employ only a single additional etch step to produce quasi-planar obstacles that do not span the channel floor to ceiling. These two-and-a-half-dimensional architectures come in several varieties.

The first variety is the "facet-based" architecture. These designs utilize a methodology invented at Sandia to create channel facets having piece-wise constant-velocity regions. Interfaces between these regions are straight, abrupt channel-depth transitions, generally tilted according to a trigonometric compatibility relation with respect to the flow direction in the channels. At these interfaces, the velocity and electric field abruptly jumps in value. A nice feature of these designs is that you can simply and rigorously engineer the magnitude of the jump and consequently the dielectrophoretic force on particles at the interfaces. Depending on the design, the particle properties, and the applied field, particles will either be dielectrophoretically restrained or free to cross the interface. If the interface is tilted, the particles are not restrained from propagating downstream parallel to the interface, as shown in Fig 4-5. The end of the interface can

truncate at a wall that traps particles until the field is reduced or can be modified to spill particles continuously in a concentrated stream. These faceted devices are promising and the subject of further development in another LDRD. The primary limitation of this methodology is the geometrical constraint imposed by the compatibility condition for obtaining piecewise uniform (or controlled nonuniform) fields.

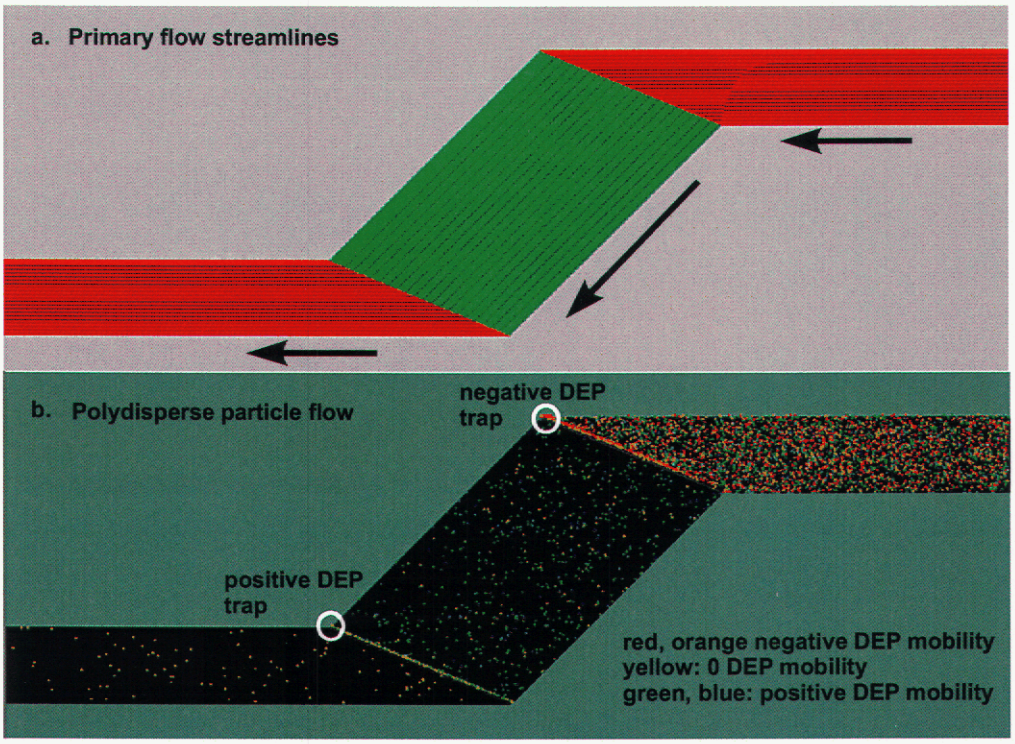

Figure 4-5 A facet-based dielectrophoretic concentrator. The central parallelogram region is etched shallower than the entry and exit regions, creating an abrupt interface. Particles having a sufficiently large negative dielectrophoretic mobility (colored red and orange) are restrained from entering the central facet. They propagate along the interface until they accumulate in the corner indicated by the circle. Particles having sufficiently large positive dielectrophoretic mobility (colored green and blue) are restrained from leaving the interface just past the central facet. They collect where indicated by the second circle. Particles whose mobility is sufficiently low (colored yellow) pass unimpeded through the system.

Corduroy-based Devices

In an effort to free the designer of the compatibility constraint and the need for simulation to assist with design, a new methodology was developed called the "corduroy methodology" after the appearance of channels that are patterned in arrays of the corduroy obstacles. This methodology supports continuous and hybrid continuous and batch processors. The corduroy methodology supports the design of extremely simple or exquisitely complicated concentrators and advanced devices like particle spectrometers. The best feature of the methodology is that it is intuitable and can therefore be used widely as the basis for further invention and development. The following sections develop the theory of the methodology and a set of sample devices.

The Corduroy Design Methodology

The problem of developing an iDEP design methodology is an exercise in crafting obstacle shapes and arrangements that are manufacturable, that can be engineered to perform useful functions reasonably, and that offer a sufficient level of performance to be practically interesting and useful. One particularly useful obstacle geometry is called for convenience a corduroy obstacle because of the resemblance to corduroy material when such obstacles are arranged in arrays. Corduroy obstacles appear as ridges and valleys of an insulating channel boundary. They can be employed individually or as a system of obstacles to compose a device. The devices described herein use these corduroy ridges and valleys to produce low-electrostatic-energy sluices, spillways, and dams that channel, deflect, remove, or collect selected particles from the bulk liquid flow, enabling a range of practical devices for processing samples. These corduroy designs can perform their filtration/concentration function in a continuous-flow mode, a batch mode in which particles are sequentially immobilized and released, or in a hybrid of these modes.

The manipulation of particles in the corduroy devices involves a competition between dielectrophoretic force fields that tend to draw particles into and confine particles to dielectrophoretic potential wells and repel particles from dielectrophoretic potential barriers and "mobilization fields" associated with a primary flow that tend to move the particles through the system with a bulk flow. In this LDRD, the mobilization field is a near-D.C. or D.C. electric field that drives electrokinesis or a pressure gradient field that drives advection.

Interaction of a Particle with a Corduroy Obstacle

A derivation and discussion of the theory behind the corduroy design methodology appears in ref. 4-2. Briefly, when competing electrokinesis with dielectrophoresis, the theory shows that there is a threshold dielectrophoretic mobility below which particles are free to cross ridges and valleys and above which particles are inhibited from crossing or leaving a ridge or valley. The inhibited particles slide along a ridge or valley if there is a component of the electrokinetic flow along the obstacle. Particles that are less conductive than the immersion liquid are inhibited at the upstream side of a ridge as a result of negative DEP. Particles that are more conductive than the immersion liquid are inhibited at the downstream edge of a ridge. This behavior is shown in the numerical simulations in Figure 4-6. The opposite behavior occurs for valley obstacles, as shown in the numerical simulations in Figure 4-7. This inhibition threshold scales inversely with the applied electric field and the cosine of the angle that the ridge makes with respect to the flow. This angular dependence is useful for engineering systems and is intuitive: to release particles at the end of a ridge one need only turn the ridge downstream and particles will spill out. This kind of termination is employed in Figure 4-8, a simple continuous-flow corduroy concentrator. Alternatively, to trap particles, one may turn the ridge upstream and form a cup.

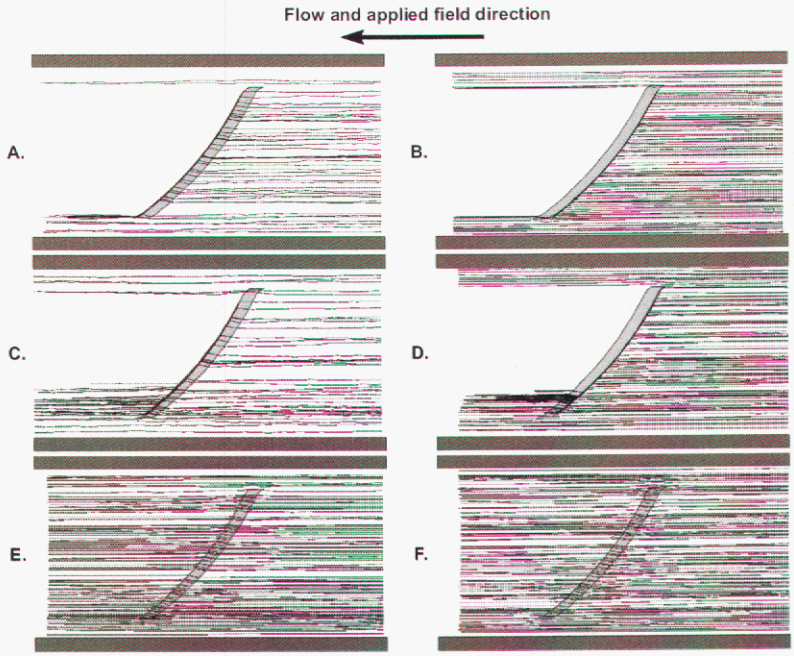

Figure 4-6 Numerical simulations of particle motion past a corduroy ridge obstacle. (A.) High positive DEP mobility; (B.) High negative DEP mobility; (C.) Medium positive DEP mobility; (D.) Medium negative DEP mobility; (E.) Low positive DEP mobility; (F.) Low negative DEP mobility.

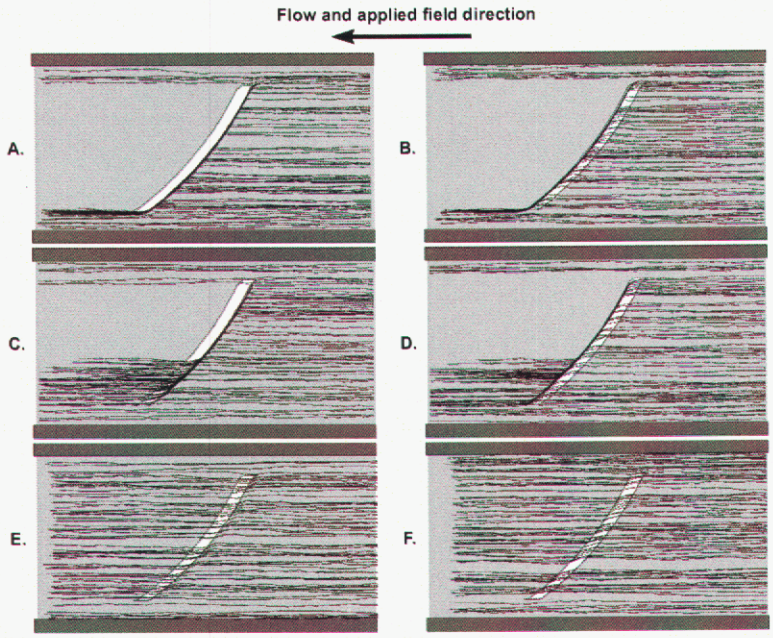

Figure 4-7 Numerical simulations of particle motion past a corduroy valley obstacle. (A.) High positive DEP mobility; (B.) High negative DEP mobility; (C.) Medium positive DEP mobility; (D.) Medium negative DEP mobility; (E.) Low positive DEP mobility; (F.) Low negative DEP mobility. Note how the behavior is the opposite of that for the corduroy ridge obstacles.

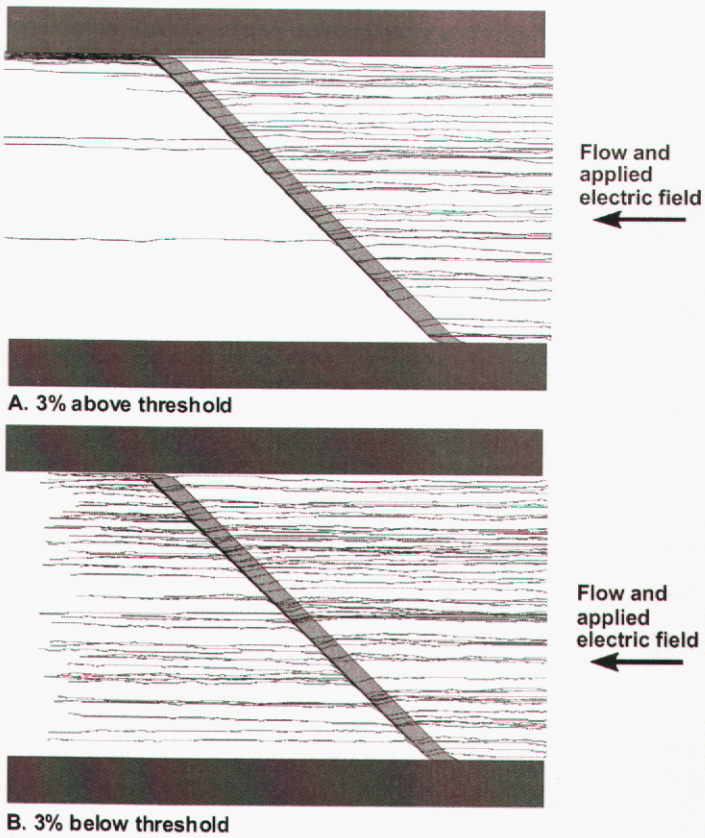

Figure 4-8 Filter/concentrator response of a straight-central-section obstacle. Because both the channel and obstacle are straight, the inhibition threshold does not vary along the central section. (A.) Particle DEP mobility is 3% above the inhibition threshold. (B.) Particle DEP mobility is 3% below the inhibition threshold.

Spectrometers can be fashioned from curved ridges as shown in the simulation in Figure 4-9. The simple DEP particle spectrometer consists of a spatial concentrator stage (right obstacle) and a dispersive stage (left curved obstacle). Particles detach or spill into bands of constant DEP mobility from the obstacle where its incidence angle exceeds a threshold value.

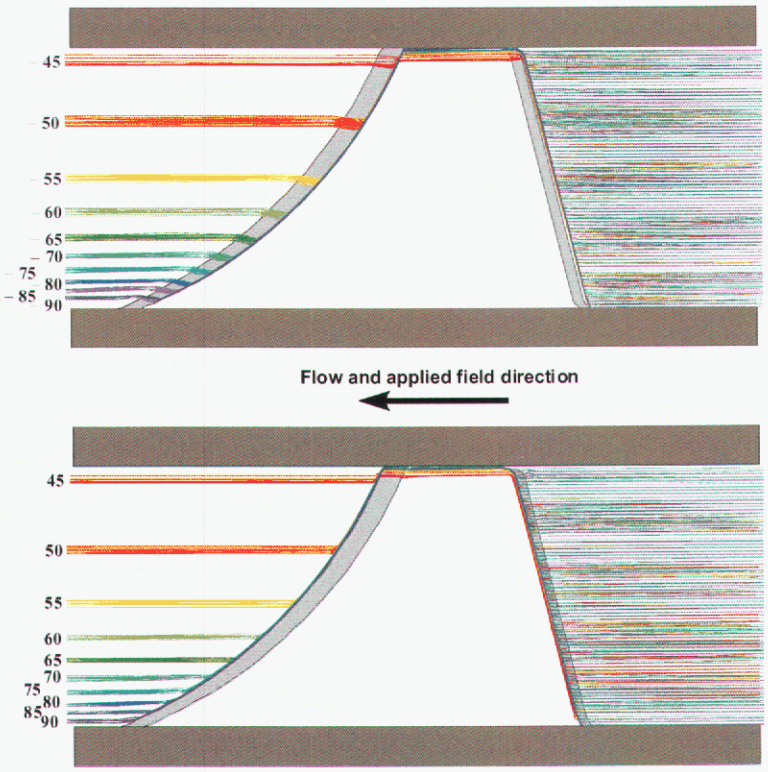

Figure 4-9 The use of a convex curved obstacle as a dispersive element. This numerical simulation shows the spatial concentration of a mixture of particles having discrete positive DEP mobilities. The curved obstacle at left disperses the particles by mobility into separate bands. The numbers at left are proportional to the DEP mobility of the particles, but the units are arbitrary. Notice that the spectrometer response depends approximately on the magnitude of the DEP mobility, not the sign.

Experimental Results

A mask was developed to test the performance and effectiveness of the corduroy-based designs. The mask design appears in Figure 4-10. This design employs three etch steps. The channels, shown in light blue are 20 μm deep. The ridges, shown in dark blue, are 7 μm deep. The third etch layer, shown in white, is 200 μm deep and is used to expand the flow uniformly from the relatively narrow, 1-mm drill holes to the ~4-mm wide main flow channels. This practice was invented for this application as a solution for avoiding the problems of lysis and particle sticking that otherwise occur in the jagged high-field area near drilled ports. The initial interface between the 200 μm-deep and 20 μm-deep channels is at a sufficiently high incidence angle (~85°) that the resulting field concentration does not restrain particles before they enter the device for most of the designs on the substrate. The designs that feature relatively high-incidence-angle ridges require the electric field to be lowered momentarily to inject particles into the main flow channel from the deep section. After injection, the electric field can be increased to manipulate the particles dielectrophoretically along the ridges while additional particles are prevented from entering the main flow channel by the facet interface.

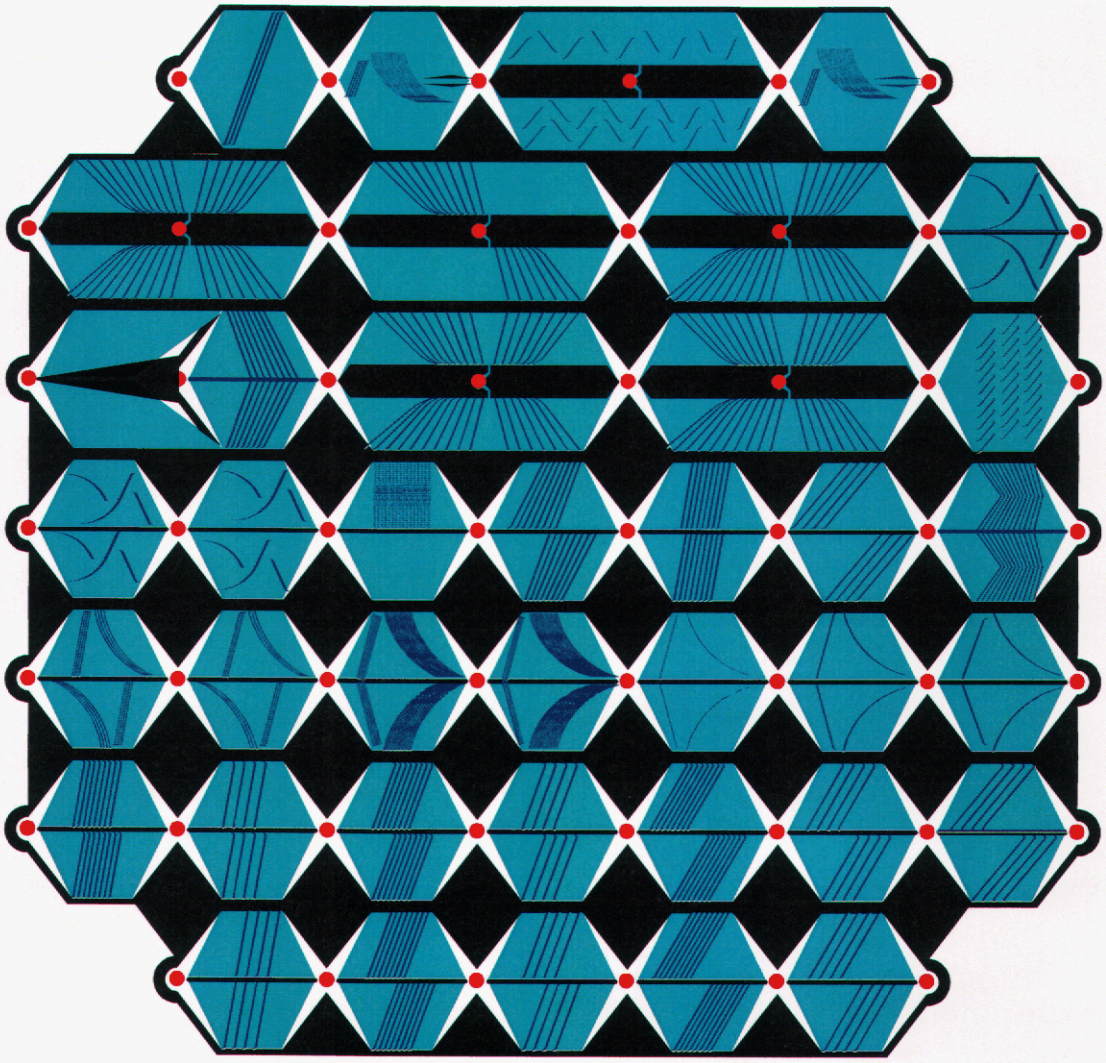

Figure 4-10 The design of the first corduroy test chip. Drill holes, indicated in red are 1-mm in diameter on 10-mm centers. The white features are 200-μm-deep faceted channel expanders that prevent fouling and lysis near drill holes and uniformly expand the flow into the 20-μm-deep main flow channels, shown in light blue. The dark-blue ridges are 7 μm deep and the black regions are the channel walls. The particle suspensions and voltages feed through to the channels through a silicone vacuum chuck with integral reservoirs that mate to the drill holes. Devices have been made in glass and are in the process of replication in plastic.

This design contains a number of novel and important design features including the initial expansion that challenged our normal glass fabrication procedures. Unfortunately, the first fabrication run was a total loss except for learned lessons, with all of the substrates warping and ultimately shattering during bonding. A second fabrication run fared better, but contamination in the bonding oven apparently caused the chips not to bond properly and all the channels were internally interconnected. Nevertheless, the flawed chip was able to demonstrate impressive performance. Figure 4-11 shows an image of the design one channel right from the bottom left concentrating 2-μm polystyrene particles to full

saturation in the bottom traps. Even at the relatively high initial concentration flowing in from the right, a concentration factor of >6000× was achieved in 16 seconds, limited only by complete saturation near the bottom wall.

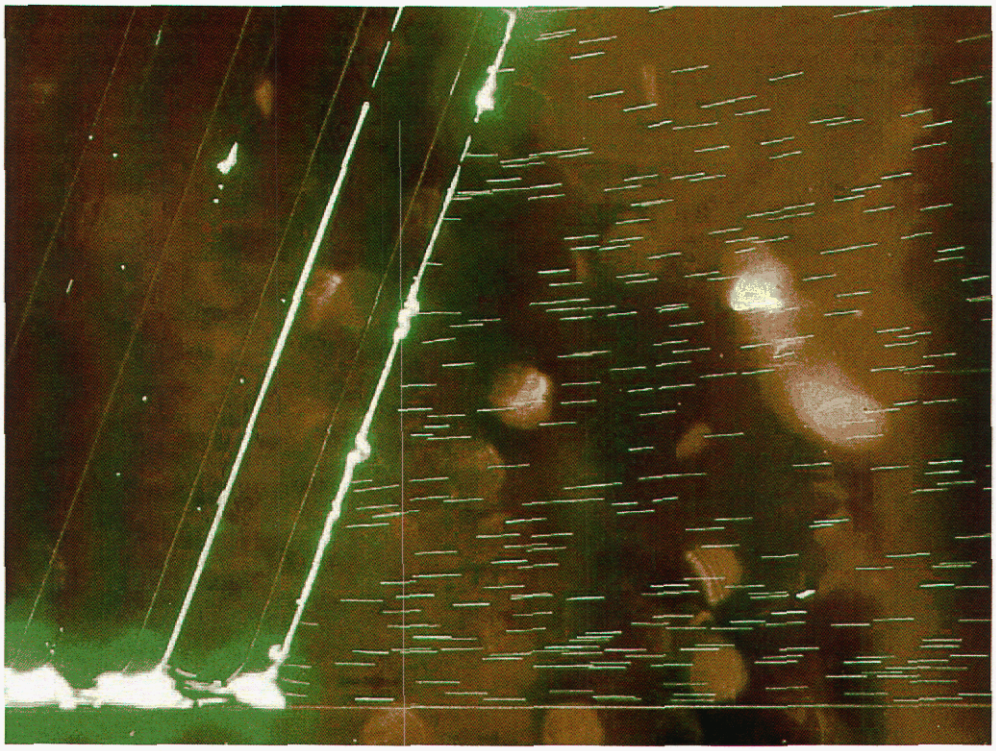

Figure 4-11 Steady state operation of a hybrid continuous/batch corduroy concentrator. The stream of 2-μm particles flowing from the right slide along the leading edge of the ridges and are trapped at the end of the ridges near the wall. The concentration factor, limited by the high concentration of the inlet stream is >6000×, reaching full saturation in less than 16 s.

This device graphically shows a number of important features. First, although there are a number of particles stuck to the ridges, the device robustly collects particles as a result of the redundant ridges. The device is functioning like a hybrid continuous and batch device: the particle "chooses" to follow or pass the ridges in a region where the concentration is relatively low and saturation effects are minimal, thus the selectivity of the device can be high. The selected particles then flow into traps where they are concentrated to near solid density and full saturation in a batch mode. The locations of the highly concentrated particle traps near the wall provides for easy and low-dispersion removal of the plug into a side channel (not part of the test design). Upon lowering the field, the particles were released in a concentrated plug, as expected.

At the time of writing a third glass fabrication run is underway, and stamps for forming plastic replicates are being plated. The rich variety of devices on this test substrate (Figure 4-10) will provide a wealth of knowledge for refining the methodology and establishing operating parameters and performance specifications for real biological particles.

MuCAD

The limitations of commercial software solutions were severe enough to force us to develop our own CAD program, MuCAD, to support our device development, simulations, and mask development, like that shown in Figure 4-10. MuCAD is hierarchical and represents shapes parametrically. The program is preloaded with device primitives, like channels, corduroy obstacles, and facets. Primitives or combinations of primitives called sub-designs can be arrayed in such a manner that any or all of the parameters in the sub-design can be incremented by a prescribed amount. These arrays can be nested into other devices, which, in turn, can be further arrayed to create a system. A more detailed description is presented in Appendix A.

Figure 4-12 shows a screen shot of MuCAD showing a four-layer (drill hole, deep etch, shallow etch, ridge) corduroy concentrator design. The rectangular element contains an array of corduroy obstacles.

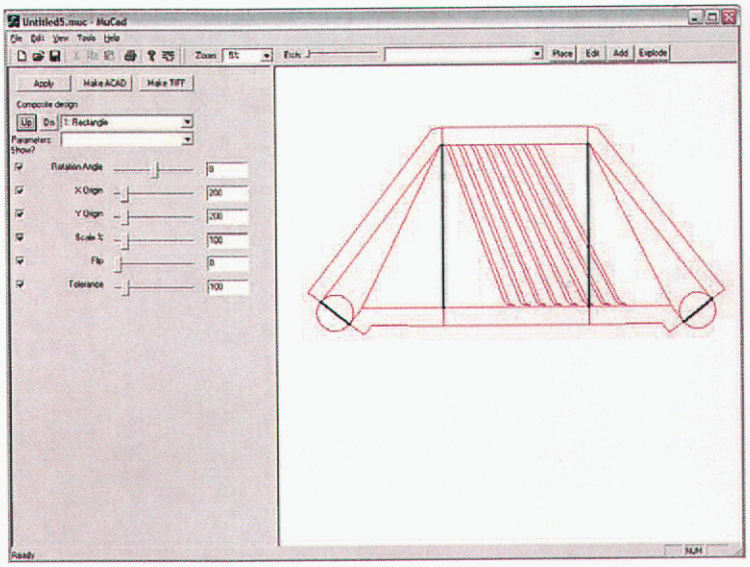

Figure 4-12 MuCAD screen shot showing the top-level view of the device hierarchy. The controls at right adjust the parameters for the overall design. The design features at right are red to indicate that they are selected. The black lines depict inlet and outlet ports for device primitives. From left to right the primitives are: a drill hole, a faceted expander, a rectangular channel element that contains an array of corduroy ridges, a faceted expander (in reverse) and a drill hole.

Conclusions

The corduroy design methodology emerged logically out of a progression of device architectures that addressed experimentally observed and theorized issues. Characterized by its ease of engineering and intuition, the main cost of the technique is need for an extra etch step in the fabrication. If the parts can be replicated with complete functionality, then there is negligible practical cost, and tremendous performance improvements over many of the electrode-based and post-based alternatives. The ability to make a two-obstacle automatic and high-throughput particle spectrometer that requires only a single D.C. power supply is remarkable and certainly exceeds our hopes at the start of this project. This development will almost certainly have a profound stimulating impact in microfluidics technology worldwide.

Based on these outstanding simulation and testing results, corduroy devices are working their way into designs for sample preparation systems and inter-device concentrators in several Sandia programs. The investment made to develop this technology will pay off in Sandia's improved ability to process real-world samples and increased detection-system sensitivity.

References

1 Karl Wally, Eric B. Cummings, C.R. Bowe Ellis, Michael P. Kanouff and Daniel J. Rader, "Particle Front End for Compact WMD Threat Detection Systems: Integrated Microsystem Concepts for Intelligent Particle Collection, Separation, Preconcentration, and Processing", SAND2002-8586, Sandia National Laboratories, 2002.

2 Eric B. Cummings, "The Corduroy Design Methodology for Dielectrophoretic Particle Concentration and Sorting," SAND report, Sandia National Laboratories, to be submitted in February, 2005.

This page intentionally left blank

Chapter 5 Remaining Challenges to Integration

An initial objective of this LDRD project was the demonstration of an integrated "front end" system capable of the collection, preconcentration, and selective transport of aerosolized biological agents from dilute atmospheric concentrations to microliter liquid concentrations for interfacing with μTAS systems, such as Sandia's μChemLab, for identification of bioagent bacteria and spores. Although our work to date has indeed demonstrated individual elements of this "front end" technology, we were not able to fully achieve our goal of an integrated demonstration before the LDRD project ended. Therefore, we propose to summarize the challenges that remain to be addressed for such an integrated demonstration to be achieved. And to recommend a path forward for further work, should additional funding be made available. We believe our work has clearly established the feasibility of the "front end" technologies described in this report, but in most cases, additional "readiness" development will be required to bring the technologies to a level that would allow their routine integration with *analysis and detection* technologies, such as Sandia's μChemLab, that are in a more advanced stage of development. Below, we discuss our recommendations for the proposed work of "readiness" development, and outline the elements needed to achieve an integrated demonstration. The many potential applications to which these front end technologies can be put, separately and in integration with each other, justifies, we believe, the further support required to achieve these goals. It is our hope that funding sponsors too will recognize this justification, and provide further funding to see this work go forward. Some of these potential applications are briefly described in the Chapter 6.

Further Work for Readiness Development

For each of the "front end" technologies that have been the subject of this LDRD project, we highlight here the additional work that we believe would bring these technologies to a sufficient level of readiness to allow their routine incorporation in future systems. Also included are recommendations for what additional work is required to complete the integration of these technologies into a concatenated system of bioaerosol particle collection, concentration, sorting, and selective transport.

Microseparator – Micromolding/Microembossing Development

Future work should develop the microseparator geometry in embossed, or injection-molded, polymer wafers. Materials and techniques that have been developed at Sandia/CA for the production of microfluidic wafers should be adapted to produce the required Opposed-Flow Virtual Cyclone geometry in a repeat pattern complementary to the microimpinger's microchannel pattern. The advantage of such micromolded parts can be realized through their enhanced performance and potential for low cost. An important characteristic of this microseparator technology is that as feature size is reduced, particle concentration, focusing, and separation occurs at lower velocities and, therefore, lower power consumption. It would

be advantageous to demonstrate this performance advantage using polymer fabrication processes.

If the microimpinger technology has been sufficiently developed, a further step in microseparator readiness development should be the integration of a microseparator wafer and a microimpinger wafer into a bonded aerosol collector wafer "sandwich".

Microimpinger – Integration with Inkjet Printhead Technology

The microimpinger is the least developed of the "front end" technologies that are the subject of this report because of the difficulties encountered in finding a solution to the problem of microparticle capture in the surface tension of the collection liquid. Work to date has identified microdroplet bombardment of the captured particles as a means to force the microparticles to submerge into liquid suspension. Further work would be needed to make this technique practical and efficient. Additional work would also be needed to clarify the mechanisms of particle wetting, the importance of microdroplet size, count, and coverage, the effect of lower surface tension solvents, or the addition of surfactants. A better fundamental understanding of particle capture, particle submergence, and physical and/or chemical surface tension behavior would be valuable in seeking an effective solution. This study and understanding is important for any system that attempts to capture particles directly into insufficiently agitated liquids, e.g., any aerosol collector of respirable-size particles into a liquid microvolume.

For the experiments described in this report, we generated microdroplets in an external commercial nebulizer using compressed air. For practical application, this microdroplet generator function must be miniaturized to be incorporated into the microseparator/microimpinger assembly. Fortunately, an existing technology of microdroplet generation is already available through inkjet printing and printhead technology. Therefore, further development work along these lines could proceed in collaboration with a commercial partner having expertise in droplet generation technology. Important to this development is the question of whether the surface-captured microparticles are transported and concentrated at the outlet end of the open microchannel. If such transport and concentration does occur, then the microdroplet bombardment can be localized to this location. If such transport does not occur, then the microdroplet bombardment will need to encompass the entire surface aperture of the open microchannel, impacting how microdroplet generation would be implemented. Transport experiments should be performed to resolve this question.

Further microimpinger development also requires the resolution of questions of microchannel fabrication, microchannel flow, electrokinetic flow, and evaporation make-up through capillary wicking. Our modeling work has identified the path forward here. Our previous report [ref, 5-1, SAND2002-8586] discusses these issues, reports modeling results, and identifies a proposed geometry (inverted "T") for further investigation. Prototype microchannel wafers which embody this proposed geometry should be fabricated and tested. Integrated testing with the microseparator is also necessary to show that the proposed microchannel geometry works for the evaporation conditions and dynamic pressures that arise in the combined assembly.

Dielectrophoretic Devices – Micromolding/Microembossing Demonstration

Future work should continue along the lines already started and previously described. Development of micro-embossed polymer wafers incorporating the corduroy geometries suitable to particle concentration and particle sorting should be pursued and demonstrated. Specific devices worthy of development and demonstration include:
i) a corduroy dielectrophoretic particle "spectrometer," sorting particles by dielectrophoretic polarizability, and ii) a high throughput particle concentrator.
The latter will require massively parallel flow geometries. Therefore, suitable flow distribution and collection schemes will need to be conceived, and fabrication and assembly processes will need to be developed. This may entail multilayer "sandwich" assemblies.

For the Post-based batchwise DEP concentrators, readiness development entails development of flow distribution and particle collection schemes to achieve macroscale fluid throughputs. This, too, entails the use of micromolded or microembossed flow elements combined in massive array.

Integrated Demonstration

A crude integration demonstration would be directly possible even using the current state-of-maturity of the front end prototype technologies and test apparatus. The different stages of this demonstration would need to be run *in-sequence and batchwise*, with batchwise sample holding reservoirs strategically positioned between stages. This would allow each stage in the collection sequence to proceed as its own step. When combined in sequence, a complete demonstration of bioaerosol particle collection, suspension, and liquid-phase concentration into a microfluid sample could be achieved. The microimpinger technology, with its rudimentary and still inefficient particle suspension through microdroplet bombardment, would be the most problematic part of such a demonstration.

Additional Integrated Demonstrations are available using the microseparator and DEP concentrator front end technologies piecewise, even with the current state-of-maturity of the prototypes and test apparatus. The microseparator technology can be used as a gas-phase particle concentration stage on an existing aerosol collection system feeding a μChemlab-based detection system. Such a scheme could be demonstrated, for example, with Sandia's current DoD μChemlab project. The DEP technology can be used as a liquid-phase particle concentration stage in an existing sample preparation system feeding μTAS detection systems. Such a scheme is being pursued, for example, with the LLNL/SNL BioBriefcase project.

Sample Preparation – Another Need for Successful Integration

Sample Preparation is another necessary, and complementary technology requiring further development to enable fully integrated demonstrations of autonomous collection, analysis and detection systems. *Sample preparation* has generally been funded as part of *detector* development because sample preparation protocols are so highly specific to individual detectors and bioagents. We, therefore, have not included *sample preparation* amongst our

"front end" technologies. *Sample preparation* development entails significant miniaturization and automation of the various sample preparation functions (e.g. cell lysis, protein purification, dye attachment) required for subsequent analysis and detection. Currently, microfluidic-based *sample preparation* development at Sandia/CA is being funded by specific project applications, in particular, by the joint LLNL/SNL BioBriefcase project for the DHS, and by the μChemLab/Bio bioagent detector project for the DoD. Therefore, until such time as an autonomous sample preparation technology becomes routinely available, any demonstrations integrating "front end" technologies with analysis and detection systems, will require manual intervention for the necessary sample preparation steps.

References

1. K. Wally, E. B. Cummings, C.R. B. Ellis, M. P. Kanouff and D. J. Rader, "Particle Front End for Compact WMD Threat Detection Systems: Integrated Microsystem Concepts for Intelligent Particle Collection, Separation, Preconcentration, and Processing", SAND2002-8586, Sandia National Laboratories, 2002.

Chapter 6 Additional Potential Applications

In addition to their use as an integrated aerosol collection "front end" to collect and concentrate particles for microseparations-based detectors such as μChemLab, the capabilities of these "front end" technologies justifies their use in other potential applications as well. A sampling of these applications is described below. As some of the examples demonstrate, these applications represent more than mere concepts, but, in some cases, have advanced to actual developmental prototype componentry.

Applications for OFVC Microseparator

HERD – Hybrid Emergency Radiation Detector

HERD is one element of a Sandia/CA site development initiative to demonstrate Livermore based technologies in Homeland Security applications. HERD stands for Hybrid Emergency Radiation Detector, a device that could be operated by emergency "first responders" to monitor and diagnose the effects of "dirty bombs". The detector incorporates a semiconductor-based room temperature radiation detector to detect the presence of radioactive particles in an respirable aerosol. The detector is designed to detect alpha-particle emission. Since alpha particle radiation has very little ability to penetrate materials, or to penetrate very far in air, the apparatus needs to bring the alpha detector and the alpha-emitting particle into close proximity. For this purpose, designers chose to use a version of Sandia's Opposed-Flow Virtual Cyclone (OFVC) MicroSeparator technology (Figure 6-1).

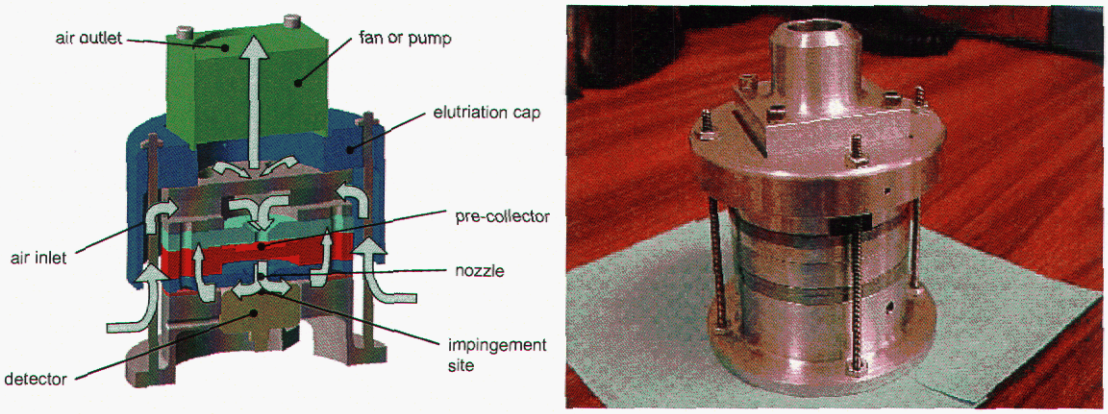

Figure 6-1 Hybrid Emergency Radiation Detector (HERD) prototype incorporating an Opposed-Flow Virtual Cyclone (OFVC) Aerosol Collector to focus particles onto a semiconductor-based room temperature operation alpha detector.

In this case, the OFVC operates "in-the-round", separating and concentrating particles to a central spot on a mylar film a few microns thick on the surface of the alpha detector.

Bioaerosol Trigger

Many existing and proposed bioagent analysis and detection systems propose to use a bioaerosol trigger scheme to enable them to minimize their consumption of reagent chemicals and power. In this scheme, the analysis and detection system remains in a standby mode until such time as a trigger awakens the system. The trigger operates continuously. Most proposed bioaerosol trigger systems are based on laser-based interrogation of aerosol particles to extract triggering information. One scheme uses visible-light laser diodes to monitor the count of particles in the size range of bacteria and spores (~ 1 μm diameter), and would trigger on unusually high counts. Another scheme adds UV-light laser diodes to the monitor to monitor the particles for UV fluorescence, a characteristic of bioparticles. Such systems trigger if they monitor particles in the size range of bacteria and spores (~ 1 μm diameter) and that are also UV fluorescent characteristic of bioparticles. In all such schemes the lasers can interrogate only small volumes of space for particles. Therefore any system which can enrich the concentration of particles available for interrogation would be very desirable. Our OFVC microseparator technology can provide such particle concentration enrichment in two ways. Configured to provide a line of concentrated particles, as in the microseparator which has been the subject of the development described in this report, the system can provide a streaming sheet of particles having a width of 50 μm or less, which lasers could interrogated end-on along the length of the line. Thus the laser beam would see the integrated effect of many particles along the length of the focused sheet of particles streaming by endwise. A second configuration of the OFVC concentrator can be arranged in an axially symmetric manner to separate and concentrate particles into a stream of particles that can be passed through the interrogation aperture of the laser detector. In either case, the concentration and spatial focusing provided by our microseparator technology could enhance the performance of bioaerosol triggers.

Aerosol Lab-on-a-Chip

A novel approach to real-time bioaerosol detection and identification is the recently patented Aerosol Lab-on-a-Chip (ALOC) concept (Rader, Wally, et al., 2002). The ALOC concept embodies a variety of aerosol collection, classification, concentration (enrichment), characterization, and sorting processes that are all fabricated onto a single substrate or layered stack of substrates. By taking advantage of modern microfabrication capabilities, an entire suite of discrete laboratory aerosol handling, characterization, and sorting techniques could be combined onto a single substrate, where they could be operated in parallel to perform a particle characterization of the sampled aerosol. The concept is shown schematically in figure 6-2.

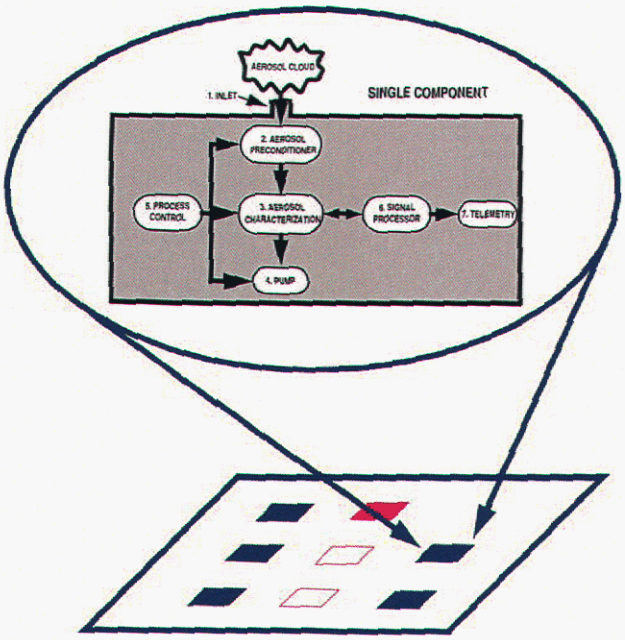

Figure 6-2 Schematic diagram of the Aerosol-Lab-on-a-Chip (ALOC) concept, patented by Sandia. An entire suite of discrete laboratory aerosol handling, characterization, and sorting techniques could be combined onto a single substrate.

In principle, a small, lightweight ALOC-based device ultimately could replace an entire laboratory suite of bench-top diagnostics. A compact ALOC device could also be deployed alongside more specific bioaerosol sensors; in this scenario the ALOC could provide independent real-time data (i.e., to support alarm decisions or to reduce false positives) or function as a trigger for activating the accompanying sensors (i.e., to reduce consumable or power usage). Another benefit of the ALOC concept is that the performance of many of the traditional aerosol handling, sorting and characterization techniques improve with miniaturization (e.g., inertia-based techniques). By constructing large arrays of identical parallel OFVC samplers, it becomes possible to reduce gas velocities and thereby greatly reduce the power consumption needed for gas sampling and handling.
The ALOC concept was first disclosed at Sandia National Laboratories and a US patent for the ALOC was issued in May 2002. The original claims comprising the ALOC patent are quite general; recently, however, a Continuation in Part to the original patent has been filed that extends the patent into additional, specific applications. Funding is currently needed to design, fabricate, and demonstrate a prototype ALOC system.

Applications for Corduroy DEP Concentrators and Sorters

The corduroy DEP technology is broadly applicable to a variety of applications across the spectrum of liquid fluidic scales. Single microchannel devices operate at the nanofluidic scale. Single wafer devices incorporating many parallel microchannels operate at the microfluidic scale. DEP devices incorporating stacks of wafers in massively parallel microfluidic array operate at the meso- and macrofluidic scale.

Applications of the corduroy DEP devices include particle filters (e.g., clogless lysis debris filters), particle sorters (e.g. flow cytometry sorters), and particle selectors (e.g. bio-particle selectors in biodetectors).

Water quality monitoring and water quality analysis are two areas where DEP particle concentration and sorting capabilities have already found applications. A recent LDRD project is using post-array DEP concentrators to monitor water-borne bacteria and parasites. Sandia has been in discussions with an international consortium regarding a CRADA project on water quality monitoring that would entail Sandia μChemlab detectors to monitor water quality. DEP concentrators would be used as a "front end" to μChemlab. The corduroy DEP technology could be used within these applications to introduce a greater ease of engineering design and operational simplicity.

The MuCAD design software will have numerous applications in supporting research and commercial development, giving researchers and designers a modeling facility to develop their own chips, devices and applications for the corduroy DEP technology.

Applications for Direct Microimpingement Technology

As the accelerating pace of research and development in μTAS technology over the past decade would suggest, a number of important applications are working to benefit from systems wherein aerosol collection is married to analysis and detection at the microfluidic scale. All such systems face the issue of the interface between aerosol particles and the microliter sample volume. The medical and pharmaceutical industries need allergen monitors, allergen samplers; infectious agent monitors and samplers; sterile environment and sterile hood monitors and samplers, etc. The food processing Industry needs airborne contaminant monitors and samplers, airborne bacteria monitors and samplers, etc. It is not an overstatement to suggest, that in most detector applications where the developers are working hard to miniaturize and even microminiaturize analysis and detection, there is dissatisfaction with the general state of development of aerosol sampling and bioaerosol sampling. State-of-the-art collector design has remained largely unchanged for decades, and little effort has previously been addressed to the problems of interface with the microfluidic scale.

Appendix A MuCAD

Commercial CAD packages do not support the corduroy design methodology well. In order to create photolithographic masks for fabricating designs, design-feature shapes need to be represented electronically in a standard mask format. Most common formats represent a feature as a closed polygon, a set of points connected by straight line segments that approximate the desired shape of the feature within a tolerance. Simple shapes, like straight channels and facets can be represented easily, but the more-general curves used in the corduroy methodology require so much effort to represent in a polyline format that automated (computer) assistance is necessary. Unfortunately commercial CAD solutions generally do not provide for automatic polygon generation from arbitrary curves. This methodology also generally calls for arrays of features that are either identical or vary slowly in one or more parameters, like, for example, entry length, entry radius of curvature, entry incidence angle, central radius of curvature, etc., parameterizations that are not supported in commercial CAD packages, and consequently cannot be arrayed non-uniformly. Moreover, features on the mask must generally be adjusted to precompensate for fabrication effects like overetch in order for the fabricated feature to approximate the desired shape. Again, commercial packages do not generally provide for automated and intelligent etch compensation. Finally, commercial packages do not generally support simulation of the fabricated geometry and automatic mesh generation for as-fabricated device simulation.

The limitations of commercial software solutions were severe enough to force us to develop our own CAD program, MuCAD, to support our device development, simulations, and mask development, like that shown in Figure 4-10. MuCAD is hierarchical and represents shapes parametrically. The program is preloaded with device primitives, like channels, corduroy obstacles, and facets. Primitives or combinations of primitives called sub-designs can be arrayed in such a manner that any or all of the parameters in the sub-design can be incremented by a prescribed amount. These arrays can be nested into other devices, which, in turn, can be further arrayed to create a system.

Figure A-1 shows a screen shot of MuCAD showing a four-layer (drill hole, deep etch, shallow etch, ridge) corduroy concentrator design. At left are parameter controls, at right is the image of the design. This view shows the topmost hierarchy. From left to right, the drill hole, faceted expander, rectangular channel, faceted expander, and drill hole are connected at their ports, shown in black, so that any adjustment of the individual elements automatically scales, rotates, and translates the other elements to keep the ports in alignment. The rectangular element contains an array of corduroy obstacles.

An element of the design can be selected by clicking on it. Figure A-2 shows the same design when the rectangular channel or any of the features in its hierarchy is clicked. Now, the drill holes and faceted expanders appear in the colors that represent their mask layers. Note that the adjustable parameters in the left pane that describe the rectangle.

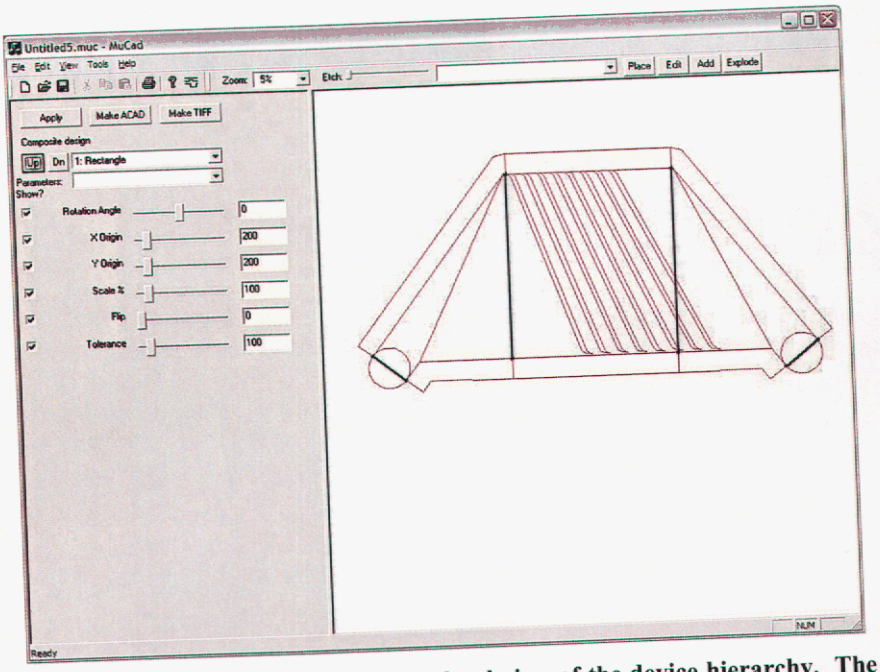

Figure A-1 MuCAD screen shot showing the top-level view of the device hierarchy. The controls at right adjust the parameters for the overall design. The design features at right are red to indicate that they are selected. The black lines depict inlet and outlet ports for device primitives. From left to right the primitives are: a drill hole, a faceted expander, a rectangular channel element that contains an array of corduroy ridges, a faceted expander (in reverse) and a drill hole.

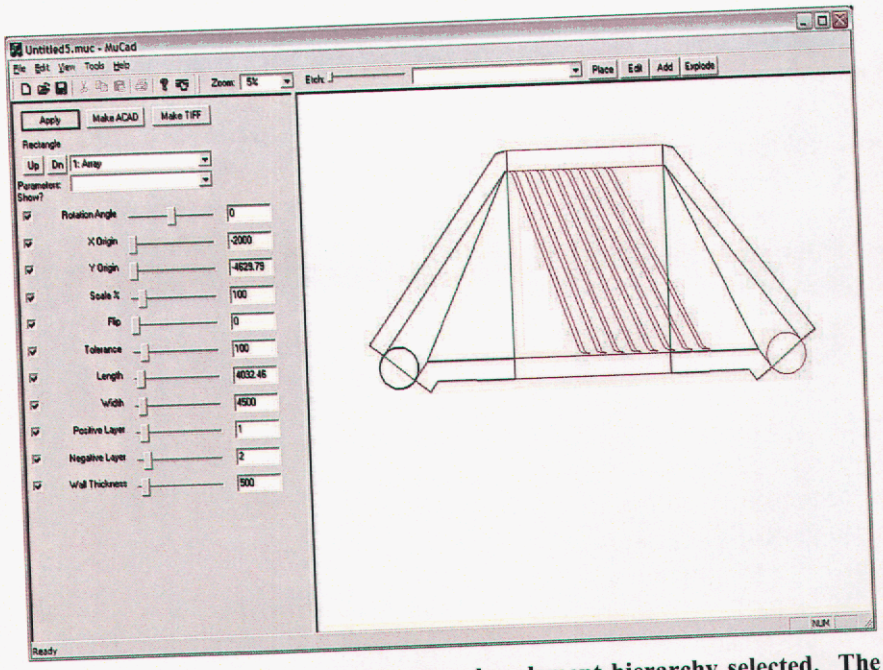

Figure A-2 MuCAD screen shot with the rectangular element hierarchy selected. The controls at right indicate and adjust the parameters that define the channel segment.

Clicking on one of the corduroy ridges descends into the rectangular-section's hierarchy. Now the array element is selected (Figure A-3). The controls in the left pane show how each parameter in the corduroy ridge elements that comprise the array can be incremented in the array. In this example, the horizontal position is incremented and the angle of the central section (start and end angle) are incremented for each of the eight selected copies. These controls automatically appear when a master element is created for the array.

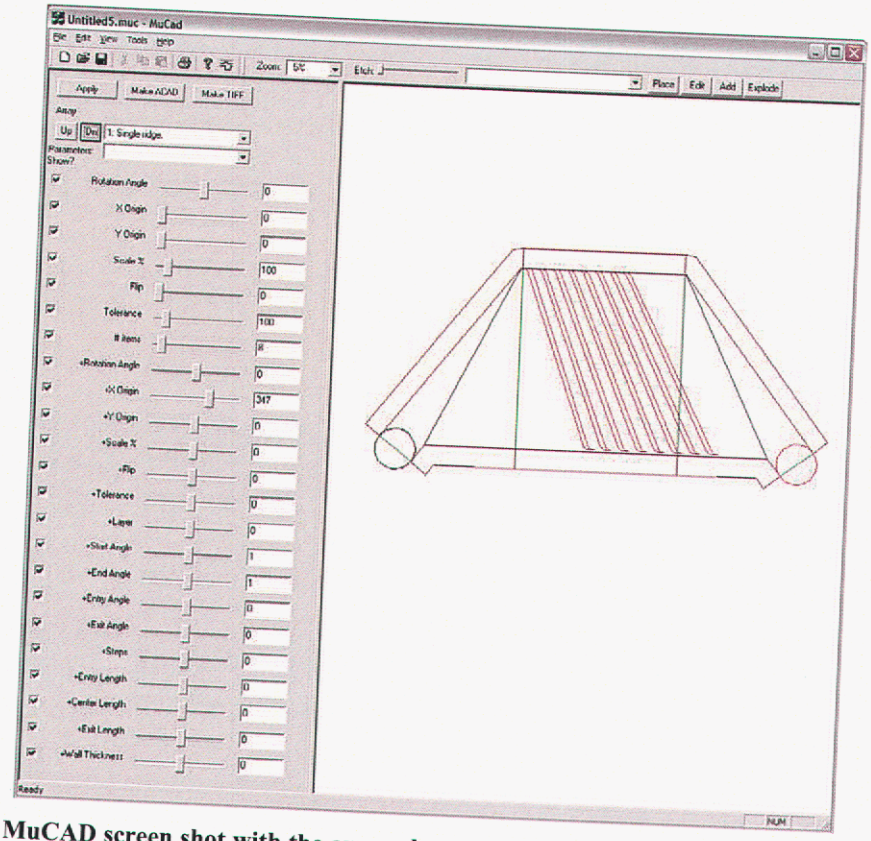

Figure A-3 MuCAD screen shot with the array element selected. Note that the controls allow one to increment any or all of the parameters of the corduroy obstacles that comprise the array. The initial values of the parameters in the array are based on a master array element owned by the array element.

The properties of the master element can be modified by clicking on the element. In Figure A-4, the controls show MuCAD's parameterization of a "standard" corduroy ridge. The entry, central, and exit regions of the ridge can have different sizes, radii of curvature, and angles, easily facilitating the creation of curved dispersive elements, spillways, and traps.

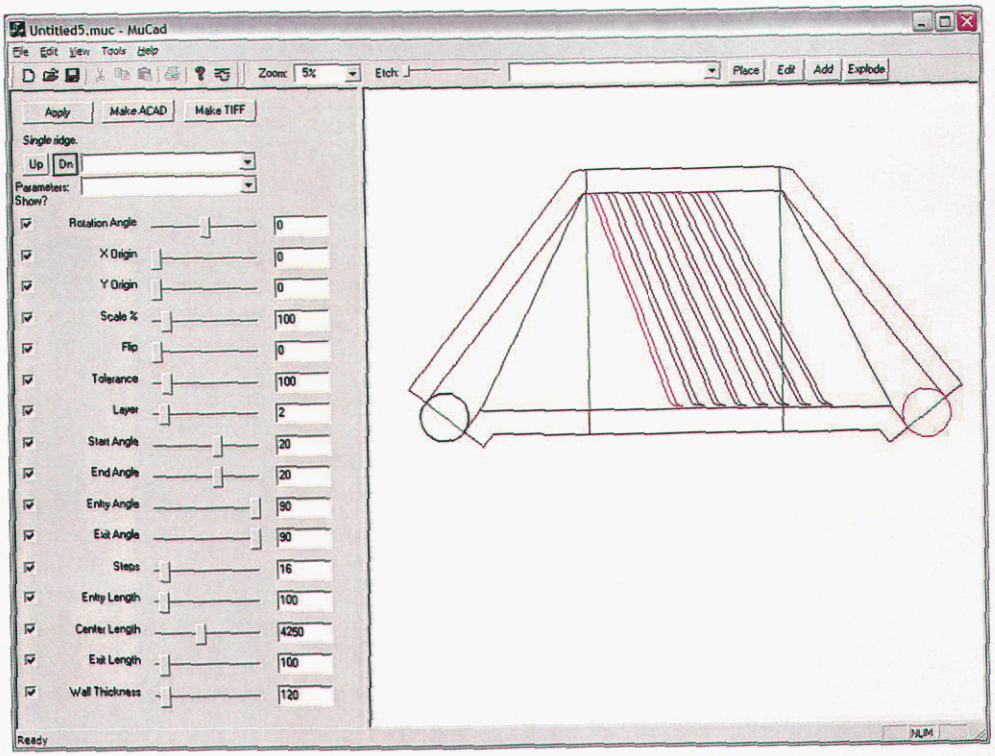

Figure A-4 MuCAD screen shot showing the master element of the array. The parameters of this element are copied and incremented by the array element to create the array.

An important feature of MuCAD is its ability to pre-compensate intelligently and automatically for over-etch. The "intelligence" lies in its ability to handle different kinds of vertices differently. For example, in Figure A-5 at the top, the sharp tip of the blue, deep channels emerging from the drill holes is impossible to etch isotropically, but important to approximate. The tip vertices of faceted channels are internally given a critical status, which causes the etch-compensation algorithm to over-neck and over-extend the channel in this region to reduce the fluid-mechanic impact of the isotropic over-etch, as shown in the bottom of Figure A-5. The ridge and shallow-channel layers are etched considerably less than the deep-etch layer so the etch compensation is less dramatic, but nevertheless important.

MuCAD can simulate the actual isotropic etch profile of the designs, as shown in Figure A-6. The grayscale of the image is proportional to depth: white is the deepest, black is zero depth (a channel wall). MuCAD can save this quantitative raster image to an image file (e.g., .tiff, .jpg, etc) from which the design can be analyzed using Laplace, an ideal electrokinetic and linear-dielectrophoretic flow solver developed at Sandia, as shown in Figure A-7.

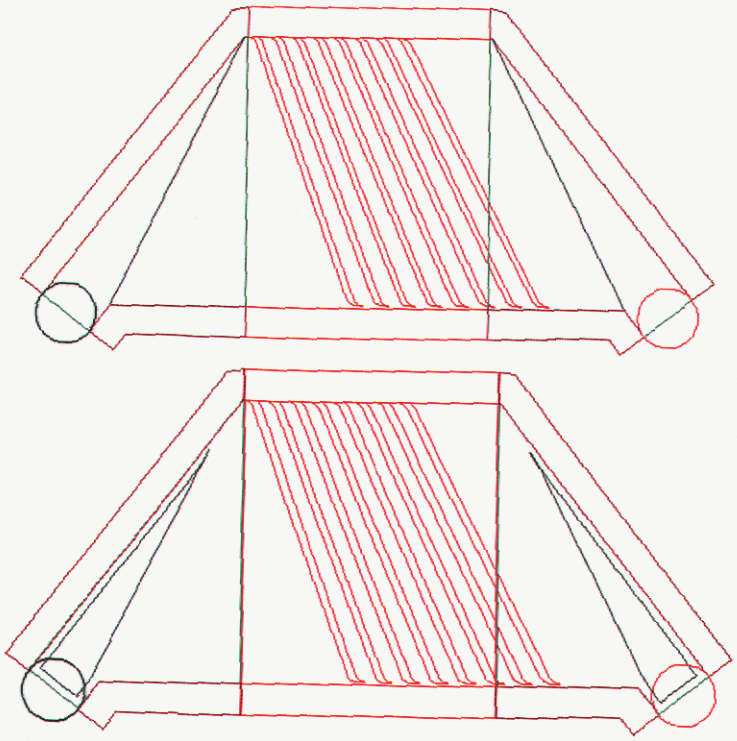

Figure A-5 Automated, intelligent etch-back compensation saves considerable time and effort and reduces the likelihood of error. Top design: nominal geometry. Bottom design: etch-compensated mask geometry.

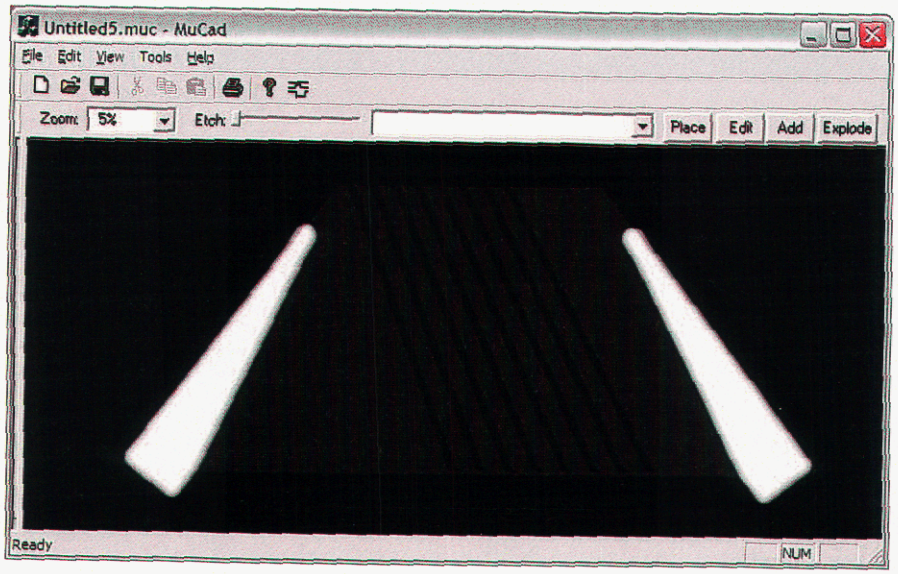

Figure A-6 MuCAD screen shot showing automatic etch simulation of the etch compensated design in Fig. A-5. The grayscale of the image is proportional to channel depth. The white channels are 200-µm deep the gray channels are 20-µm deep and ~4-mm wide and the dark-gray ridges come to within ~7 µm of the channel lid. The black boundary (grayscale 0) corresponds to a zero-depth channel, i.e., a wall.

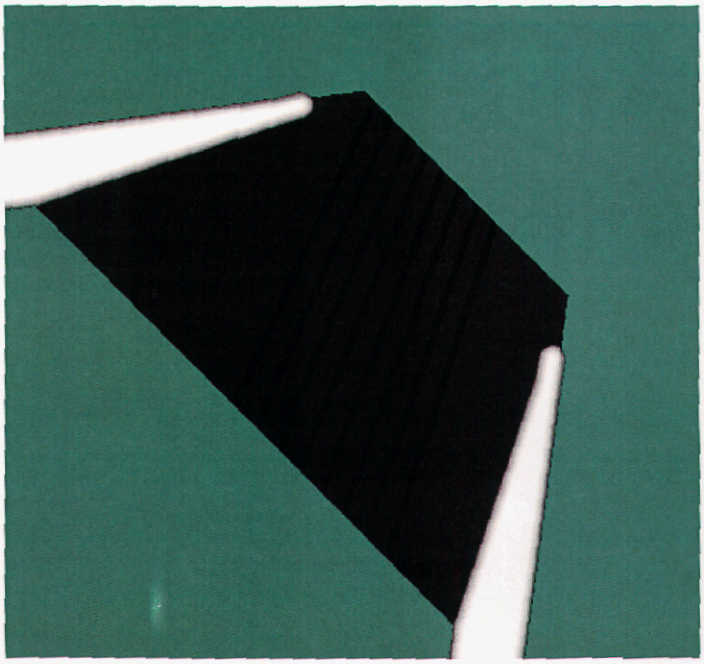

Etch simulation (grayscale proportional to depth)

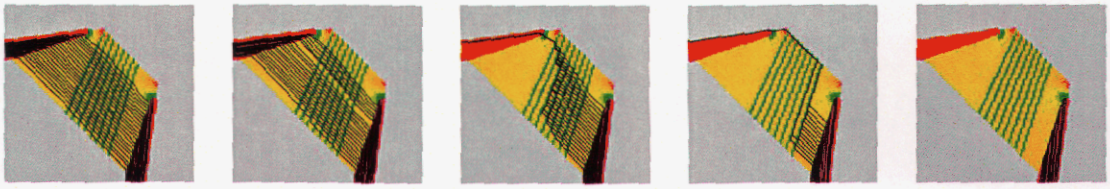

-0.002 -0.00225 -0.0025 -0.00275 -0.003

Dielectrophoretic mobility (EK mobility = 1, Diffusivity = 0)

Figure A-7 The MuCAD etch simulation is in a format that is compatible with Laplace, a quasi-two-dimensional electrokinetic and dielectrophoretic flow solver. The as-etched geometries can be simulated and the device performance studied extensively with a minimum of manual effort before committing to a costly fabrication run.

The power of the combination of MuCAD and Laplace is obvious in Figure A-8, a large-array-based spectrometer. Devices having a large number of features and large non-uniform arrays are favorable for robustness and performance, but could not be studied practically, particularly with the etch compensated and simulated, without these tools.

Finally, when a device is ready for inclusion on a mask, MuCAD exports a script file that loads the design automatically into AutoCAD, preserving layers. Because it was developed explicitly for microfluidics applications, MuCAD is exceptionally powerful and can support many microfluidic design applications in addition to implementing the corduroy methodology.

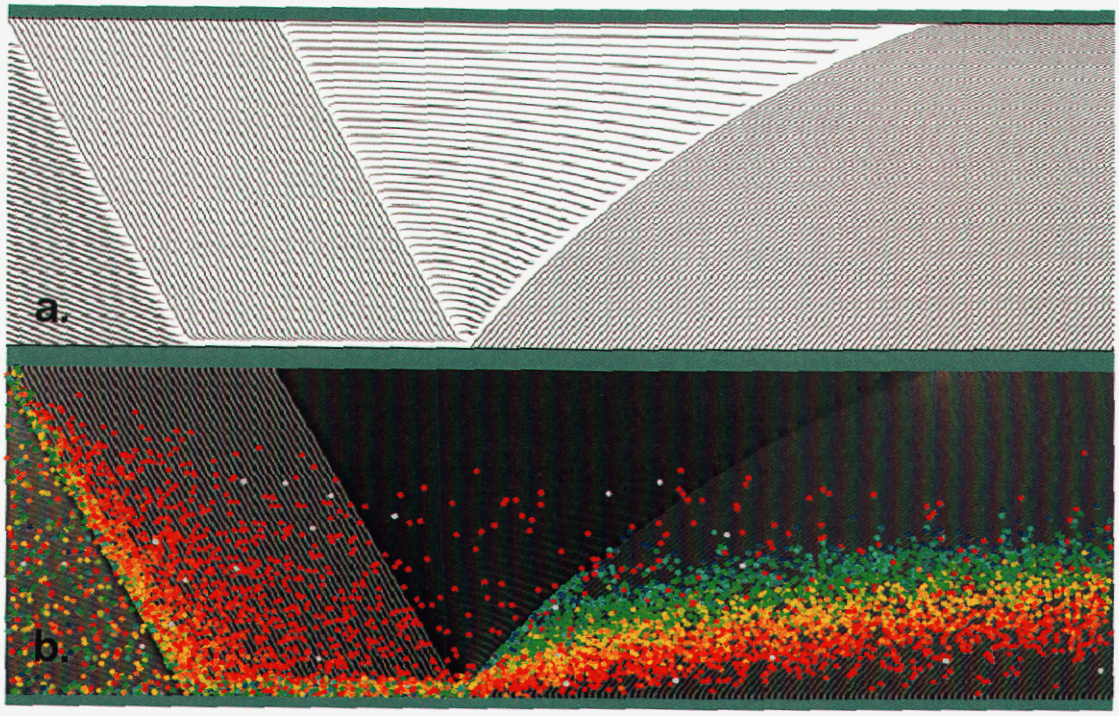

Figure A-8 The combination of MuCAD and *Laplace* supports the development and simulation of designs that are far too complicated to draft and etch-compensate manually. As in the spectrometer design shown in a. and then simulated in b. The spectral color of the particles indicates dielectrophoretic mobility with red and blue indicating respectively low and high mobility.

Distribution

3	MS9018	Central Technical Files, 8945-1
1	MS0899	Technical Library, 9616
1	MS9021	Classification Office, 8511/Technical Library, MS 0899, 9616
1	MS9021	Classification Office, 8511 for DOE/OSTI
1	MS0188	D. Chavez, LDRD Office, 1030
1	MS9004	R. H. Stulen, 08100
1	MS9004	D. L. Lindner, 08150
1	MS9054	T. A. Michalske, 08300
1	MS9951	A. E. Pontau, 08324
1	MS9951	Y. Fintschenko, 08324
4	MS9951	E. B. Cummings, 08324
1	MS9403	J. M. Hruby, 08700
1	MS9404	G. D. Kubiak, 08750
1	MS9291	J. A. Lamph, 08755
6	MS9291	K. Wally, 08755
1	MS9291	C. R. Bowe Ellis, 08755
1	MS9409	C. D. Moen, 08775
4	MS9291	M. P. Kanouff, 08775
1	MS0384	C.W. Peterson, 09100
1	MS0834	J. E. Johannes, 09112
4	MS0834	D. J. Rader, 09112